Preliminary development of a transistor-based biosensing platform

Incorporating an Extended Gate Field Effect Transistor design and Copper Free Click Chemistry functionalization of Screen Printed Electrodes

Master's thesis in biotechnology, MPBIO

LINNÉA FRYKBERG

DEPARTMENT OF PHYSICS AND ASTRONOMY

CHALMERS UNIVERSITY OF TECHNOLOGY
Gothenburg, Sweden 2026
www.chalmers.se

Master's thesis 2026

Preliminary development of a transistor-based biosensing platform

Incorporating an Extended Gate Field Effect Transistor design and Copper Free Click Chemistry functionalization of Screen Printed Electrodes

LINNÉA FRYKBERG

CHALMERS
UNIVERSITY OF TECHNOLOGY

Department of Physics and Astronomy
Division of Materials Physics
Chalmers University of Technology
Gothenburg, Sweden 2026

Preliminary development of a transistor-based biosensing platform
Incorporating an Extended Gate Field Effect Transistor design and Copper Free Click Chemistry functionalization of Screen Printed Electrodes
LINNÉA FRYKBERG

© LINNÉA FRYKBERG, 2026.

Supervisors:
Adepu Saritha, the Swedish University of Agricultural Sciences
Hammersberg Johan, Mölnlycke Health Care
Karlsteen Magnus, Department of Physics and Astronomy
Skiöldebrand Eva, the Swedish University of Agricultural Sciences

Examiner: Karlsteen Magnus, Department of Physics and Astronomy

Master's Thesis 2026
Department of Physics and Astronomy
Division of Materials Physics
Chalmers University of Technology
SE-412 96 Gothenburg
Telephone +46 31 772 1000

Typeset in LaTeX
Printed by Chalmers Reproservice
Gothenburg, Sweden 2026

Preliminary development of a transistor-based biosensing platform
Incorporating an Extended Gate Field Effect Transistor design and Copper Free Click Chemistry functionalization of Screen Printed Electrodes
LINNÉA FRYKBERG
Department of Physics and Astronomy
Chalmers University of Technology

Abstract

Early detection of osteoarthritis remains challenging, as few diagnostic methods combine accessibility, minimal invasiveness, and sufficient analytical sensitivity. Biosensor-based detection of disease related biomarkers found in saliva represents one promising route toward more practical and sensitive diagnostic tools. Electrochemical biosensors employing Extended-Gate Field-Effect Transistor (EG-FET) designs represent a viable approach due to their compact format and low cost implementation.
This project presents the preliminary development of a transistor-based biosensing platform using an EG-FET design coupled to an EmStat Pico potentiostat, representing an early step toward a system capable of detecting osteoarthritis biomarkers in equine saliva. Screen-printed gold electrodes (Au-SPEs) were functionalized using copper free click chemistry, enabling selective surface modification for future attachment of DBCO-coupled Fab' fragments. The functionalization strategy used in this work employed lipoamido-PEG4-azide as the linker molecule, followed by DBCO-PEG4-alcohol passivation and BSA blocking prior to exposure to equine saliva samples to evaluate non specific binding. Cyclic voltammetry, electrochemical impedance spectroscopy and chronoamperometry were used to evaluate each functionalization step and to assess the performance of the EG-FET system.
Both linker attachment and subsequent DBCO-PEG addition and BSA layers produced clear and reproducible electrochemical signatures when measuring with either cyclic voltammetry or electrochemical impedance spectroscopy, confirming that the functionalization protocol used was effective on the Au-SPE surfaces. Chronoamperometric measurements with the custom EG-FET system responded to surface bound charge variations, demonstrating that the setup successfully enabled detection of electrochemical changes occurring at the gold electrode interface. However, functionalization with molecules carrying a net neutral charge or positioned too far from the surface resulted in no detectable transistor response, this underscores the importance of understanding the system's sensitivity to Debye screening effects. Both the ionic strength of the surrounding medium and the physical length and net charge of the functionalization molecules influence the effective sensing distance, which in turn affects the transistor's ability to detect future biomolecular binding events. Further optimization of buffer conditions, molecular architecture, and electrode geometry will therefore be essential to improve sensitivity and robustness.
Overall, this work represents a promising first step toward a transistor-based biosensor for osteoarthritis related biomarkers. While the platform shows clear potential, substantial development remains before a fully functional diagnostic device can be achieved.

Keywords: Extended Gate Field Effect Transistor (EG-FET), Electrochemical Impedance Spectroscopy (EIS), Cyclic Voltammetry (CV), Chronoamperometry (CA), Screen Printed Electrodes (SPEs), surface functionalization, Copper free click chemistry, Debye Length.

Acknowledgements

I would like to express my gratitude to everyone who has supported me throughout this project. I am especially thankful to Magnus Karlsteen for his guidance, availability and supporting discussions. I also thank Johan Hammersberg for his time, patience and essential help in understanding and building the measurement system. My appreciation further goes to Agnes Gustafsson for valuable collaboration and support in the laboratory throughout the spring.

I would also like to thank my supervisors Eva Skiöldebrand, whose research made this project possible, and Saritha Adepu for providing samples and answering practical questions. I am grateful to Matthew Giese for introducing click chemistry and advising on linker and PEG selection for future work.

I further wish to acknowledge Fredrik Höök, Andreas Dahlin, and Julie Gold for their guidance and discussions during the laboratory process and project planning. My thanks also go to Ezio Zanghellini for managing laboratory orders, and to Jan-Åke Wiman and Charlotte Hamngren Blomqvist for assistance with PDMS fabrication and molding.

Finally, I would like to thank all others who have contributed in various ways throughout this work.

Linnéa Frykberg, Gothenburg, June 2026

List of Acronyms

Below is the list of acronyms that have been used throughout this thesis listed in alphabetical order:

Au-SPE	Gold Screen-Printed Electrode
BGN^{262}	Biglycan biomarker fragment
BSA	Bovine Serum Albumin
CA	Chronoamperometry
CE	Counter Electrode
$COMP^{156}$	Cartilage Oligomeric Matrix Protein biomarker fragment
CPE	Constant Phase Element
CV	Cyclic Voltammetry
DBCO	Dibenzocyclooctyne
DoE	Design of Experiments
EG-FET	Extended-Gate Field-Effect Transistor
EIS	Electrochemical Impedance Spectroscopy
ELISA	Enzyme-Linked Immunosorbent Assay
Fab'	Antigen-Binding Fragment
JFET	Junction Field-Effect Transistor
LoD	Limit of Detection
OA	Osteoarthritis
OECT	Organic Electrochemical Transistor
PBS	Phosphate-Buffered Saline
PDMS	Polydimethylsiloxane
PEG	Poly(ethylene glycol)
R_{ct}	Charge-Transfer Resistance
RE	Reference Electrode
SPE	Screen-Printed Electrode
WE	Working Electrode

Contents

1

Introduction

Osteoarthritis (OA) is a common condition affecting both humans and animals.[1] It is characterized by low grade inflammation in the joints that progresses gradually over time, leading to disability, pain and economic loss.[2][3][4][5] According to estimations based on data from 2020, OA affects approximately 595 million people, corresponding to about 7.6% of the world's population.[6] Annual OA-related direct costs vary widely across countries, ranging from a few hundred to nearly 20 000 USD depending on healthcare system and disease severity.[7] While this work aims for the preliminary development of a biosensor later intended for horses, the disease presents similarly across mammals and therefore diagnostic and therapeutic approaches are promising to be transferable between mammal species.[1][2][8][9]

Today OA is most often diagnosed at an irreversible stage using radiography, meaning that joint destruction is an inevitable outcome.[5][9][10] There is a need to develop measuring methods that are able to detect OA in its reversible stages, as reliable tools for early OA detection could substantially benefit equine welfare. Preferably these methods would be cheap and give fast results while also be applicable in the field, making it accessible to all horse owners. This would allow veterinarians and horse owners to detect the disease before irreversible joint damage occurs and implement suitable interventions. A simple and affordable method would also enable regular follow up and better informed decisions during training and rehabilitation, ultimately improving long-term clinical outcomes for the horse. Given the requirements for a cheap, fast and field-applicable method, biosensors represent a promising approach as they can be developed to meet many of these demands. In the context of equine OA diagnostics, the envisioned biosensor would first be developed and validated in vitro, as initiated in this project. A future step would be to adapt the system for ex vivo use in field settings such as stables, where saliva samples could be applied directly to an exchangeable sensor. In the long term, the platform could be further advanced toward in vivo integration for continuous monitoring in the oral cavity during training, a development that would require extensive biocompatibility testing and compliance with relevant ISO standards for medical devices intended for oral contact.

The original plan of this project involved the complete development of a biosensor that was later intended for ex vivo use, including immobilization of specific antibody fragments on the sensor surface to enable selective detection of two specific OA related biomarkers. Due to a too tight time frame in obtaining the antibody

fragments, the experimental work instead changed focus on establishing a proof of concept surface functionalization strategy. The strategy used involves copper free click chemistry with DBCO groups, being the same reactive group intended for future antibody fragment immobilization using DBCO coupled Fab' fragments. The functionalization approach represented in this project is therefor broadly applicable to any DBCO-terminated molecule, extending beyond the specific antibody fragments associated with OA biomarkers.

The following sections in the introduction present the full biological and technological background of the envisioned biosensor system, while the experimental work in this project covers only the initial development of the platform and its proof of concept surface functionalization without any Fab' fragments.

1.1 Diagnostic needs in equine osteoarthritis

Several studies have explored the possibility of diagnosing OA before osseous damage becomes visible. Approaches such as presymptomatic cartilage texture mapping based on Magnetic Resonance Imaging (MRI) have been tested, while positron emission tomography (PET) and scintigraphy have been suggested as potential alternatives.[9][10] Common for all these is that they require expensive equipment and can be difficult to manage around a living horse.

A possible method for detecting OA in the presymptomatic phase involves the use of biomarkers, defined as measurable indicators of biological processes or disease states.[11] Several studies have searched for and investigated biomarkers relevant to OA. Some biomarkers that have been shown to increase their levels before the onset of lameness are Interleukins 1 and 6 (IL-1 and IL-6), Matrix Metalloproteinases 9 and 13 (MMP-9 and MMP-13), Disintegrin and Metalloproteinase with Thrombospondin Motifs-5 (ADAMTS-5), Chondroitin Sulfate Epitope 846 (CS846), Glycosaminoglycans (GAG), Hyaluronic Acid (HA), C-Terminal Telopeptide of Type II Collagen (CTX-II), as well as fragments of Cartilage Oligomeric Matrix Protein (COMP) and Biglycan (BGN).[2][3][4][5][9][12][13] While all are possible candidates for detecting OA in its presymptomatic phase, some are more specifically linked to the disease than others. For instance, IL-1 and IL-6 are proinflammatory cytokines, a part of the immune system, and can become activated by many other things than OA, infections or trauma being common reasons. While COMP and BGN are more specifically associated with changes in cartilage and bone structure.[3][4][5][9][13] The intended fututre for the sensor of this project is to study two already identified fragments of COMP and BGN, $COMP^{156}$ and BGN^{262}, which were also used in a previous study related to equine OA.[13] These fragments are also biomarkers for which veterinarians can submit synovial fluid from an affected joint for laboratory analysis when evaluating joint inflammation or suspected OA.[14]

BGN^{262} has been demonstrated to be detectable in equine saliva, as shown in a recent study on salivary biglycan neoepitopes in horses.[4] For $COMP^{156}$, salivary detection data has been generated and is currently submitted for publication. Correlation between salivary and synovial fluid concentrations has not yet been in-

vestigated. Saliva is considered an attractive screening fluid, as it contains many molecules otherwise found in synovial fluid and serum and its composition reflects the physiological and disease state of the body.[4] Because saliva is substantially more accessible and minimally invasive to collect, these biomarkers could in practice be sampled directly by horse owners and a field applicable biosensor could enable on site measurement, making routine monitoring far more accessible.

Numerous methods exist for quantifying soluble biomarkers. One of the most commonly used methods is the Enzyme-Linked Immunosorbent Assay (ELISA). This technique is considered the gold standard for protein-based biomarker analysis and assays can be validated for use under both Good Laboratory Practice (GLP) and Good Manufacturing Practice (GMP), increasing the reliability and reproducibility of concentration measurements.[15] Validated ELISA assays are available for both $COMP^{156}$ and BGN^{262}. The BGN^{262} assay has been analytically validated and published. [9] [4] For $COMP^{156}$, an earlier version of the assay using a previous antibody has been published [5], while the updated assay employing a newly developed antibody has been analytically validated and is currently submitted for publication. These ELISA assays provide a robust reference for quantifying both $COMP^{156}$ and BGN^{262} biomarkers and form the basis for calibrating future biosensor signals against known concentrations. While ELISA is a robust and well established method, it is time consuming (48 hours in lab + delivery time) [14] and requires specialized laboratory equipment as well as multiple disposable components, limiting its applicability for field-based settings such as stables.

The limit of detection (LoD) defines the lowest analyte concentration that can be reliably distinguished from background noise and is therefore a key metric for evaluating the overall sensitivity of the sensing system. It is given by

$$LoD = \Delta S_{blank} + 3\sigma_{blank} \tag{1.1}$$

where ΔS_{blank} is the mean signal measured for blank samples (saliva without target biomarkers) and σ_{blank} is the corresponding standard deviation.[16] The blank measurements should be performed on an active sensing surface under identical conditions as the analytical measurements.

The required LoD of the future sensor is determined by the concentration levels associated with healthy states for the target biomarkers. Threshold values for distinguishing healthy from osteoarthritic states for both biomarkers have been established based on analyses of synovial fluid and saliva samples. For $COMP^{156}$, healthy thresholds are typically <50 ng/mL in saliva and <500 ng/mL in synovial fluid, with observed sample ranges spanning approximately 40–400 ng/mL and 200–5000 ng/mL, respectively.[14] For BGN^{262}, healthy thresholds are typically <500 ng/mL in saliva and <2000 ng/mL in synovial fluid, with observed sample ranges spanning approximately 50–1000 ng/mL and 500–8000 ng/mL, respectively.[14] These established concentration intervals define the analytical range that a future biosensor must be able to detect, requiring sensitivity at least down to the reported threshold values for each biomarker in saliva and a dynamic range that extends beyond the

highest concentrations observed in saliva.

1.2 Biomarkers $COMP^{156}$ and BGN^{262}

$COMP^{156}$ and BGN^{262} are biomarkers associated with cartilage and bone remodeling processes linked to inflammatory activity in synovial joints.[3][4][5][9][13]

COMP is a major protein, 524 kDa, playing a central role in articular cartilage homeostasis while also cross-bridging the collagen network by binding to collagen type II and IX in the extracellular matrix (ECM).[3][5] Articular cartilage is the smooth tissue covering the ends of bones in joints, often getting damaged in OA. Homeostasis in the articular cartilage refers to the balance between degradation and repair mechanisms, which may be disrupted in OA, leading to loss of cartilage ECM.[17] The ECM occupies the spaces between cells and contributes to the structural integrity and organization of tissues within an organism.[18] As OA begins to develop, low grade inflammation causes the release of proinflammatory cytokines such as IL-1 and IL-6, leading to fragmentation of ECM molecules.[5][12] The destruction of this matrix causes the release of unique fragments of COMP that are only present in diseased cartilage. There can be different cleavage sites done to the molecule, each resulting in different fragments. One fragment, with peptide sequence "SGPTHEGVGMAFAK" located in position 156 of the protein, has been shown to be released early in the progression of OA. The same study show that $COMP^{156}$ is significantly increased for joints with acute lameness compared to healthy joints, joints with chronic lameness or joints during the late stages of OA.[5] This suggests that $COMP^{156}$ may be a promising prognostic biomarker for the early stages of OA.

Biglycan (BGN) is present in both cartilage and skeletal bone, contributing to the structural integrity and homeostasis of these tissues.[9] In skeletal homeostasis, BGN plays a key role in promoting bone formation and facilitating interactions between cells and the ECM, as well as supporting bone matrix mineralization.[4][9] Similarly to COMP, BGN is gradually fragmented during inflammatory processes, causing release of specific fragments. One such fragment, BGN^{262}, corresponding to cleavage site 262GLGHNQIRM, has been shown to have 100% homology across various species, including horses and humans, making it a promising diagnostic biomarker also for humans.[9] The same cleavage site has been shown to reflect the response to joint load as early as during the first 6-month interval of training in young racehorses, highlighting its potential as an early biomarker for cartilage and bone changes in the reversible stages of OA.[4]

Together, $COMP^{156}$ and BGN^{262} complement each other. COMP reflects early cartilage changes, while BGN also provides information on bone related processes. Measuring both biomarkers can help localize disease activity and assess the progression of OA, enabling detection of active joint related inflammation as well as identification of OA in its reversible stages.

1.3 Antibodies and specific bindning

To selectively capture and quantify targeted biomarkers, specific antibodies or antibody fragments are required, making antibody antigen interactions a fundamental component of future biosensor designs for this work. Antibodies (immunoglobulins) are large, Y-shaped glycoproteins generated by the adaptive immune system to recognize and bind distinct molecular structures. Each antibody consists of two identical heavy chains and two identical light chains.[19] In an IgG antibody, the light chain is composed of two immunoglobulin (Ig) domains, whereas the heavy chain contains four Ig domains.[20] Like all polypeptides, each immunoglobulin domain has an N-terminal and a C-terminal end. In both heavy and light chains, the N-terminal amino acid sequences vary greatly between different antibodies. The first Ig domain is the most variable, corresponding to approximately the first 110 amino acids of the full chain.[20] The variable domains, also known as the fragment antigen binding (F(ab)) region, creates the antigen binding site (called the paratope) that binds to a specific part of an antigen (called the epitope).[19] Apart from the N-terminal variable domain, remaining Ig domains in both heavy and light chains are constant for antibodies belonging to the same isotype.[20]

For biosensing applications, full-length antibodies can be enzymatically cleaved into smaller fragments such as F(ab) or Fab' fragments, which retain the same antigen specificity while reducing overall molecular size.[19] This reduction is advantageous in systems where the Debye screening length limits the effective sensing distance, as smaller recognition elements position the binding event closer to the sensor surface. Consequently, Fab' fragments are considered a promising recognition element for the future of this work, and the molecular components intended for functionalization of these fragments are presented further down in this section.

The intended chemical strategy for future biomarker recognition involved a stepwise surface functionalization designed to enable specific binding of Fab' fragments. Although the full protocol with Fab' fragments could not be completed in this project, an identical workflow was carried out using only DBCO-PEG molecules to measure non specific binding, and the detailed experimental procedure of that is presented in Section 2.2 of the report. The description below outlines the planned approach for measuring specific binding, while the experimental work in this thesis instead focuses on a proof of concept functionalization method and evaluating non specific binding, a necessary control for all future biosensor development.

Figure 1.1 shows the chemical structure of the linker used, lipoamido-PEG$_n$-azide, where n denotes the number of repeating ethylene glycol units. In the future implementation, a PEG1 linker is suggested, corresponding to a molecular weight of approximately 100 Da.[21] A similar linker was used in this project, but with a longer PEG chain (PEG4) due to time constraints and the availability of chemicals within the scope of the project.

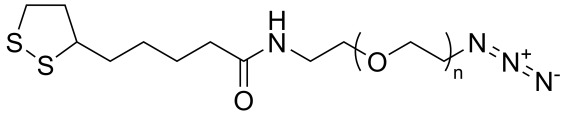

Figure 1.1: Chemical structure of the linker molecule lipoamido-PEG$_n$-azide, where n denotes the number of ethylene glycol repeat units in the PEG chain. Future work is suggested to use PEG1 ($n = 1$), corresponding to an approximate molecular weight of 100 Da.
Created in BioRender. Frykberg, L. (2026) `https://biorender.com/rc8i92k`

On a cleaned gold surface, the first step of the planned functionalization is the attachment of a thiol-terminated linker molecule, lipoamido-PEG4-azide. The lipoamide group forms a stable bond to gold, creating a defined azide terminated monolayer that serves as the reactive platform for subsequent copper free click chemistry. Figure 2.4 illustrates the linker bound to a gold surface.

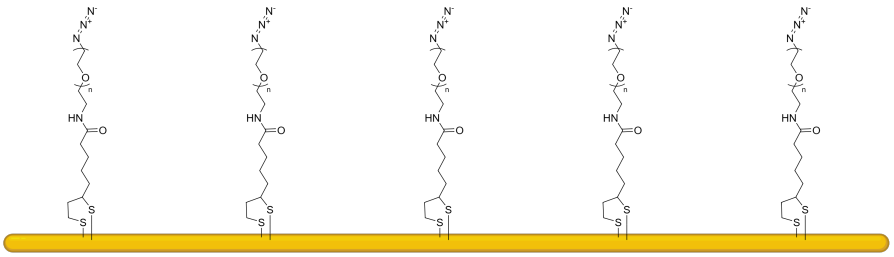

Figure 1.2: Schematic illustration of lipoamido-PEG$_n$-azide linker molecules immobilized on a gold surface through sulfur–gold interactions, forming the basis for subsequent surface functionalization.
Created in BioRender. Frykberg, L. (2026) `https://biorender.com/nk6vv7y`

Once the azide-terminated linker is immobilized on the gold surface, the next planned step is to introduce DBCO-functionalized molecules for copper free click chemistry. A 1:1 molar ratio between Fab'–DBCO conjugates and passivating DBCO-PEG chains is intended as a first try, allowing Fab' fragments to be positioned at defined distances while unreacted surface sites will be blocked by PEG to minimize non specific binding. This ratio was selected as an initial approximation and would be optimized in future sensor development. The resulting mixed layer provides specific recognition sites for the intended biomarkers ($COMP^{156}$ or BGN^{262}), while the PEG molecules suppress non specific adsorption. Figure 1.3 shows the chemical structures of the intended click reagents for future development, Fab' fragment coupled to DBCO-PEG4-amide-lipoic acid and DBCO-PEG12-OH, where DBCO-PEG12-OH has a molecular weight of approximately 600 Da.[21] Using these reagents with lipoamido-PEG1-azide as linker would place the biomarker binding event approximately 6 nm away from the surface of the sensor.[21]

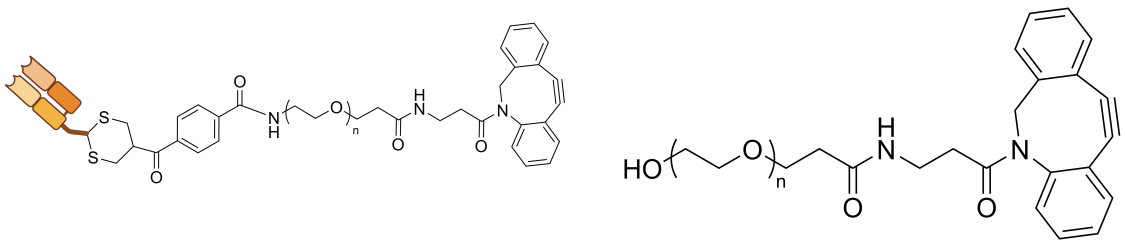

(a) **(b)**

Figure 1.3: Chemical structures of dibenzocyclooctyne-terminated molecules intended for copper-free click chemistry. a) Fab' fragment coupled to DBCO-PEG$_n$-amide-lipoic acid, where n denotes the number of ethylene glycol repeat units in the PEG chain. Future work is suggested to use PEG4 ($n = 4$) or shorter if available. b) DBCO coupled PEG chain, DBCO-PEG$_n$-OH, where n denotes the number of ethylene glycol repeat units in the PEG chain. Future work is suggested to use PEG12 ($n = 12$), corresponding to an approximate molecular weight of 600 Da.
Created in BioRender. Frykberg, L. (2026) `https://biorender.com/ea77ex9` and `https://biorender.com/ooop8j5`

Figure 1.4 illustrates the mixed surface layer formed by Fab' fragments and PEG passivation molecules bound to the linker on the gold surface.

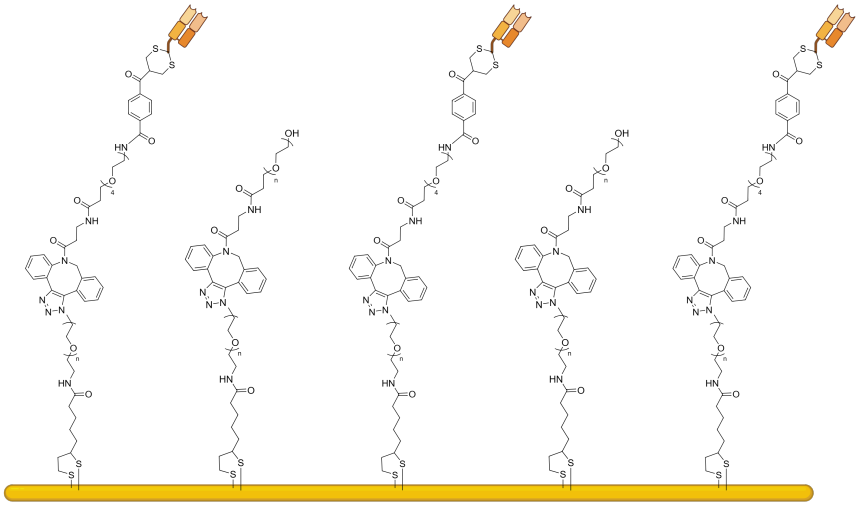

Figure 1.4: Fab' fragments and passivating PEGs on gold surface.
Created in BioRender. Frykberg, L. (2026) `https://biorender.com/t860w2s`

In the final step of the planned surface architecture, remaining unreacted areas are to be blocked with bovine serum albumin (BSA) to further reduce non specific binding. Illustrated in Figure 1.5.

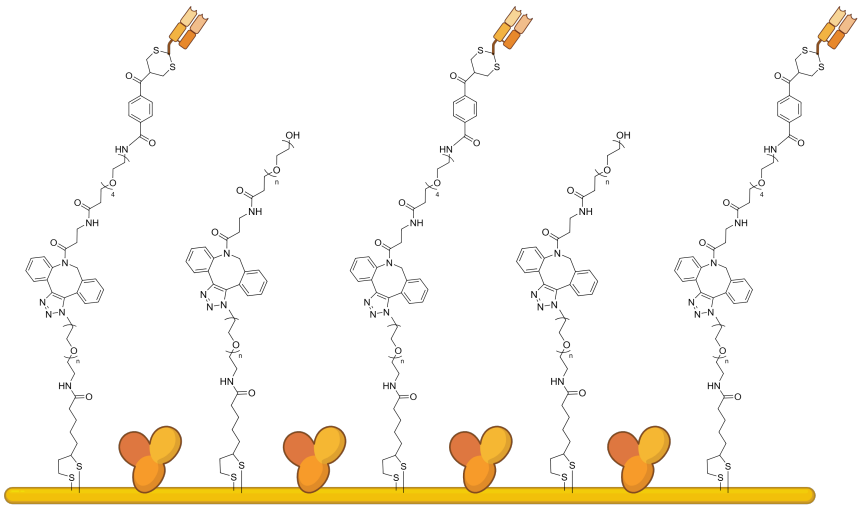

Figure 1.5: The fully functionalized active surface.
Created in BioRender. Frykberg, L. (2026) `https://biorender.com/wnx20le`

This fully functionalized surface architecture represents the planned configuration for measuring specific biomarker binding. In the present work, only non specific binding was evaluated experimentally using PEG-only control surfaces, consisting of surfaces that underwent click chemistry only with DBCO-PEG and no DBCO-Fab' fragments. Such controls are essential in biosensor development, as they establish how much of the measured signal originates from non specific interactions rather than true analyte recognition and are therefore needed in a future on-site calibration system. The intended equation used for future on site calibration can be seen in equation 1.2.

$$S_{\text{calibrated}} = S_{\text{specific}} - S_{\text{control}} \tag{1.2}$$

Here, S denotes the measured signal, S_{specific} refers to the signal obtained from the active Fab' functionalized mixed surface and S_{control} refers to the PEG only functionalized surface.

1.3.1 Dissociation constant and concentration dependent sensor response

The dissociation constant, K_D, is commonly used to describe the binding affinity between two interacting molecules.[22] A low K_D value corresponds to strong binding, whereas a high K_D value indicates weaker binding between the molecules.[22] More specifically, K_D represents the concentration of a binding partner at which half of the available binding sites are occupied at equilibrium.[22] Due to its ability to quantify molecular interactions, K_D is widely used in biochemistry and biosensor applications to characterize binding strength.[22] The measured value of K_D can vary depending on experimental conditions such as temperature and pH, since these parameters influence intermolecular interactions and molecular charge states.[23]

Based on the Langmuir interaction model, the binding between an immobilized receptor R and an analyte ligand L can be described as a reversible 1:1 interaction.[24]

$$R + L \rightleftharpoons [RL] \tag{1.3}$$

At equilibrium, the association and dissociation rates are equal, giving

$$k_a[R][L] = k_d[RL] \tag{1.4}$$

where k_a and k_d are the association and dissociation rate constants, respectively.[24] The dissociation constant K_D can therefore be expressed as

$$K_D = \frac{[R][L]}{[RL]} \tag{1.5}$$

where $[R]$ represents the concentration of free binding sites on the sensor surface, $[L]$ is the concentration of free ligand in solution, and $[RL]$ is the concentration of bound receptor-ligand complexes. For surface-based biosensors, the measured equilibrium signal is commonly assumed to be proportional to the amount of bound receptor-ligand complex, $[RL]$. The fractional surface coverage, θ, can therefore be defined as

$$\theta = \frac{[RL]}{[R_{\text{tot}}]} \tag{1.6}$$

where $[R_{\text{tot}}]$ is the total concentration of available binding sites on the sensor surface. Assuming a simple 1:1 interaction at equilibrium, the total number of binding sites can be expressed as

$$[R_{\text{tot}}] = [R] + [RL]$$

which gives

$$[R] = [R_{\text{tot}}] - [RL]$$

Substituting this expression into Equation 1.5 yields

$$K_D = \frac{([R_{\text{tot}}] - [RL])[L]}{[RL]}$$

Rearranging gives

$$K_D[RL] = [R_{\text{tot}}][L] - [RL][L]$$

$$[RL](K_D + [L]) = [R_{\text{tot}}][L]$$

and therefore

$$[RL] = \frac{[R_{\text{tot}}][L]}{K_D + [L]}$$

Substituting the expression for $[RL]$ into Equation 1.6 gives

$$\theta = \frac{\frac{[R_{\text{tot}}][L]}{K_D+[L]}}{[R_{\text{tot}}]} = \frac{[L]}{K_D + [L]} \tag{1.7}$$

Equation 1.7 corresponds to the equilibrium form of the Langmuir adsorption isotherm, where θ represents the fraction of occupied binding sites as a function of analyte concentration.[25] The fractional coverage, θ, can then be used to express the sensor response as

$$S = S_{\max} \cdot \theta \tag{1.8}$$

where S is the equilibrium signal at a given analyte concentration, $S_{\max}$ is the maximum signal obtained at complete surface saturation, and θ is the fraction of occupied binding sites.[25] At analyte concentrations approaching surface saturation, the sensor response levels approaches $S_{\max}$, meaning that additional analyte no longer results in a proportional increase in signal. Consequently, $S_{\max}$ determines the upper limit of the sensor response.

Substituting Equation 1.7 into the expression given in Equation 1.8 gives

$$S(L) = S_{\max} \cdot \frac{[L]}{K_D + [L]} \tag{1.9}$$

where S denotes the equilibrium signal at a given analyte concentration, $S_{\max}$ represents the maximum signal corresponding to complete saturation of binding sites, and $[L]$ is the analyte concentration in solution. By measuring the equilibrium signal S_i for a range of analyte concentrations $[L_i]$, the parameters K_D and $S_{\max}$ can be estimated by nonlinear regression using appropriate software, based on Equation 1.9. At equilibrium, the Langmuir model implies a characteristic property of the system, when $[L] = K_D$, the sensor response reaches half of its maximum value. This can be shown directly from Equation 1.9. Thus, K_D corresponds to the analyte concentration at which half of the binding sites are occupied, and the signal reaches 50% of its saturation value.

To obtain robust calibration models, measurements at known ligand concentrations can be performed under a range of controlled environmental conditions, such as different pH values and temperatures. This generates a set of calibration curves that capture how the binding interaction, and thus the sensor response, varies with the surrounding conditions. For unknown samples, the pH and temperature could be determined prior to analysis, allowing the calibration curve corresponding to the closest matching conditions to be selected for concentration estimation. Consequently, K_D should not be regarded as a single fixed constant, but rather as a condition-dependent parameter that varies across the calibration set. Interpreting the sensor response within this environmental context improves the reliability and accuracy of the estimated ligand concentration.

In the present work, the sensor surface was not fully functionalized with specific Fab' fragments and no concentration dependent biomarker binding experiments were performed. Consequently, dissociation constants and equilibrium calibration curves were not experimentally determined within this study. However, the pre-

sented framework may be relevant in future work for characterization of Fab'-based biomarker binding under defined measurement conditions, as well as for calibration of EG-FET system biosensor responses against corresponding ELISA-derived concentrations from the same sample solutions.

1.4 State of the art in biosensing

Recent reviews show that biosensors are an emerging and rapidly developing field, combining fast response times with high analytical sensitivity.[26][27] In contrast to ELISA, biosensors offer immediate responses as analytes that bind to the biochemical component of the sensor directly generate an electrical signal proportional to the concentration of analytes.[28]

Organic electrochemical transistors (OECTs) have recently emerged as one of the most promising device platforms in biosensing. Their ability to operate at low voltages combined with their biocompatibility and strong signal amplification capabilities make them well suited for detecting a wide range of biochemical targets. OECTs have demonstrated strong potential for detecting pH, ions, small molecules, and protein biomarkers, with significant progress reported in the last couple of years.[26] Although OECTs were not implemented in this work, they represent a promising direction for future development of the system due to their strong signal amplification and potential for improved sensitivity in biomarker detection.

Field-effect transistor (FET) biosensors have also gained increasing interest due to their high sensitivity, fast response, small size, low power and potential for low cost mass level manufacturing.[27] In certain biosensor designs, an electrode can be coupled to a FET as an extended gate (EG-FET).[29] The electrode used can be both inexpensive and replaceable, making this approach promising for practical use in field settings such as stables.

Modern biosensor development is strongly influenced by advances in surface chemistry. Copper free click chemistry, awarded the Nobel Prize in Chemistry in 2022, has become a widely adopted functionalization method due to its bioorthogonality, high reaction efficiency, and compatibility with sensitive biomolecules.[30][26] This makes the method particularly suitable for immobilizing antibodies and Fab' fragments on gold electrodes, as the bioorthogonal reaction conditions preserve the structural integrity of the F(ab) region required for specific biomarker recognition.

An EG-FET measurement platform was developed in this work, together with a copper free click chemistry functionalization protocol applied to gold screen printed electrodes, acting as the extended gate. Preliminary evaluation of non specific binding in equine saliva was also performed. Taken together, this work lay the foundation for a future electrochemical biosensor intended to target the OA-associated biomarkers $COMP^{156}$ and BGN^{262} in equine saliva.

1.5 Aim

The aim of this project is to develop the initial components of an electrochemical biosensing platform for detecting OA related biomarkers in equine saliva. This is achieved by establishing an EG-FET measurement setup and implementing a copper free click chemistry–based surface functionalization protocol on gold Screen Printed Electrodes. The work focuses on developing a proof of concept functionalization strategy suitable for future integration with DBCO-coupled Fab' fragments as recognition elements, enabling selective detection of $COMP^{156}$ and BGN^{262} in equine saliva under ex vivo conditions in field settings such as stables. In the long term, the platform is intended to be further developed toward potential in vivo use, which will require future biocompatibility evaluation and alignment with relevant ISO standards.

1.6 Limitations

Several limitations of this work should be acknowledged. All experiments were performed under controlled in vitro conditions using equine saliva in room temperature with measured pH and known concentrations of both $COMP^{156}$ and BGN^{262} (established through ELISA). Although saliva is a biologically relevant matrix, in vitro measurements do not fully capture the dynamic, continuously changing environment present in the oral cavity. This limits the ability to assess sensor performance under realistic physiological conditions.

The platform developed in this project represents an initial proof of concept rather than a complete biosensing system. While an EG-FET setup and a copper free click chemistry functionalization method was established, the integration of DBCO-coupled Fab' fragments as recognition elements was not experimentally validated. Consequently, key performance parameters such as sensitivity, selectivity, limit of detection, long-term stability, and response time could not be evaluated.

SPEs also introduce batch to batch variability, which may affect reproducibility and require further testing. Additionally, the EG-FET configuration is likely sensitive to environmental factors such as temperature, pH and ionic strength, all of which vary in equine saliva and between measurement conditions and may influence the electrical response of the system.

While the long term vision for the system includes ex vivo measurements in field settings such as stables and, ultimately, in vivo integration for continuous biomarker tracking in the oral cavity, achieving this will require significant advances in sensor robustness, antifouling resistance, mechanical stability as well as wireless data transmission.

1.7 Structure of the thesis

This work is a preliminary platform development and proof-of-concept study of a surface functionalization strategy intended for future application to specific Fab' fragments for detection of two OA-related biomarkers in equine saliva, $COMP^{156}$ and BGN^{262}. It is important to emphasize that the present study does not yet include specific biomarker detection, but instead focuses on establishing and validating the underlying electrochemical sensing platform and surface chemistry required for such future measurements.

The thesis is structured to follow the experimental workflow of platform development, surface modification and electrochemical evaluation of the custom platform. First, the EG-FET measurement system is characterized to assess baseline stability and reproducibility of the electrochemical response. Second, the surface functionalization strategy is investigated using stepwise chemical modification, where each reaction step is evaluated using cyclic voltammetry (CV) and electrochemical impedance spectroscopy (EIS) to confirm successful immobilization and surface passivation. Finally, the EG-FET configuration is assessed to determine whether the device can respond to interfacial changes in surface charge induced both by the functionalization steps and by direct exposure of bare gold surfaces to model proteins, including BSA and synthetic biomarkers of $COMP^{156}$ and BGN^{262}.

This structure is chosen to separate platform characterization, surface chemistry validation and custom platform measurements into distinct stages, allowing each component to be evaluated independently.

2

Theory

This chapter provides the theoretical background necessary to understand the electrochemical measurements performed in this work, the custom transistor-based system and the surface chemical principles underlying the proof-of-concept functionalization protocol.

2.1 Electrochemical detection

Electrochemical detection techniques form the analytical foundation of this project, both for cleaning and characterizing the electrode surfaces and for understanding the signal generation mechanisms relevant to the EG-FET biosensing platform. This section introduces the electrochemical principles underlying the measurement methods used in this work, including Electrochemical Impedance Spectroscopy (EIS), Cyclic Voltammetry (CV) and the basic operating principles of transistor-based sensing.

2.1.1 Electrochemical Impedance Spectroscopy

EIS is an electrochemical technique widely used for studying a variety of electrochemical systems, including biosensors.[31] In EIS, a small sinusoidal voltage signal is applied to a system over a broad range of frequencies while the resulting electrical response is measured.[31] In biosensing applications, EIS measurements are commonly performed in the presence of a redox couple, such as the ferri/ferrocyanide redox pair $[Fe(CN)_6]^{3-/4-}$, to probe biomolecular interactions at the electrode interface.[31] The redox probe enables charge-transfer processes that are sensitive to surface modifications induced by biomolecular binding, making the impedance response suitable for biosensing applications.[31] By analyzing the impedance response at different frequencies, information about electrochemical and interfacial processes occurring at different time scales can be obtained.[31] One of the main advantages of EIS is its ability to separate complex electrochemical behavior into individual processes with different characteristic time constants.[31] Fast electrochemical processes are mainly observed at high frequencies, while slower processes such as diffusion become dominant at lower frequencies.[31]

Impedance data obtained from EIS measurements can be represented using equivalent electrical circuits consisting of components such as resistors, capacitors, and

diffusion elements.[31] One of the most commonly used equivalent circuit models for EIS-based biosensing systems is the Randles circuit.[32] In this model, different electrochemical processes are represented by individual electrical elements whose combined response approximates the measured impedance behavior.[31] By fitting experimental impedance data to an equivalent circuit model, parameters related to electrochemical properties of the system can be estimated using dedicated fitting software.[31] Impedance data are commonly visualized using a Nyquist plot, where the imaginary component of the impedance is plotted as a function of the real component.[31] For a Randles-type equivalent circuit including diffusion, the high-frequency region typically forms a semicircle associated with charge-transfer kinetics, while the low-frequency region approaches a diffusion-dominated response often approximated by a 45° line.[31] The shape of the Nyquist plot can therefore provide qualitative information about electrochemical processes occurring at the electrode interface. An example of a typical Nyquist plot obtained from a Randles-type equivalent circuit including diffusion is shown in Figure 2.1.

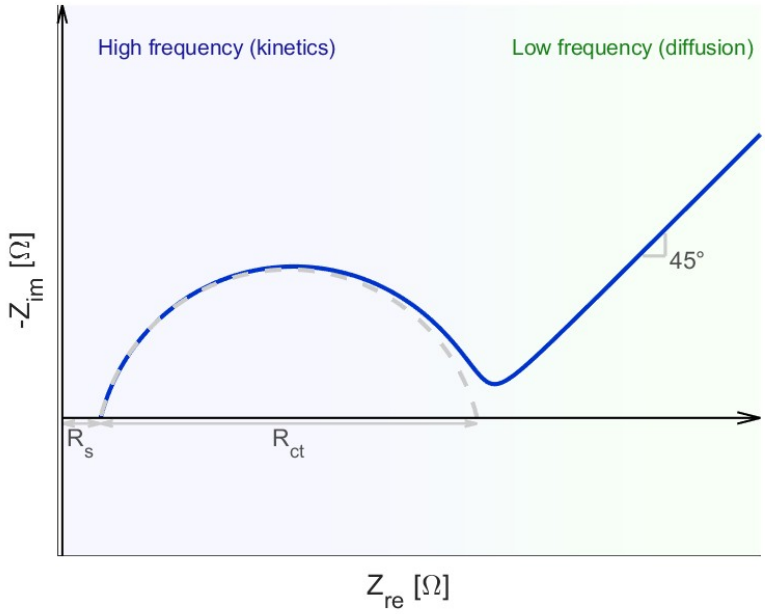

Figure 2.1: Example of a Nyquist plot obtained from a Randles-type equivalent circuit including diffusion model. The high-frequency semicircle is associated with charge-transfer processes at the electrode interface, while the low-frequency region reflects diffusion-related processes.

In a Nyquist representation, the high-frequency intercept corresponds to the solution resistance R_s, which appears as the starting point of the Nyquist curve on the real axis, while the diameter of the semicircle is related to the charge-transfer resistance R_{ct}.[31] [33] To quantitatively analyze the impedance response, the experimental data can be fitted to an equivalent electrical circuit model.[31] A typical diffusion-limited Randles-type equivalent circuit is shown in Figure 2.2, together with its corresponding fitting equation given in Equation 2.1.

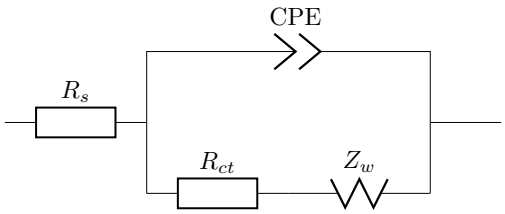

Figure 2.2: Typical diffusion-limited Randles-type equivalent circuit used to fit EIS data. The circuit consists of the solution resistance R_s, the charge-transfer resistance R_{ct}, the constant phase element (CPE) and the Warburg impedance Z_W.

$$Z = R_s + \frac{1}{\frac{1}{R_{ct}+Z_W} + Q(j\omega)^\alpha} \tag{2.1}$$

In Equation 2.1, R_s and R_{ct}, both expressed in [Ω], represent the ohmic resistance of the electrolyte and electrical contacts and the charge-transfer resistance at the electrode-electrolyte interface, respectively.[34] The term $Q(j\omega)^\alpha$ represents a constant phase element (CPE), which is commonly used instead of an ideal capacitor to describe non-ideal capacitive behavior in electrochemical systems.[34] [35] Here, Q is the CPE coefficient with units of $[\Omega^{-1}\, s^\alpha]$ and α is a dimensionless empirical exponent describing the deviation from ideal capacitive behavior.[35] The term j denotes the imaginary unit and $\omega = 2\pi f$ is the angular frequency. For an ideal capacitor, $\alpha = 1$, while lower values indicate increasingly non-ideal behavior.[35]

The diffusion-related contribution can be modeled using a finite Warburg element, Z_W, given by

$$Z_W(\omega) = \frac{1}{Y_0\sqrt{j\omega}} \tanh\left(B\sqrt{j\omega}\right) \tag{2.2}$$

where Y_0 is the diffusion-related parameter of the constant phase element formulation, with units $[\Omega^{-1}s^{1/2}]$.[31] B is a characteristic diffusion parameter defined as

$$B = \frac{\delta}{\sqrt{D}}$$

where δ is the diffusion layer thickness [cm] and D is the diffusion coefficient $[cm^2 \cdot s^{-1}]$.[31]

By defining the characteristic time constant as $\tau = B^2 = \delta^2/D$, the finite Warburg impedance can be written as

$$Z_W = \frac{\sigma}{\sqrt{j\omega}} \tanh\left(\sqrt{j\omega\tau}\right), \tag{2.3}$$

where σ is a re-parameterization of Y_0 capturing the magnitude of the diffusion-related impedance contribution expressed in units $[\Omega\, s^{-1/2}]$.

Equation 2.3 is algebraically equivalent to the original expression, but written in the parameterization used throughout this work. In this equation, σ is treated as a model parameter describing the magnitude of the diffusion-related impedance contribution, while τ is a characteristic diffusion time constant expressed in [s]. The finite Warburg element accounts for diffusion occurring over a finite diffusion length rather than assuming semi-infinite diffusion.[31] The hyperbolic tangent term therefore modifies the low-frequency behavior compared to an ideal semi-infinite Warburg response.

By fitting experimental impedance data to the equivalent circuit model, electrochemical parameters describing the electrode interface can be extracted, while the quality of the fit can be evaluated using the root-mean-square error (RMSE), which represents the overall deviation between the measured and modeled impedance values.[34] Since a constant phase element (CPE) does not represent an ideal capacitor, an effective capacitance, C_{eff}, can be estimated from the fitted parameters according to equation 2.4.[36]

$$C_{\text{eff}} = Q^{1/\alpha} \left(\frac{R_s R_{ct}}{R_s + R_{ct}}\right)^{(1-\alpha)/\alpha} \tag{2.4}$$

To evaluate the fitting quality relative to the magnitude of the impedance response, RMSE can be normalized with respect to the charge-transfer resistance according to

$$\text{Relative RMSE} = \frac{\text{RMSE}}{R_{ct}} \cdot 100\%. \tag{2.5}$$

To facilitate comparison between electrodes and reduce the influence of electrode-to-electrode variations, changes in charge-transfer resistance can be expressed as a relative percentage change between consecutive modification steps according to

$$\Delta R_{ct,\text{step}} = \frac{R_{ct,n} - R_{ct,n-1}}{R_{ct,n-1}} \cdot 100\% \tag{2.6}$$

where $R_{ct,n}$ and $R_{ct,n-1}$ denote the charge-transfer resistance obtained from the current and previous step, respectively.

2.1.2 Cyclic voltammetry

CV is an electrochemical method commonly used to monitor gradual changes on electrode surfaces between functionalization steps, or to clean and activate the surface of electrodes. [37] [38] [39] [40] [41]

When evaluating step-by-step surface modifications using CV, a redox couple such as ferri/ferrocyanide redox pair $[Fe(CN)_6]^{3-/4-}$ is commonly used to generate oxidation and reduction peaks in the voltammogram.[42] In CV, the electrode potential is swept linearly between two set limits and then reversed, forming a cyclic potential sweep while measuring the resulting current.[43]

The oxidation process gives rise to the anodic peak current (I_{pa}), while the reduction process produces the cathodic peak current (I_{pc}).[39] [42] During the potential sweep, oxidation and reduction reactions of the redox couple occur at the electrode surface, producing measurable current responses that depend on the accessibility of the electrode surface and the rate of electron transfer. Changes in peak shape or peak current between functionalization steps can therefore indicate changes occurring at the electrode interface.

When cleaning and activating gold electrodes, CV in sulfuric acid is commonly used, where repeated cycles are performed until a reproducible voltammogram is achieved.[40] [41] During these cycles, surface impurities may be removed while gold oxide species are repeatedly formed and subsequently reduced at the electrode surface through reversible oxidation and reduction processes. Stabilization of the cyclic voltammogram therefore indicates that the electrode surface has reached a more stable and reproducible electrochemical state, suitable for subsequent surface functionalization and electrochemical measurements.

2.1.3 Field Effect Transistors and Debye length

Transistors are fundamental components in modern electronics and are used to control or amplify electrical signals.[44] A Field Effect Transistor (FET) operates using three terminals, source (S), drain (D) and gate (G). The current flowing from source to drain (I_{DS}) is regulated by the voltage applied to the gate (V_{GS}).[45] Even small changes on V_{GS} can produce large variations in I_{DS}, making FETs highly sensitive devices.[46] There are two main types of FETs, N-type and P-type. In N-channel FETs, electrons act as negative charge carriers and I_{DS} increases with a more positive V_{GS}. While in P-channel FETs, it is the absence of electrons ("holes" in the material) that behave as positive charge carriers, causing I_{DS} to increase with a more negative V_{GS}.[45]

One important type of FET is the Junction Field Effect Transistor (JFET).[47] In semiconductor materials, P-type regions contain an excess of positive charge carriers ("holes"), while N-type regions contain excess electrons.[47] In an N-channel JFET, P-doped gate regions surround an N-type channel between the source and drain terminals, creating a PN-junction with the conducting channel.[47] When a more negative voltage is applied between the gate and source, the conducting channel

inside the transistor becomes narrower, which reduces the current flowing between the source and drain terminals.[47] When the depletion regions extend across the entire channel, the channel becomes fully pinched off and the current is reduced to approximately zero, the corresponding gate voltage is referred to as the pinch-off voltage or $V_{GS(\text{off})}$.[47] Most JFETs operate in depletion mode, meaning that the transistor conducts current at $V_{GS} = 0$ and is turned off by applying a gate voltage of the appropriate polarity, for N-channel JFETs, $V_{GS(\text{off})}$ is therefor negative.[47]

Transistors can be characterized using several different measurement configurations. One commonly used approach is to record transfer characteristics, where I_{DS} is measured as a function of gate-source potential V_{GS} at a fixed drain-source potential V_{DS}.[48] These measurements provide information about transistor behavior and can be used to determine parameters such as transconductance and operating conditions, where transconductance is defined as equation 2.7 below.[48] [49]

$$g_m = \frac{dI_D}{dV_{GS}} \tag{2.7}$$

In addition to transfer curve measurements, FET-based biosensors can also be operated during chronoamperometric measurements.[50] Chronoamperometry (CA) is an electrochemical method in which a fixed electrode potential is applied relative to a reference electrode while the resulting current is monitored over time.[51] By operating a FET during CA measurements, small electrochemical changes at the sensing surface can lead to amplified changes in the measured drain-source current due to the transistor's sensitivity to variations in gate potential. This is particularly promising for biosensor applications, where small electrochemical signals generated by low-concentration binding events can otherwise be difficult to detect. In an EG-FET design, an electrode is connected to the gate. The potential of the electrode changes upon attachment of biomarkers to it, leading to changes in V_{GS} which in turn changes I_{DS}, allowing real time monitoring of proportional changes in biomarker concentration.[29]

Debye length

The Debye length describes the characteristic distance over which electric charges are screened in an electrolyte solution.[52] If an analyte binds too far from the transducer surface, the associated electric potential may decay before reaching the sensor surface, thereby reducing the sensitivity of the measurement.[52] FET biosensors rely on target molecules being located within the Debye length so that changes in surface charge can effectively modulate the transistor signal.[53] Since conventional recognition elements such as antibodies are often significantly larger than the effective Debye length, this size mismatch can lead to substantial signal reduction and reduced detection sensitivity.[53] In biological environments with high ionic strength, the Debye length decreases according to Equation 2.8.[54]

$$\lambda_D = \sqrt{\frac{\varepsilon_0 \cdot \varepsilon_R \cdot R \cdot T}{2 \cdot F^2 \cdot I}} \tag{2.8}$$

where ε_0 [F m^{-1}] is the permittivity of free space, ε_R is the relative permittivity of the solvent, R [J mol^{-1} K^{-1}] is the gas constant, T [K] is the absolute temperature, F [C mol^{-1}] is Faraday's constant, and I [mol m^{-3}] is the ionic strength.[54]

For water under standard conditions, Equation 2.8 can be simplified to express the Debye length in [nm], provided that the ionic strength I is expressed in molarity [mol L^{-1}], according to

$$\lambda_D \approx \frac{0.304}{\sqrt{I}} \tag{2.9}$$

The Debye length depends on the ionic strength of the solution, which can be calculated according to Equation 2.10.[54]

$$I = \frac{1}{2} \sum c_i z_i^2 \tag{2.10}$$

where c_i is the concentration of ion i and z_i is its charge number. Since the ionic strength depends on the concentrations of all ions present in the solution, changes in pH can affect the ionic strength by altering the equilibrium concentrations of pH-dependent species, such as phosphate buffer components. To determine these concentrations, the Henderson-Hasselbalch equation can be used.[55]

$$pH = pK_a + log\frac{[A^-]}{[HA]} \tag{2.11}$$

By rearranging Equation 2.11, the ratio between deprotonated and protonated species can be expressed as

$$R = \frac{[A^-]}{[HA]} = 10^{(pH - pK_a)}$$

which gives

$$[A^-] = R \cdot [HA]$$

Using the total buffer concentration c_{tot},

$$\begin{aligned} c_{\text{tot}} &= [HA] + [A^-] \\ &= [HA] + R \cdot [HA] \\ &= [HA](1 + R) \end{aligned}$$

which can be rearranged to

$$[HA] = \frac{c_{tot}}{1+R} \tag{2.12}$$

Substituting Equation 2.12 into the expression for $[A^-]$ gives

$$\begin{aligned}[A^-] &= R \cdot \frac{c_{tot}}{1+R} \\ &= \frac{c_{\text{tot}} \cdot R}{1+R}\end{aligned} \tag{2.13}$$

These concentrations may then be used to calculate the total ionic strength of the solution according to Equation 2.10 and subsequently used in Equation 2.9 to calculate the Debye length.

2.2 Surface chemistry and functionalization

The performance of a biosensor is critically dependent on the chemistry used to modify and control the electrode surface. This section describes the principles underlying surface immobilization used in this project, including disulfide based attachment to gold, copper-free click chemistry and antifouling approaches to reduce non specific binding.

2.2.1 Gold surfaces in biosensors and sulfur–gold chemistry

Gold is widely used as an electrode material in immunobiosensors.[16][37][56][57] Its favorable properties for biosensing include biocompatibility and electrical characteristics that facilitate efficient electron transfer.[37] Gold is also considered chemically inert, which contributes to its stability as a platform for surface functionalization.[58] In addition, gold forms strong bonds with sulfur-containing ligands including thiols and dithiolane-based structures, providing high-affinity sites for immobilization of biomolecules such as antibodies used for biomarker detection.[58] These sulfur–gold bonds can, however, desorb at sufficiently negative potentials due to reductive processes [58], which is important to consider when applying negative potentials in electrochemical measurements. The same article further shows that molecules containing two sulfur atoms (dithiols) bind strongly to gold, supporting the use of dithiolane-derived linkers such as the lipoamide-based linker employed in this work.[58]

The linker used in this work is lipoamido-PEG4-azide, whose general chemical structure is shown in Figure 2.3.

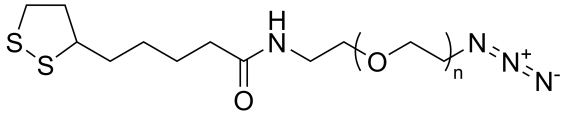

Figure 2.3: Chemical structure of the linker molecule lipoamido-PEG$_n$-azide, where n denotes the number of ethylene glycol repeat units in the PEG chain.
Created in BioRender. Frykberg, L. (2026) `https://biorender.com/rc8i92k`

When the linker contacts the gold surface, the dithiolane ring opens and allows one or both sulfur atoms to bind to the gold, resulting in a stable surface attachment. The azide group remains exposed and enables the subsequent copper free click chemistry. This surface chemistry is illustrated in Figure 2.4.

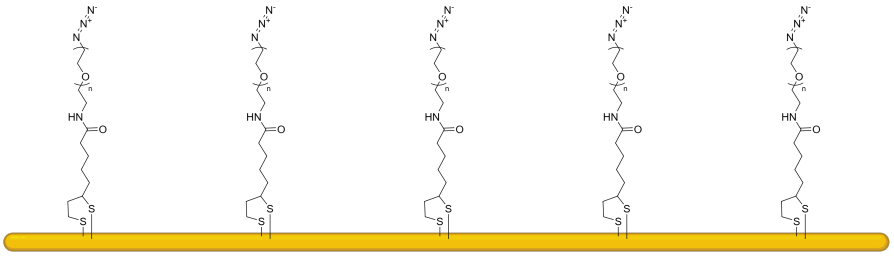

Figure 2.4: Schematic illustration of lipoamido-PEG$_n$-azide linker molecules immobilized on a gold surface through sulfur–gold interactions, forming the basis for subsequent surface functionalization. n denotes the number of ethylene glycol repeat units in the PEG chain.
Created in BioRender. Frykberg, L. (2026) `https://biorender.com/nk6vv7y`

2.2.2 Copper-free click chemistry

Copper-free click chemistry has become widely used in modern surface functionalization due to its high selectivity and compatibility with biological environments.[59] [60] [61]

The azide–alkyne cycloaddition forms a triazole product, but the uncatalyzed reaction proceeds too slowly at physiological or ambient temperatures in the absence of a catalyst, reflecting a low intrinsic reaction rate.[59] [61] The introduction of copper as a catalyst dramatically accelerates this transformation, establishing the classical copper-catalyzed "click chemistry" reaction.[59] [61] However, copper is toxic in living systems and therefore incompatible with applications involving biological environments.[59]

Ring strain can be used to accelerate the azide–alkyne reaction, as ring strain increases the reactivity of cyclic alkynes.[59] This forms the basis of strain-promoted azide–alkyne cycloaddition (SPAAC), a copper free click reaction in which a sufficiently strained cyclic alkyne reacts selectively with azides under mild conditions to form a stable triazole conjugate.[59] [60] [61] The driving force of SPAAC arises from the high strain energy of the cyclic alkyne, and rational design of these strained alkynes is therefore central to achieving fast and efficient reactions.[60] Dibenzocyclooctyne (DBCO) is a commonly used example of a strained cyclooctyne derivative developed according to these design principles.

In practical surface functionalization, DBCO-coupled molecules can react with azide-terminated linkers, such as the lipoamide-PEG4-azide used in this work, via SPAAC. The reaction proceeds rapidly and selectively, forming a stable triazole product without the need for a copper catalyst. The absence of copper catalysts reduces the risk of surface contamination and potential interference with subsequent electrochemical measurements. Figure 2.5 shows the general structure of the unbound click reagent used in this work, DBCO-PEG4-OH.

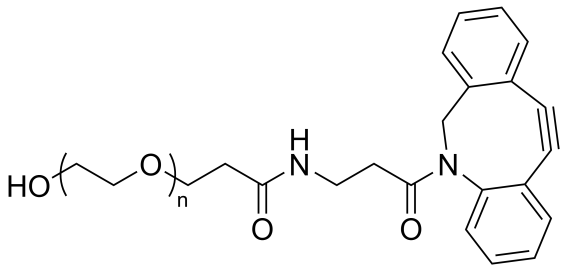

Figure 2.5: Chemical structure of a DBCO-PEG$_n$-OH click reagent.
Created in BioRender. Frykberg, L. (2026) `https://biorender.com/ooop8j5`

DBCO-PEG serves as a passivating molecule, as PEG chains reduce nonspecific adsorption of proteins and other biomolecules.[58] By minimizing unwanted interactions with the surface, PEG helps prevent false responses caused by nonspecific binding. In this work, DBCO-PEG served as a proof of concept for the developed surface functionalization protocol, as the same chemistry is intended to be employed for the future incorporation of Fab' fragments targeting the biomarkers $COMP^{156}$ and BGN^{262}, as described in Section 1.3. Figure 2.6 shows the triazole-linked PEG layer formed on a gold surface via SPAAC chemistry with DBCO-PEG.

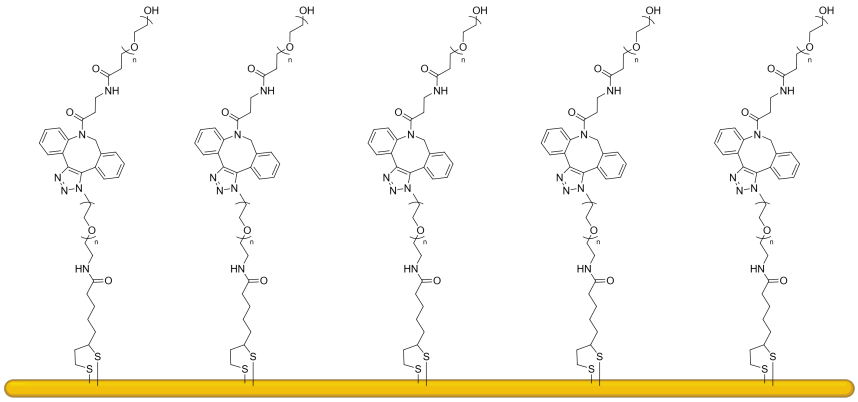

Figure 2.6: Schematic illustration of the triazole-linked PEG layer formed on a gold surface via SPAAC chemistry between surface bound azide-terminated linker and DBCO-PEG.
Created in BioRender. Frykberg, L. (2026) `https://biorender.com/2qs1mt2`

2.2.3 Non-specific binding and antifouling strategies

Saliva contains a broad range of biomolecules. These include nucleic acids, proteins, metabolites and microbial components, which makes it a valuable medium for disease screening and diagnostics.[62] This biochemical complexity, however, introduces challenges when measuring specific biomarker binding, as nonspecific adsorption can obscure the true analytical signal. Antifouling strategies therefore play a crucial role in ensuring that the measured response reflects specific interactions rather than background noise, even if an on site calibration against a control according to equation 1.2 were to be performed. As described in Section 2.2.2, PEG chains contribute to surface passivation. However, because DBCO-PEG must attach to a linker, and the linker mot likely does not fully cover the electrode surface, small uncovered regions may remain, allowing for nonspecific adsorption to occur. To minimize this, BSA is commonly introduced as an additional blocking agent.

BSA has attracted considerable interest as an antifouling agent due to its biocompatibility and ability to reduce nonspecific adsorption.[63] The antifouling properties of BSA are associated with its spherical conformation, amphiphilic surface, and multiple functional groups, which promote the formation of hydrated and sterically hindering surface layers that reduce nonspecific biomolecular adsorption.[63] BSA adsorption on gold surfaces has also been reported to form multilayer structures or continued adsorption beyond an initial monolayer, depending on conditions and surface chemistry.[64] This can allow BSA to contribute to coverage of exposed regions of the electrode surface that are not occupied by linker molecules or DBCO-PEG groups. Consequently, BSA blocking can reduce nonspecific adsorption and improve the selectivity of electrochemical biosensing measurements performed in complex biological samples such as saliva.

In addition, the net charge of BSA depends on the surrounding pH. Since the isoelectric point of BSA is approximately pI $\approx$ 4.7, BSA carries a net negative charge at physiological pH values above this point.[65] Knowledge of the BSA surface charge is relevant for the EG-FET sensing system, since negatively charged species near the transistor surface are expected to induce channel depletion in an N-type transistor, which under fixed bias conditions can lead to a reduction in the drain-source current. The presence of negatively charged BSA layers may therefore contribute to modulation of the electrical response during measurements. Figure 2.7 shows the fully functionalized surface created in this work.

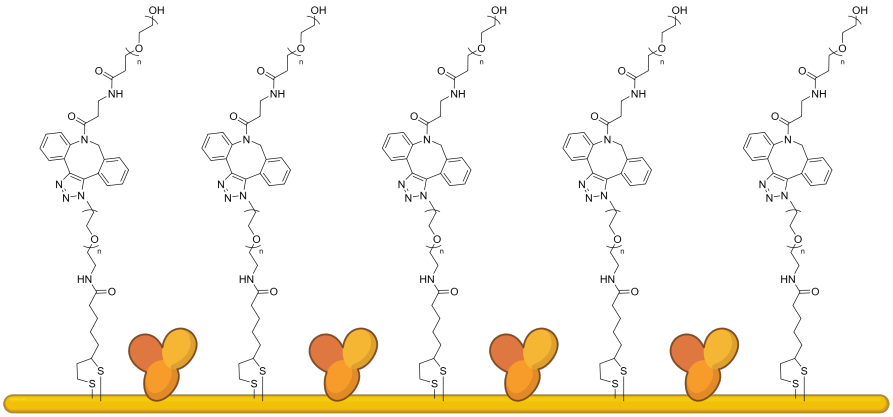

Figure 2.7: Schematic illustration of the fully functionalized surface, showing a triazole-linked PEG layer and subsequent BSA adsorption.
Created in BioRender. Frykberg, L. (2026) `https://biorender.com/zu5znjj`

In addition to serving as a proof-of-concept surface in this work, PEG-functionalized surfaces will also act as essential controls in the future sensor design. Such PEG-only surfaces enable quantification of nonspecific adsorption and allow on-site calibration by separating the specific signal arising from biomarker-Fab' binding events from the nonspecific background according to Equation 1.2 presented in Section 1.3. The PEG chain lengths suggested in the same section for both the linker and click chemistry are consistent with those intended for future functionalization of both the active and control surfaces.

3

Methods

The following chapter outlines the theoretical background, experimental setup, and practical procedures used in this work. It begins with the electrostatic considerations related to the Debye length, followed by the development and stability characterization of the EG-FET system. The subsequent sections describe the materials, fabrication steps and measurement procedures applied throughout the study.

3.1 Debye length

The concentrations used for calculating the ionic strength and the corresponding Debye length are provided in this section. The ionic strength was calculated at three different pH values: 6.0, 8.3 and 9.0. These values were selected based on the pH range reported in Table 5 of the article "*Straight from the horse's mouth: The effect of different feedstuffs on oral pH in horses and ponies*", where the measured oral pH ranged from 5.86 to 9.05, with a mean value of 8.28.[66]

Table 3.1 displays the concentrations of components measured in equine saliva.

Table 3.1: Mean electrolyte and urea concentrations in equine saliva before and 50 minutes post mastication of forage, adapted from Table 1 in the article "*Equine saliva components during mastication, and in vivo pH changes in the oral biofilm of sound and carious tooth surfaces after sucrose exposure*".[67]

Component	**0 min [mM]**	**50 min [mM]**
Na	5.75	10.6
K	22.2	34.4
Ca	1.37	2.71
P	0.26	0.37
HCO_3^-	27.1	27.5
Urea	2.67	3.17

Table 3.2 displays the standard concentration of components in PBS.

Table 3.2: Standard formulation of PBS (pH 7.4).[68]

Substance	**Concentration [mM]**
NaCl	137
KCl	2.7
Na_2HPO_4	10
KH_2PO_4	1.8

3.2 EG-FET development and stability characterization

During the initial phase of the project, preliminary experiments were conducted to evaluate transistor behavior, characterize the measurement setup and identify suitable operating conditions for the EG-FET sensing system. An EmStat Pico Development Kit was used to bias the transistor, perform electrical measurements and stream data to a computer via USB.

In this work, V_{GS} is defined as the potential applied by the EmStat Pico potentiostat between the working electrode (WE, acting as the gate electrode in the EG-FET configuration. See Section 3.2.1) and the reference electrode (RE). The counter electrode (CE) is included in the three-electrode setup on the SPE but does not contribute to the definition of V_{GS}. The drain-source bias V_{DS} is applied across the transistor's drain and source terminals, and the resulting drain current I_{DS} is recorded.

Several field-effect transistors (FETs) were screened to identify devices with high sensitivity within the voltage and current limitations of the EmStat Pico system ($\pm$2 V output range and $\pm$3 mA current compliance).[69] Sensitivity was assessed based on the modulation of drain current in response to changes in V_{GS} potential. Measurements were initially performed on a breadboard without any external electrode connected, allowing direct comparison of transfer characteristics with manufacturer datasheets. Based on these measurements, devices with the highest apparent sensitivity (i.e. strongest I_{DS} response to changes in V_{GS}) were selected within each transistor type for further evaluation.

A sensitive N-channel JFET (J113) was selected for further development. The depletion-mode operation of this transistor allows measurable drain current at $V_{GS} = 0$, which is advantageous in an exploratory biosensing context where the direction and magnitude of potential shifts at the gate are unknown. The transistor was biased to operate in the steep region of the transfer curve while maintaining sufficient dynamic range for drain current modulation within the limits of the EmStat Pico system. The selected bias conditions were $V_{GS} = -0.4, \mathrm{V}$ and $V_{DS} = 0.4, \mathrm{V}$ for subsequent chronoamperometric measurements. For transfer-characterization measurements, different bias conditions were used throughout the work. In the final

measurement protocol, the drain-source bias was set to ($V_{DS} = 0.6$ V), with a gate-voltage sweep range from (-1 V) to (0 V). Oscilloscope measurements confirmed that both V_{GS} and V_{DS} remained positive relative to ground during operation. The apparent negative bias applied via the EmStat Pico originates from its internal reference scheme, where potentials are defined relative to the instrument measurement channels rather than absolute ground.

To interface the transistor with an external electrode, a custom measurement setup was constructed. The system was enclosed in a grounded aluminium housing to reduce electromagnetic interference and coaxial cables were used between the enclosure and the SPE connector to minimize noise in the signal path. This configuration revealed stability limitations, where the introduction of the electrode and liquid interface led to noticeable electrical drift and reduced repeatability in the transfer characteristics measurements compared to the initial breadboard-mounted tests.

Short-term stability improvements were implemented through hardware modifications. These included the use of shorter coaxial cables and thermal stabilization of the transistor using a copper heat spreader with thermal paste. In addition, a relay-controlled reset circuit based on a Pickering 118-1A-3/2D reed relay was integrated and triggered via the EmStat Pico GPIO5 output to discharge accumulated charge prior to each transfer characteristics measurement.

A $1M\Omega$ resistor placed between CE and RE was evaluated as a potential discharge pathway but was not included in the final configuration. Transfer characteristics were used to extract the transconductance (g_m) as a performance metric.

Prior to the functionalization experiments, the measurement approach was transitioned from transfer-characterization measurements to chronoamperometry, which was subsequently used as the primary measurement method for the EG-FET system.

3.2.1 Schematic diagram EG-FET system

The schematic shown in Figure 3.1 outlines the complete EG-FET measurement set up, detailing the connections between the EmStat Pico, the Au-SPE and the J113 transistor. It also shows the integration of the Pickering 118-1A-3/2D relay used for charge reset functionality, together with the grounding layout and aluminium shielding enclosure used to minimize external interference.

The electrodes used in this work were all gold CTI Phase Zero SPEs bought from Conductive Technologies via PalmSens, with a WE diameter of 2mm, corresponding to a geometric surface area of approximately $3.14mm^2$. SPEs were selected due to their low cost, commercial availability and suitability for disposable biosensor applications. Their planar geometry and "easy to switch" configuration also simplified measurements. Figure 3.2 shows a picture of the type of Au-SPE used as the extended gate electrode platform in the EG-FET system.

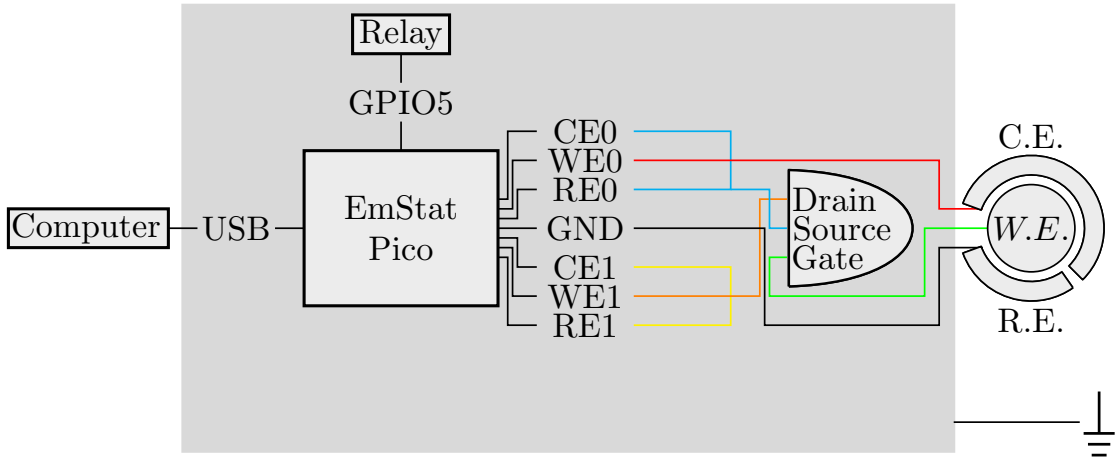

Figure 3.1: Schematic diagram of the complete EG-FET measurement system. Including the J113 transistor, the Emstat Pico, the relay-based discharge circuit, grounding connections and the aluminium enclosure used as electromagnetic shielding.

Figure 3.2: Photograph of Au-SPE used in the EG-FET system, the WE geometric area is approximately $3.14 mm^2$.

3.3 Materials and equipment

The following section provides an overview of the materials, chemicals, software tools and laboratory equipment used in this project. More detailed descriptions of each category are presented in the subsequent subsections.

3.3.1 Chemicals and reagents

The chemicals and reagents used in this work are listed in Table 3.3, together with supplier information and storage conditions. For the PDMS fabrication, a two component SYLGARD^{TM} 184 silicone elastomer system was used. Additional materials used throughout the experiments included MilliQ water, nitrogen gas and 96% ethanol.

Table 3.3: List of chemicals and reagents used in this project, including supplier information and storage temperature for each compound.

Name	CAS	Supplier	Storage temperature
Bovine serum albumine	9048-46-8	Sigma-Aldrich (Merck)	+4 °C
Phosphate buffered saline (pH 7.4)	-	Sigma-Aldrich (Merck)	RT
Sulfuric acid	7664-93-9	Sigma-Aldrich (Merck)	RT
Lipoamido-PEG4-azide	890016-39-4	MedChemExpress	−20 °C
Dibenzocyclooctyne-PEG4-alcohol	-	Sigma-Aldrich (Merck)	−20 °C
Potassium hexacyanoferrate(III)	13746-66-2	Sigma-Aldrich (Merck)	RT
Potassium hexacyanoferrate(II) trihydrate	14459-95-1	ThermoFisher	RT
Potassium chloride	7447-40-7	Sigma-Aldrich (Merck)	RT
Synthetic $COMP^{156}$	-	Saritha Adepu	−20 °C
Synthetic BGN^{262}	-	Saritha Adepu	−20 °C
Equine saliva	-	Saritha Adepu	−20 °C

3.3.2 Software

The software tools used in this project included ChemDraw, BioRender, PSTrace, MATLAB, AI tools and Overleaf.

ChemDraw was used to draw chemical structures, while BioRender was employed to design biomolecular illustrations and to convert vector graphics, .svg-files, into regular .jpg-format. All electrochemical measurements, including electrode cleaning procedures, were performed and logged in PSTrace. MATLAB was used for all data processing, including plotting, curve fitting and extraction of parameters. AI tools such as ChatGPT, Scopus and Microsoft Copilot were used as supportive tools to identify relevant literature, explore thoughts and ideas, refine scientific text and assist in the development of MATLAB code used for data processing. The report was written in Overleaf using LaTeX, which was also used to generate schematic diagrams such as the wiring layout in Figure 3.1 and the Randles circuit in Figure 2.2.

3.3.3 Instruments and equipment

The instruments and equipment used in this project included the developed EG-FET system, consisting of an EmStat Pico development kit, a J113 transistor and CTI Phase Zero Au-SPEs with a working electrode area of 3.14 mm^2. Additional equipment included a PalmSens3 potentiostat, an Eppendorf Multipette E3 (single-channel), standard laboratory pipettes (1000 μL, 100 μL and 10 μL), as well as a custom polydimethylsiloxane (PDMS) setup. The PDMS setup included a 3D-printed base plate for electrode placement, followed by a PDMS layer and a top plate with incubation reservoirs, enabling selective incubation of the working electrode on multiple electrodes simultaneously. This setup is further described in the following section.

3.3.4 PDMS mold fabrication

A custom PDMS mold was fabricated to enable selective functionalization of the WE on multiple electrodes simultaneously. The mold, bottom plate and top plate containing integrated incubation reservoirs with an approximate volume of 400 μL for selective isolation of the WE were all 3D-printed in PLA using ironing settings, forming a complete custom setup tailored for this project. The preparation of the PDMS and the corresponding CAD drawings relevant to the PDMS workflow are presented in this section.

PDMS was prepared using a two-component SYLGARD^{TM} 184 silicone elastomer system, consisting of a base and a curing agent mixed in a 10:1 ratio. A total of 55 g of PDMS was prepared by mixing 50.1 g of base with 5.4 g of curing agent. After manual mixing, the mixture was initially degassed in a vacuum chamber to reduce the amount of entrapped air bubbles before being poured into two separate molds with shapes and dimensions according to Figure 3.3. The filled molds were subsequently placed in a vacuum chamber and degassed until no visible air bubbles remained upon releasing the vacuum, a process that required approximately one hour. The molds were positioned on a level surface, verified using a spirit level, to ensure uniform curing. The PDMS was cured at room temperature for six days, as the PLA molds could not withstand elevated temperatures that else would reduce curing time. After curing, the PDMS structures were released from the PLA molds by cutting along the outer edges with a scalpel and carefully peeling them away.

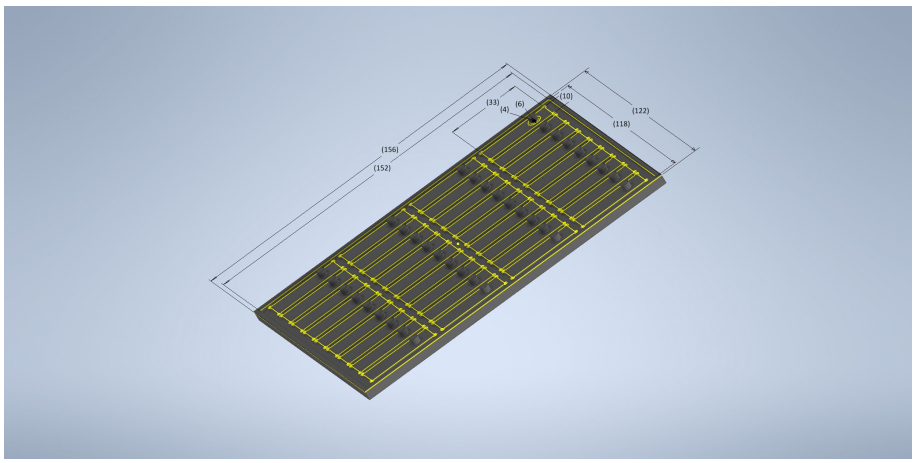

Figure 3.3: CAD drawing of the mold used for PDMS casting, including dimensions in [mm]. The raised central structures define the openings corresponding to the working electrode areas, while the surrounding recessed regions generate a thicker PDMS sealing region around each WE interface.

The mold geometry used for PDMS casting is shown in Figure 3.3. The raised central structures in the mold correspond to the position of the WEs of each SPE and were designed to create openings in the cured PDMS layer, thereby preventing PDMS coverage of the active WE surface. The mold created has space for a total of 36 electrodes. A recessed region surrounding each WE structure was included

to produce a locally thicker PDMS region around the WE interface. This design was intended to improve sealing performance during compression in the assembled setup.

The resulting PDMS layer can be represented as a negative replica of the mold geometry, shown in Figure 3.4, where the thicker sealing region surrounding the WE openings can be observed.

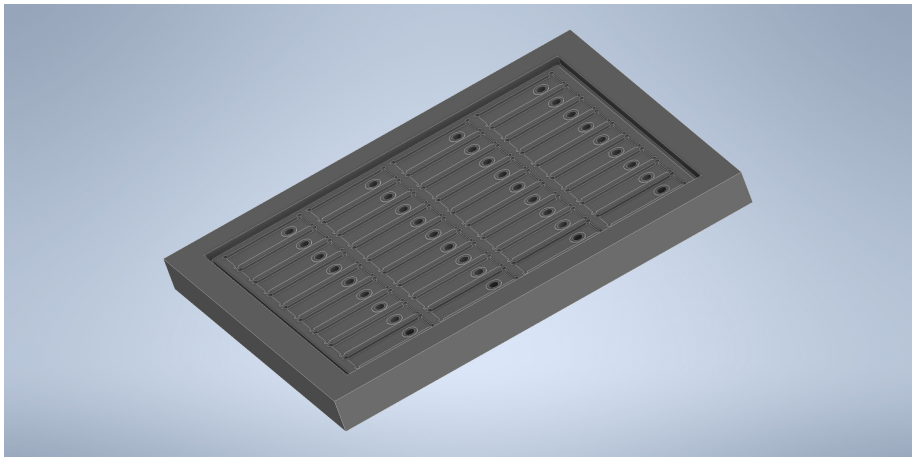

Figure 3.4: Negative replica of the mold geometry representing the resulting PDMS, including thicker sealing regions surrounding the openings around each WE.

The CAD drawing of the bottom plate used in the final PDMS assembly is shown in Figure 3.5. During assembly, the electrodes were positioned in the plate with their active surfaces facing upward. Recessed electrode pockets matching the electrode geometry, including rounded corners to ease insertion, were incorporated into the bottom plate to enable reproducible electrode positioning and to reduce movement of the electrodes during addition as well as compression with the PDMS layer. The recess depth was selected to improve mechanical stability while still maintaining sufficient compression of the PDMS to ensure proper sealing around each WE.

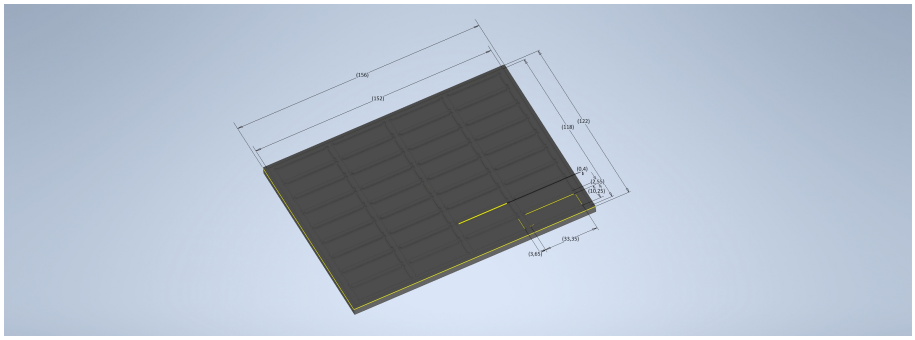

Figure 3.5: CAD drawing of the bottom plate used in the final PDMS assembly, including dimensions in $[mm]$. Recessed electrode pockets with rounded corners were incorporated to facilitate electrode insertion, improve reproducible positioning and reduce movement during addition as well as compression with the PDMS layer.

The CAD drawing of the alignment frame used in the final PDMS assembly is shown in Figure 3.6. The frame was designed to facilitate reproducible positioning of the PDMS layer during assembly and to mechanically secure the bottom and top plates relative to each other in the assembled setup.

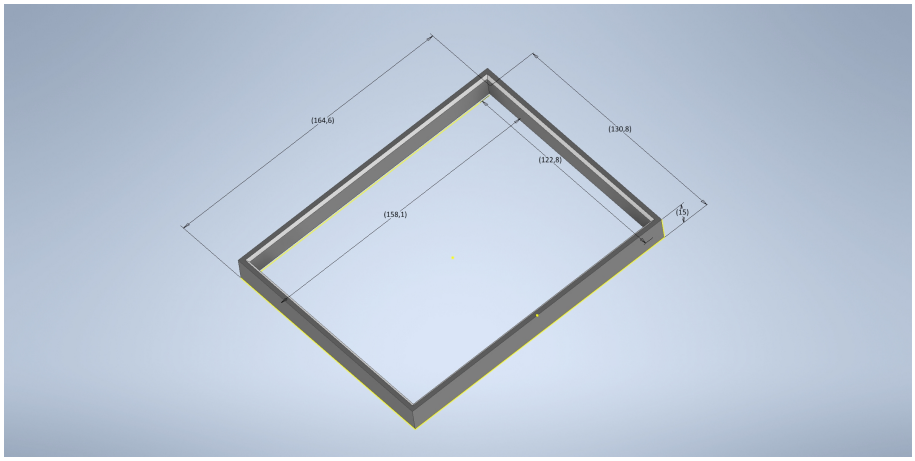

Figure 3.6: CAD drawing of the alignment frame used in the final PDMS assembly, including dimensions in $[mm]$. The frame was designed to guide placement of the PDMS layer and maintain alignment between the bottom and top plates during assembly and operation.

The CAD drawing of the top plate used in the final PDMS assembly is shown in Figure 3.7. The top plate contained integrated incubation reservoirs positioned above each WE, enabling selective exposure of only the WE surface to functionalization solutions during incubation. Each reservoir had an approximate volume of 400 μL.

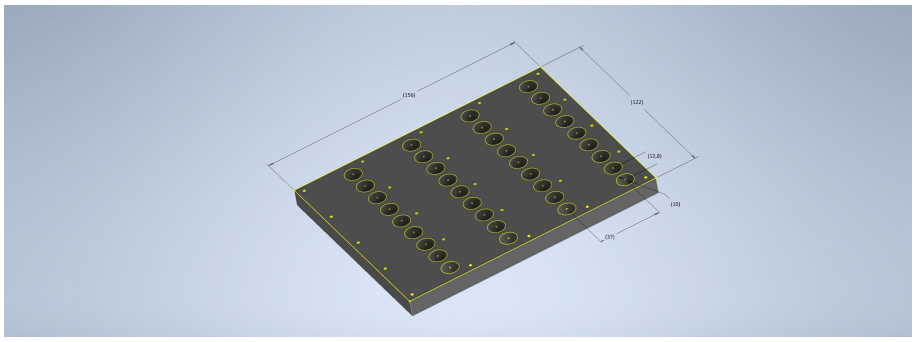

Figure 3.7: CAD drawing of the top plate used in the final PDMS assembly, including dimensions in $[mm]$. Integrated incubation reservoirs aligned with the WE positions enable selective functionalization during incubation. Each reservoir had an approximate volume of 400 μL.

The final PDMS setup used for electrode incubation on WE exclusively is shown in Figure 3.8.

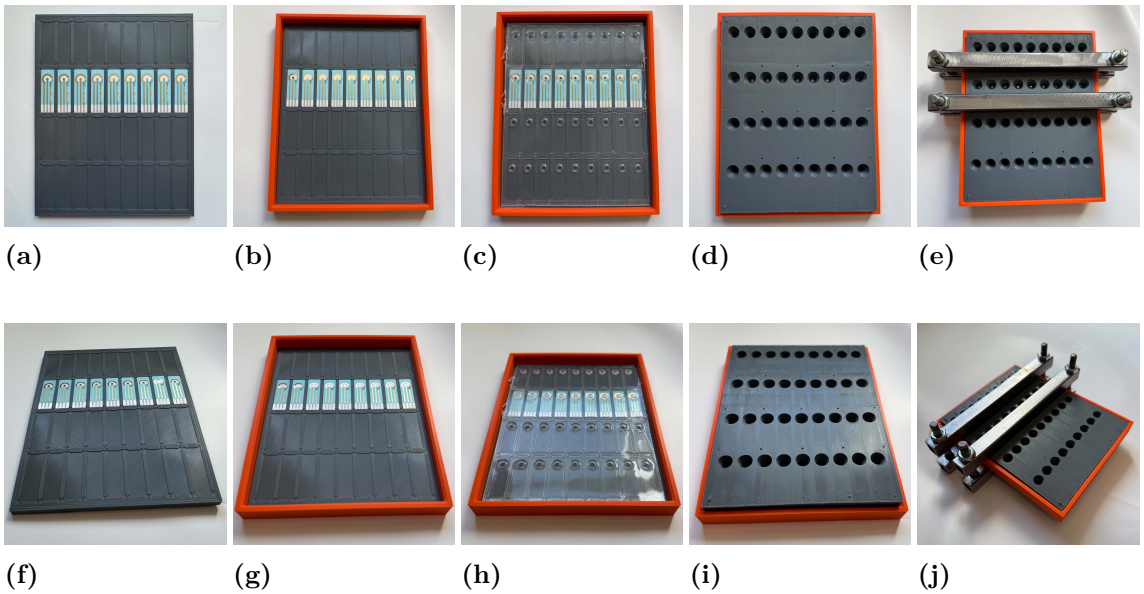

Figure 3.8: Top and side views of the assembled PDMS setup used for selective incubation on WE. Subfigures (a–e) show the set up from above, and subfigures (f–j) show the corresponding side views.

The assembly was performed in five steps. First, the electrodes were positioned in the bottom plate (a, f). A guiding frame was then added to ensure correct alignment of the PDMS layer and the top plate (b, g). The PDMS piece, designed to seal around WE of each electrode, was placed next (c, h). This was followed by the top plate containing funnels aligned only with WE of each electrode (d, i). Finally, the entire construction was clamped together to secure a tight seal during incubation (e, j).

3.4 Measurement procedures

The following section provides an overview of the measurement procedures used throughout the project, including instrument settings, preliminary tests, validation experiments, and the workflow for surface functionalization on the SPEs together with the data analysis used in this project. More detailed descriptions of each part of the measurement workflow are presented in the following subsections.

3.4.1 Settings

CV and EIS measurements were performed with a PalmSens3 potentiostat and CA measurements with the custom EG-FET system, all using predefined techniques for each type found in PSTrace, with parameter adjustments as specified below. Only the transfer characteristic measurements of the EG-FET system required a

custom MethodSCRIPT in PSTrace. This script was adapted from the example provided in the Application Note *PSAN-EmStat Pico Field Effect Transistor Characterization.*[70] Modifications of the script was mainly made to the potential ranges, sweep parameters, as well as the relay based discharging immediately prior to each measurement. The full MethodSCRIPTs used in this work are provided in Appendix A, this includes not only the script used for the transfer characteristic measurements but also the predefined PSTrace Techniques with the exact settings applied in this project for both CV, EIS and CA.

The CV cleaning procedure was performed using a 20s equilibration time, followed by potential cycling between −0.1V and +1.5V with a step size of 5mV and a scan rate of $100\text{mV}\,\text{s}^{-1}$. A total of 30 scans were recorded.

For the CV functionalization measurements, the same equilibration time was applied, but the potential window was adjusted to −0.5V to +0.5V, again using a 5mV step size, a scan rate of $100\text{mV}\,\text{s}^{-1}$, and three consecutive scans. The potential window was intentionally limited to $-0.5\,\text{V}$ to $+0.5\,\text{V}$ to minimize the risk of disrupting the surface-bound molecular layers during repeated measurements. Consequently, simplified procedures were used for determining I_{pc} and I_{pa}, as described in Section 3.4.7.

EIS measurements were carried out after a 45s equilibration period using a DC potential of 0.28V together with a 10mV AC potential. A total of 30 frequencies were recorded in the range from 50kHz down to 0.05Hz.

CA measurements were performed with no equilibration time and a constant gate voltage of −0.4V. The drain-source voltage was set to 0.4V, and the I_{DS} current was sampled every 0.1s over a total duration of 18 000s (5h) unless stopped.

The transfer-characteristic measurements were performed by applying a drain-source voltage of 0.6V while sweeping the gate voltage from −1.0V to 0V at a rate of $10\text{mV}\,\text{s}^{-1}$. Prior to each sweep, both V_{DS} and V_{GS} were set to zero, and a relay-based zeroing step was executed over the same gate interval using a faster $100\text{mV}\,\text{s}^{-1}$ sweep in order to reduce residual charge effects.

All measurements in this project were performed using PSTrace, an overview of the measurement systems used with corresponding settings can be seen in Table 3.4.

Table 3.4: Summary of electrochemical measurement settings used in this work.

Measurement	**Instrument**	**Solution**	**Main settings**	**Purpose**
CV cleaning	PalmSens3	0.5 M H_2SO_4	$t_{eq} = 20\,\text{s}$ $E_{V1} = -0.1\,\text{V}$ $E_{V2} = +1.5\,\text{V}$ $E_{step} = 5\,\text{mV}$ scan rate = $100\,\text{mV}\,\text{s}^{-1}$ $n_{scans} = 30$	Cleaning and electrochemical activation of Au-SPE
CV measurement	PalmSens3	$5\,\text{mM}\,K_3[Fe(CN)_6]$ / $5\,\text{mM}\,K_4[Fe(CN)_6]$ / 0.1 M KCl	$t_{eq} = 20\,\text{s}$ $E_{V1} = -0.5\,\text{V}$ $E_{V2} = +0.5\,\text{V}$ $E_{step} = 5\,\text{mV}$ scan rate = $100\,\text{mV}\,\text{s}^{-1}$ $n_{scans} = 3$	Monitoring electrode functionalization
EIS measurement	PalmSens3	$5\,\text{mM}\,K_3[Fe(CN)_6]$ / $5\,\text{mM}\,K_4[Fe(CN)_6]$ / 0.1 M KCl	$t_{eq} = 45\,\text{s}$ $E_{dc} = 0.28\,\text{V}$ $E_{ac} = 10\,\text{mV}$ $n_{freq} = 30$ $Max_{freq} = 50\,\text{kHz}$ $Min_{freq} = 0.05\,\text{Hz}$	Monitoring electrode functionalization
CA measurement	EG-FET system	Functionalization solution	$t_{eq} = 0\,\text{s}$ $V_{\text{GS}} = -0.4$ V $V_{\text{DS}} = +0.4$ V $t_{int} = 0.1\,\text{s}$ $t_{run} = 18000\,\text{s}$	Monitoring electrode functionalization
Transfer characteristics measurement	EG-FET system	Functionalization solution	$V_{\text{DS}} = 0.6$ V V_{GS}: -1.0 to 0 V V_{step}: 1V scan rate = 10 mV s^{-1}	EG-FET characterization

3.4.2 Preliminary tests

Preliminary tests were conducted to evaluate whether the same electrode could be used throughout the surface functionalization workflow for both EIS and EG-FET measurements, using transfer characteristics as the measurement mode for the EG-FET system. Cross exposure between different analytical fluids (EIS performed in redox solution and EG-FET directly on analyte), charging effects, or adsorption phenomena could influence subsequent measurements and was therefore

investigated.

Three gold electrodes were used to assess potential cross interference. One electrode was measured only with EIS, one only with the EG-FET system, and one was measured first with the transistor and then with EIS. After the initial measurements, all electrodes were incubated for one hour in a BSA solution prepared in PBS at a concentration of $10\,\mathrm{mg\,mL^{-1}}$. The same measurement sequence was then repeated for each electrode to evaluate whether both techniques could be applied to the same electrode without influencing the results.

To further investigate whether one technique affected the other, the electrode initially characterized with EIS was subsequently measured with the EG-FET setup and then again with EIS after the BSA incubation. This allowed assessment of whether the transistor measurement altered the EIS response. Similarly, the electrode initially measured with the EG-FET system was subsequently characterized with EIS and then again with the EG-FET to determine whether the EIS measurement influenced the transistor response. The design and outcome of these tests are presented in Section 4.3.

3.4.3 Validation of surface cleaning and activation

To validate the surface cleaning and activation procedure, CV measurements were performed in a ferri/ferrocyanide redox solution consisting of 5mM $K_3[Fe(CN)_6]/K_4[Fe(CN)_6]$/0.1M KCl. The procedure was done in triplicate. Each electrode was first measured in its initial, uncleaned state to establish a baseline response. The electrodes were then rinsed in three separate MilliQ baths and cleaned electrochemically in 0.5M sulfuric acid using CV. Thereafter, the electrodes were again rinsed in three consecutive MilliQ baths and measured according to the same procedure.

To investigate whether the wash buffer used in the ELISA protocols of both $COMP$[156] and BGN[262] could be applied in future workflows, the cleaned electrodes were incubated for one minute in 10mM PBS with 0.05%Tween-20. The short incubation time was chosen deliberately, as the solution is not intended as a storage medium but only as a wash buffer. To evaluate whether Tween-20 introduced non-specific adsorption or other effects that could influence the electrochemical response, after incubation, the electrodes were rinsed in three fresh Milli-Q baths and again measured according to the same procedure.

3.4.4 PDMS Leakage Assessment

To evaluate whether the PDMS wells provided sufficient containment during incubation steps, two electrodes were first cleaned in 0.5M sulfuric acid according to the cleaning protocol used for CV, rinsed in three Milli-Q baths and then measured in ferri/ferrocyanide redox solution (5mM $K_3[Fe(CN)_6]/K_4[Fe(CN)_6]$/0.1M KCl) according to the EIS protocol used. One electrode was then placed inside a PDMS well, while the other was left without PDMS to serve as a reference.

Both electrodes were then incubated for one hour in a BSA solution prepared at 10mg mL^{-1} in PBS. After incubation, the electrodes were rinsed in three consecutive MilliQ baths and measured again. This procedure allowed assessment of whether the PDMS setup influenced protein adsorption and thereby assessment of possible leakage during incubation.

3.4.5 Surface functionalization on SPE

Surface functionalization of Au-SPEs was carried out over three consecutive days. An overview of the funztionalization protocol can be seen in Table 3.5.

Table 3.5: Overview of the surface functionalization workflow performed over three days, including electrode state, measurements and incubation steps. CV and EIS were performed in triplicate, while CA was performed on a single electrode and only during functionalization steps (linker, click chemistry and BSA incubation), not during saliva measurements.

Day	Step	Electrode state	Measurement	Incubation / Action
1	Cleaning + linker	Bare, 0	CA/CV/EIS	Linker incubation initiated and continued overnight
2	Click reaction	Linker-modified, 1	CA/CV/EIS	DBCO-PEG incubation initiated and continued overnight
3 (step 1)	Passivation step	Click-functionalized, 2	CA/CV/EIS	BSA incubation (1 h)
3 (step 2)	Biological exposure	Fully functionalized, 3	CV/EIS	Saliva incubation (1 h)
3 (step 3)	Final readout	Post saliva, 4	CV/EIS	

On the first day, baseline measurements were performed on cleaned electrodes before the linker solution was added. On the second day, the linker-modified electrodes were measured again and subsequently incubated with the click-reagent. On the third day, the click-functionalized electrodes were measured, after which BSA was added for passivation and the electrodes were measured again to assess the BSA response. Finally, saliva was introduced and a last measurement was performed to evaluate nonspecific binding.

All functionalization steps were performed in triplicate for both CV and EIS, while CA was only done for one electrode due to time constraints. Two types of controls were included throughout the procedure: one unmodified electrode and one linker-only electrode. Both controls were kept in the corresponding solvent as the fully modified electrodes during all incubation steps to ensure that any solvent dependent effects on the electrochemical response could be distinguished from effects arising from surface chemistry. The linker only control also served to verify that the linker attachment step had been successful before proceeding with the full functionalization sequence. Furthermore, each functionalization step was evaluated relative

to the preceding surface state, which served as the primary control when assessing the effect of the subsequently added molecular layer.

Below shows the filename used for the CA electrode and Tables 3.6 and 3.7 summarize the electrode layout used in the PDMS set ups as well as the corresponding file name structure for both CV and EIS measurements. These tables provide an overview on how each electrode position was assigned, how the measurements were organized and how the resulting .csv files were stored.

CA electrode: GD1.CA.XXX

Table 3.6: Overview of file names and electrode placement in PDMS set up used for CV measurements.

GD1.CTRL. Linker. CV.XXX		GD1. Electrode_ 1.CV.XXX	GD1. Electrode_ 2.CV.XXX	GD1. Electrode_ 3.CV.XXX				GD1.CTRL. Bare. CV.XXX

Table 3.7: Overview of file names and electrode placement in PDMS set up used for EIS measurements.

GD1.CTRL. Linker. EIS.XXX		GD1. Electrode_ 1.EIS.XXX	GD1. Electrode_ 2.EIS.XXX	GD1. Electrode_ 3.EIS.XXX				GD1.CTRL. Bare. EIS.XXX

XXX =

- 0 = bare electrode
- 1 = linker
- 2 = linker + DBCO-PEG
- 3 = linker + DBCO-PEG + BSA
- 4 = linker + DBCO-PEG + BSA + saliva

All experiments and incubation times were performed at room temperature. Before each measurement, the conductive tracks on each electrode were dried carefully. New aliquots of linker, click-molecule and saliva were used during the functionalization. The redox solution and PBS were prepared on the first day and used throughout all three experimental days. Sulfuric acid was bought prepared, while linker, click-molecule and BSA were diluted immediately before use.

Day 1. The redox solution, 5mM K3[Fe(CN)6]/K4[Fe(CN)6] / 0.1M KCl, was prepared by dissolving 41.15mg potassium hexacyanoferrate(III), 53mg potassium hexacyanoferrate(II), and 373mg potassium chloride, and filling up to 50mL with MilliQ water. The solution was stirred until fully dissolved and subsequently degassed by continuous bubbling with nitrogen, this was maintained throughout the

laboratory day. At the end of the day, the nitrogen flow was stopped and the container was sealed with a cap. PBS was prepared by dissolving one tablet in 200mL MilliQ water. The PDMS mold was cleaned with MilliQ, dried with pressurized air and left to air dry.

The linker solution was prepared by dissolving approximately 20mg lipoamido-PEG4-azide in 10mL 96% ethanol, corresponding to an estimated linker concentration of approximately 5mM. Due to the highly viscous and oily nature of the linker, the exact transferred mass could not be determined with high precision. All electrodes except for the CA electrode were placed in the PDMS setup prior to linker addition to ensure functionalization only on the working electrode surface.

To minimize the time between electrode cleaning and linker application, all procedures were organized so that each electrode could be functionalized as soon as possible after preparation. The CA electrode was therefore started immediately after cleaning, and two separate PDMS setups were used to allow parallel processing of CV and EIS plates without delay. The bare control electrode, which was not intended to receive any linker, was cleaned first and consequently had the longest waiting time before receiving solvent in the PDMS setup. Electrode cleaning was done electrochemically using CV in 0.5M sulfuric acid.

The CA electrode was cleaned first, rinsed in three separate MilliQ baths, and immediately connected for chronoamperometric measurement, which was allowed to run continuously throughout the laboratory day. Directly after starting the measurement, 4000 µL of the linker solution was added to the cuvette. When the measurement was finalized, 2000 µL was removed to avoid incubation on the conductive tracks, the cuvette was sealed, and the electrode was left for overnight incubation.

While the CA measurement was ongoing, all electrodes intended for the CV plate were cleaned, rinsed in three separate MilliQ baths, and stored in MilliQ until the entire plate was ready. Baseline cyclic voltammetry measurements in redox solution of each CV electrode were then performed, followed by rinsing in three separate MilliQ baths and stored in MilliQ until the entire plate was measured. Once all CV baseline measurements were completed, the electrodes were placed in a PDMS setup and left for incubation overnight with 300 µL of linker solution added to each reservoir and sealed with parafilm.

After completing the CV workflow, all electrodes intended for the EIS plate were cleaned, rinsed, measured for baseline, rinsed, and incubated with linker in the same manner as the CV plate but in a separate PDMS setup.

Day 2. On the second day, the redox solution was bubbled with nitrogen for at least 20 minutes prior to the first measurement and then kept under continuous nitrogen bubbling until all measurements for the day was completed. When done, the nitrogen flow was stopped and the container was sealed with a cap. The click-reagent was prepared by dissolving 7.34mg DBCO-PEG4-OH in 12mL PBS, corresponding to a concentration of approximately 1.2mM.

The CA electrode was rinsed in three separate MilliQ baths, and immediately con-

nected for chronoamperometric measurement. Directly after starting the measurement, 4000 µL of the prepared click solution was added to the cuvette, and the measurement was kept running continuously throughout the laboratory day. When the measurement was finalized, 2000µL was removed to avoid incubation on the conductive tracks, the cuvette was sealed, and the electrode was left for overnight incubation.

While the CA measurement was ongoing, all electrodes intended for CV measurements were removed from the PDMS set up, rinsed in three separate MilliQ baths, and stored in MilliQ until the entire plate had been processed. Cyclic voltammetry measurements in redox solution of each CV electrode were then performed. Directly after measurement, the electrodes were again rinsed in three consecutive MilliQ baths and placed in sealed glass cuvettes containing 2000µL of the prepared click solution for overnight incubation. The cuvettes were labeled according to the electrode type they contained, and each cuvette was additionally marked with a "CV" and "EIS" side. This allowed both CV and EIS electrodes to be incubated in the same cuvette, necessary due to limited availability of reagents.

After completing the CV workflow, all electrodes intended for EIS measurements were handled in the same manner. They were removed from the PDMS set up, rinsed, measured, rinsed and and incubated with click solution in their corresponding cuvette.

Day 3. On the third day, the redox solution was again bubbled with nitrogen for at least 20 minutes before the first measurement and subsequently maintained under continuous bubbling throughout the laboratory day. BSA solution ($10\,\mathrm{mg\,mL^{-1}}$) was prepared by dissolving 0.5g BSA in 50mL PBS.

The CA electrode was rinsed in three separate MilliQ baths and immediately connected for chronoamperometric measurement. Directly after starting the measurement, 4000µL of the prepared BSA solution was added to its cuvette, and the measurement was kept running continuously throughout the laboratory day.

While the CA measurement was ongoing, all CV electrodes were sequentially rinsed in three separate MilliQ baths, measured using cyclic voltammetry in redox solution, rinsed again, and placed in sealed glass cuvettes containing 2000µL of the prepared BSA solution for incubation of approximately one hour.

After completing the CV workflow, the same procedure was repeated for the EIS electrodes.

During BSA incubation, the saliva sample was thawed. This pooled sample contained saliva from multiple horses and had previously been analyzed with ELISA, showing concentrations of $80\,\mathrm{ng\,mL^{-1}}$ for $COMP^{156}$ and $425\,\mathrm{ng\,mL^{-1}}$ for BGN^{262}.

After one hour of BSA incubation, CV electrodes were rinsed in three MilliQ baths, measured in redox solution, rinsed again, and placed in cuvettes containing 2000µL saliva sample for incubation of one hour. The same procedure was then repeated for the EIS electrodes.

After the final incubation, CV electrodes were rinsed in three MilliQ baths and measured the same way again, followed by the same procedure for the EIS electrodes.

3.4.6 Supplementary EG-FET CA Experiments

Supplementary chronoamperometric measurements were performed to explore how the EG-FET system responded during binding events other than the ones measured during the functionalization protocol. The aim was to evaluate whether the system could detect adsorption of BSA that has a known net charge below zero or any of the synthetic biomarkers, $COMP^{156}$ and BGN^{262}, on a bare electrode surface.

BSA measurements
CA measurements were performed to explore how the EG-FET system responded when BSA adsorption is applied directly on the electrode surface. A BSA solution with a concentration of $10\text{mg}\,\text{mL}^{-1}$ was used. Cleaned electrodes were prepared by CV in 0.5M sulfuric acid followed by rinsing in three consecutive MilliQ baths.

For each measurement, a CA recording was initiated on a gold electrode, after which the BSA solution was added to the cuvette to fully cover the active surface of the electrode. Four conditions were tested to evaluate the influence of electrode cleanliness and solvent: a cleaned electrode with BSA dissolved in PBS, a cleaned electrode with BSA dissolved in MilliQ (performed in duplicate), an uncleaned electrode with BSA dissolved in PBS and an uncleaned electrode with BSA dissolved in MilliQ.

Synthetic biomarker measurements
CA measurements were also performed using synthetic biomarkers of $COMP^{156}$ and BGN^{262}, each prepared at a concentration of $10\mu\text{g}\,\text{mL}^{-1}$ by diluting $10\mu\text{L}$ of $2\text{mg}\,\text{mL}^{-1}$ stock solution in 2mL solvent. All measurements were conducted on electrodes cleaned with CV in 0.5M sulfuric acid and subsequently rinsed in three consecutive MilliQ baths.

For each experiment, a CA recording was initiated on a cleaned bare gold electrode, after which the biomarker solution was added to the cuvette to fully cover the active surface of the electrode. Each biomarker was tested using two different solvents, resulting in four separate conditions: BGN^{262} dissolved in MilliQ, $COMP^{156}$ dissolved in MilliQ, BGN^{262} dissolved in PBS and $COMP^{156}$ dissolved in PBS.

3.4.7 Data analysis

All experimental data were exported directly from PSTrace in .csv file format and subsequently imported into MATLAB for analysis and visualization. The MATLAB scripts used for data processing of EIS and CV measurements are provided in Appendix B. CA and transfer characteristic transistor measurements did not undergo any additional numerical processing, the recorded data were simply plotted and compared.

The EIS data were fitted in MATLAB using circuit models based on the Randles circuit described in equations 2.1 and 2.3. Nonlinear least squares fitting was

performed using deterministic multistart optimisation in order to improve fitting robustness and reduce sensitivity to initial parameter estimates. The fitting procedure extracted parameters including R_s, R_{ct}, Q, α, σ, τ, C_{eff} and RMSE as well as relative RMSE and relative stepwise changes in R_{ct}. To improve fit quality, optional removal of edge data points at high and low frequencies was implemented. The maximum number of removable high frequency points was ten and the allowed number for low frequency points removal was manually defined for each dataset after visual inspection of the spectra and corresponding fits. No more than three low frequency points were allowed to be removed. Point removal was only accepted if the RMSE improved by at least 10%. All final fits were manually inspected to ensure physically reasonable behavior and agreement with the experimental spectra. Figure 3.9 shows examples of the circuit fitting applied to the EIS data.

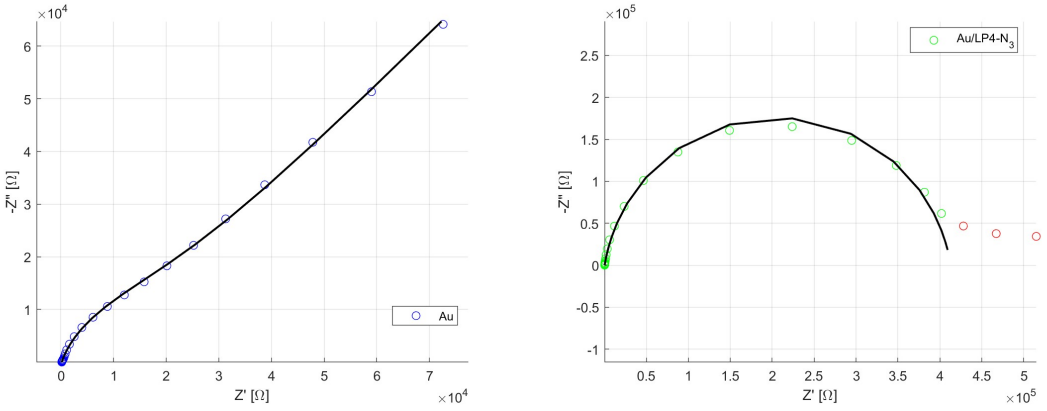

(a) **(b)**

Figure 3.9: Example of EIS fitting performed by MATLAB on (a) a bare gold electrode with no low frequency point removal allowed, and (b) a linker modified electrode where removal of up to three low frequency points was permitted to achieve the most accurate fit.

In Figure 3.9a, MATLAB achieves an almost perfect fit for the bare gold electrode without removing any data points. In contrast, Figure 3.9b shows an example where allowing the removal of up to three low frequency points was necessary to obtain a curve that closely followed the experimental data.

For CV, the MATLAB scripts identified I_{pa} and I_{pc} together with E_{pa} and E_{pc} directly from the measured data. The peak currents were extracted from the third (final) cycle of each voltammogram to ensure a stable electrochemical response. Peak currents were defined as the maximum anodic peak and the minimum cathodic peak, with no baseline correction, since the potential window became too narrow in later measurements to allow a consistent and comparable baseline fit across all functionalization steps. Relative stepwise changes in anodic and cathodic peak currents between consecutive measurements were subsequently calculated and used for comparison between functionalization steps. Figure 3.10 shows the peak detection procedure applied to CV data.

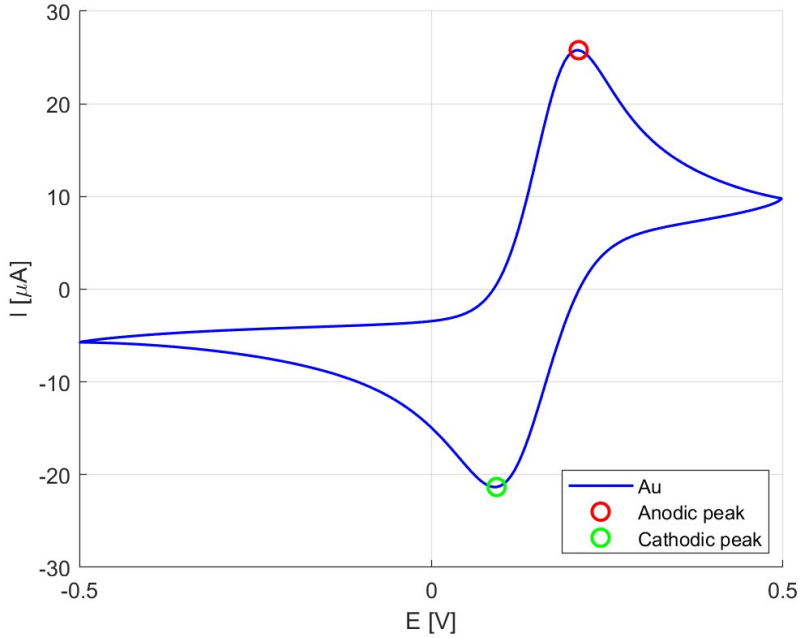

Figure 3.10: Peak detection performed by MATLAB on a bare gold electrode.

4

Results

This chapter presents the experimental results obtained throughout the project, beginning with the calculated Debye length for PBS, MilliQ and equine saliva. This is followed by an EG-FET development and stability characterization section moving over to the outcomes of all experimental stages in the subsequent sections: preliminary tests, validation of electrode cleaning and activation, assessment of PDMS leakage, the full surface functionalization sequence on SPEs, and the supplementary EG-FET chronoamperometric experiments.

4.1 Calculated Debye length

The ionic strength and corresponding Debye length of PBS, Milli-Q water and equine saliva samples described in Section 3.1 were calculated according to the equations presented in Section 2.1.3. The resulting values are summarized in Table 4.1.

Table 4.1: Calculated ionic strengths and corresponding Debye lengths for PBS, MilliQ water and equine saliva at different pH values and incubation times. For MilliQ water, no defined pH value was assigned due to the absence of buffering ions. The ionic strength and Debye length are therefore indicated qualitatively, approaching zero and infinity, respectively.

Sample	**Time [min]**	**pH**	I **[M]**	λ_D **[nm]**
PBS	-	7.40	0.167	0.740
MilliQ	-	-	$\to 0$	$\to \infty$
Equine saliva	0	6.00	0.0304	1.74
Equine saliva	0	8.30	0.0308	1.73
Equine saliva	0	9.00	0.0308	1.73
Equine saliva	50	6.00	0.0419	1.49
Equine saliva	50	8.30	0.0424	1.48
Equine saliva	50	9.00	0.0424	1.48

A difference of approximately 1nm in Debye length was observed between PBS and equine saliva due to their differing ionic strengths. Since the effective sensing range of the EG-FET is limited by the Debye length, these results indicate that ionic strength may significantly influence the transistor response in future measurements.

Variations within equine saliva resulted in less than 0.3nm difference in Debye length, while pH variations produced only minimal effects with a maximum difference of 0.01nm. The estimated Debye length of approximately 1.5–1.7 nm in equine saliva obtained here suggests that the intended binding event distance of approximately 6 nm with future Fab' fragments described in Section 1.3 lies outside the effective sensing range of the system. This indicates that further optimization of the surface architecture or linker design may be necessary to obtain a detectable signal in the EG-FET system when detecting biomarker binding events.

The pooled saliva sample used during the functionalization experiments contained saliva from multiple horses and had previously been analyzed using ELISA, showing concentrations of 80 ng mL^{-1} for $COMP^{156}$ and 425 ng mL^{-1} for BGN^{262}. The pH of the saliva sample was estimated using pH indicator paper, with the result shown in Figure 4.1.

Figure 4.1: pH indicator paper measurement of the equine saliva sample used during the functionalization experiments.

The measured saliva pH was estimated to be approximately 8-8.5, with an accuracy of ±0.2 pH units. Based on the calculated ionic strengths presented in Table 4.1, this corresponds to an estimated Debye length in the range of 1.48-1.73nm depending on the ionic composition of the sample.

4.2 EG-FET development and stability characterization

This section presents the results obtained during the EG-FET development and stability characterization described in Section 3.2.

Repeated transfer-characterization measurements of individual transistors on the

breadboard showed good repeatability, with only minor variations between runs. These variations were not visually distinguishable in the transfer curves and were therefore only identified through subsequent data analysis. Device sensitivity was assessed by analyzing the modulation of I_{DS} in response to changes in V_{GS}. A strong current response to small variations in gate potential was considered desirable for biosensing applications, as it indicates high transconductance and increased signal amplification capability.

When the transistor was connected to the external Au-SPE, measurements were performed with the electrode immersed in liquid to reduce capacitive noise and baseline instability observed when operating the electrode in air. This configuration enabled evaluation of how the presence of the electrode and its surrounding liquid environment influenced the transistor response compared to the initial breadboard-based measurements. Introducing the electrode and liquid interface resulted in reduced repeatability and the emergence of time-dependent variations in the transfer characteristics. Repeated measurements of the same configuration frequently exhibited a horizontal shift in V_{GS} while maintaining a similar curve shape, indicating instability in the measurement system.

A range of possible sources of instability were evaluated, including capacitive charging effects, grounding and shielding conditions, thermal effects and the mechanical design of the electrode holder. Initial tests focused on the electrode holder, however, repeated measurements using the same electrode configuration without changing its position in the holder still exhibited lateral drift in the transfer characteristics. To further investigate the origin of the observed behavior, control measurements were performed using discrete capacitors (100 pF, type 101J) connected between the WE, RE and CE terminals instead of an electrode. These measurements produced a similar form of drift, suggesting that part of the observed instability was likely related to the electrical measurement system. However, the behavior of a discrete capacitor does not fully replicate that of an electrode in an ionic medium. In electrolyte solutions, the high ionic strength provides a resistive pathway that helps discharge accumulated capacitive charge, creating a filtering effect that is absent when only capacitors or MilliQ is used as surrounding solvent. As a result, direct comparison between these cases should be interpreted with caution. Despite this, drift was still observed when measurements were performed in PBS, indicating that increased ionic strength alone was insufficient to eliminate all drift.

Observations also indicated that the reference electrode was not fully reset to ground potential during the controlled reset circuit, likely due to limitations in the measurement hardware. Temperature dependence of the transistor response was evaluated through CA measurements at fixed bias conditions. A weak dependence on temperature was observed, with lower device temperatures corresponding to a slight increase in I_{DS}, order of $\sim 0.01\mu$A.

Stability improvements implemented during the study reduced the magnitude of the drift, although complete elimination of drift was not achieved within the scope of this work. An example of the observed behavior is shown in Figure 4.2.

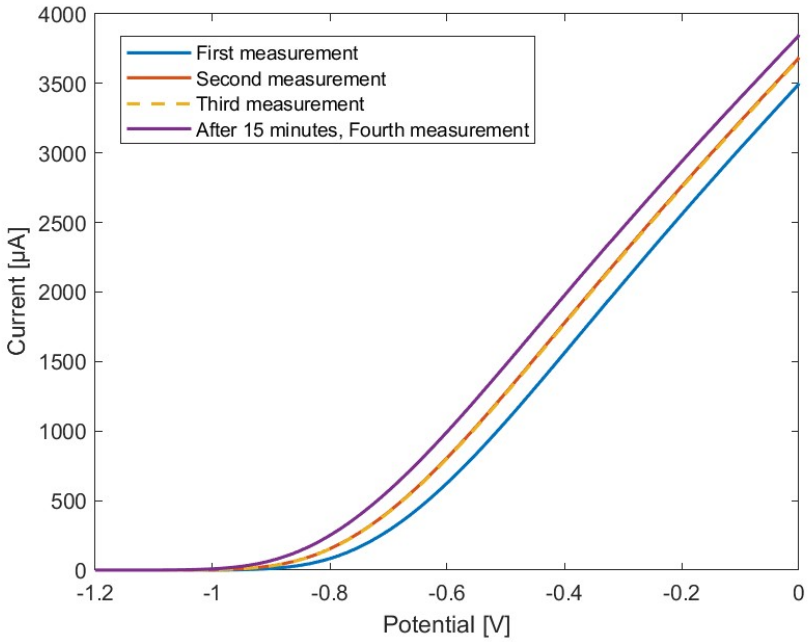

Figure 4.2: Example of lateral drift in the transfer characteristics of the EG-FET system, showing a horizontal shift in V_{GS} between repeated sweeps with $V_{DS} = 0.4$V

Due to the variations in I_{DS} observed between different measurement sessions, subsequent analysis of the transfer characteristics was based on the slope of the curves rather than on absolute current levels at fixed gate potentials. The local slope of the transfer curve remained consistent even when horizontal shifts in V_{GS} were present. Therefore, the transconductance provided a more reproducible parameter. Binding events at the gate interface of the electrode were expected to alter the effective gate potential, thereby shifting the operating point of the transistor. Such a shift would, according to Equation 2.7, influence the transconductance and result in a corresponding change in the slope of the transfer curve. This behavior is analogous to the effect observed when varying the set bias of V_{DS}. An example of how the slope varied with different values of V_{DS} is shown in Figure 4.3.

Repeatability analyses were performed to evaluate how experimental variations within the setup, including electrode exchange, solution replacement and cuvette handling, affected the extracted slope and its standard deviation. These measurements were performed in PBS and the results are presented in Appendix C.

Before the full functionalization experiments were initiated, transfer-characterisation measurements were discontinued and chronoamperometry was selected as the primary measurement method for the EG-FET system. This decision was based on early CA measurements, which did not exhibit the pronounced drift observed in the transfer-characterisation measurements. Across all CA measurements performed throughout the project, drift-like behavior was observed only once, shown in Figure 4.4. In that instance, the system stabilized after three rapid consecutive CA start-ups, after which the effect did not reappear.

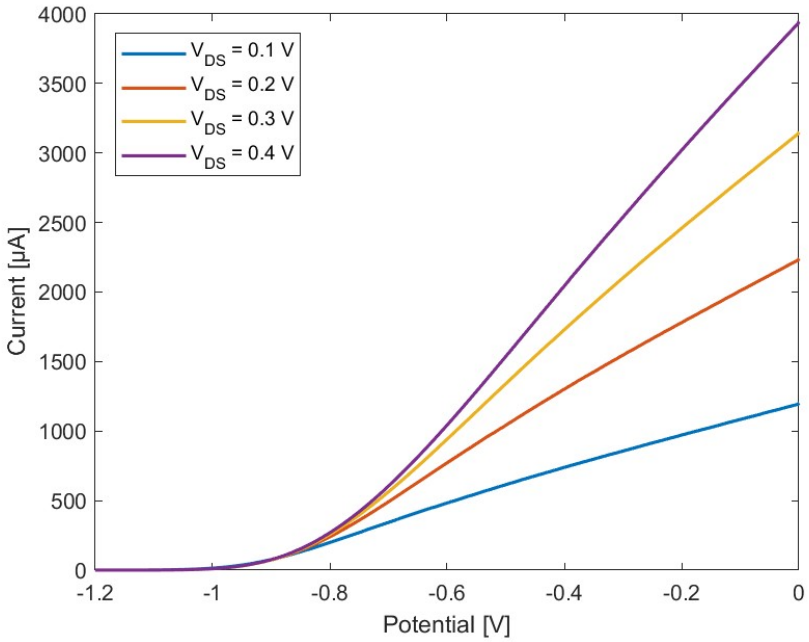

Figure 4.3: Transfer characteristics measured at different set V_{DS}, illustrating how the chosen drain–source bias affects the slope of the curve.

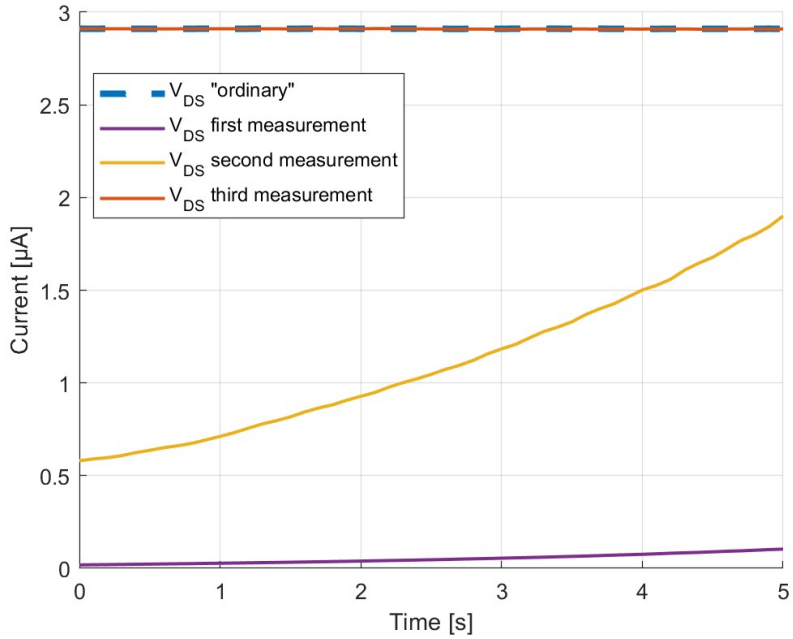

Figure 4.4: The only instance of drift-like behavior observed during CA measurements. After three rapid consecutive CA sweeps, the system stabilized and the drift did not reappear.

Over time, it also became clear that CA performed during binding events provided more direct information on changes in I_{DS} compared to transfer character-

istics measurements performed at equilibrium. In CA, shifts in I_{DS} are observed during the binding process, whereas at equilibrium the current returns towards its initial baseline value as further discussed in Section 4.7. Because the transistor responds to changes in effective gate potential in the same way regardless of measurement method the later findings in CA behavior indicated that equilibrium based measurements, whether performed via transfer sweeps or CA, would not retain any binding-related signal changes. This suggested that CA was better suited for capturing time-dependent binding events in the effective gate potential and motivated the decision to rely exclusively on CA for all functionalization and supplementary experiments.

4.3 Preliminary tests

The results of the preliminary experiments described in Section 3.4.2 are presented below. The combined electrode measurements are shown in Appendix D. However, no interpretable conclusions could be drawn from the data of the combined electrode, as it was not possible to determine whether one measurement method influenced the other.

The results from the EIS electrode are shown in Figure 4.5.

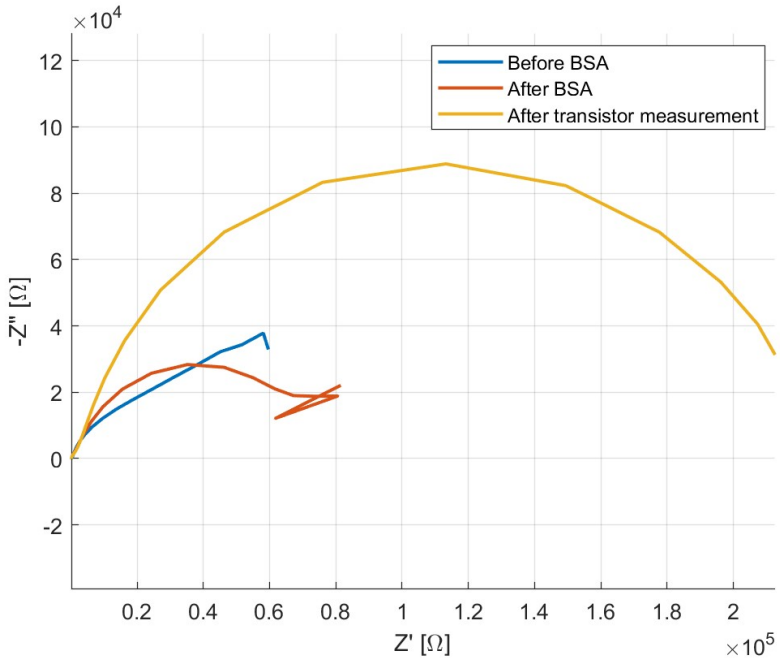

Figure 4.5: EIS measurements on the EIS electrode. Three measurements were performed: first before BSA incubation, then after 1h incubation in BSA, followed by an EIS measurement after the electrode had been subjected to a transistor measurement.

A clear effect of the binding of BSA is observed. Additionally, preceding transistor

measurement showed that the impedance increased drastically after the transistor test, and the EIS graph no longer overlaped with its preceding curve measured after incubation with BSA. This indicates that the transistor measurement perturbed or charged the electrode surface.

The results from the EG-FET electrode are shown in Figure 4.6.

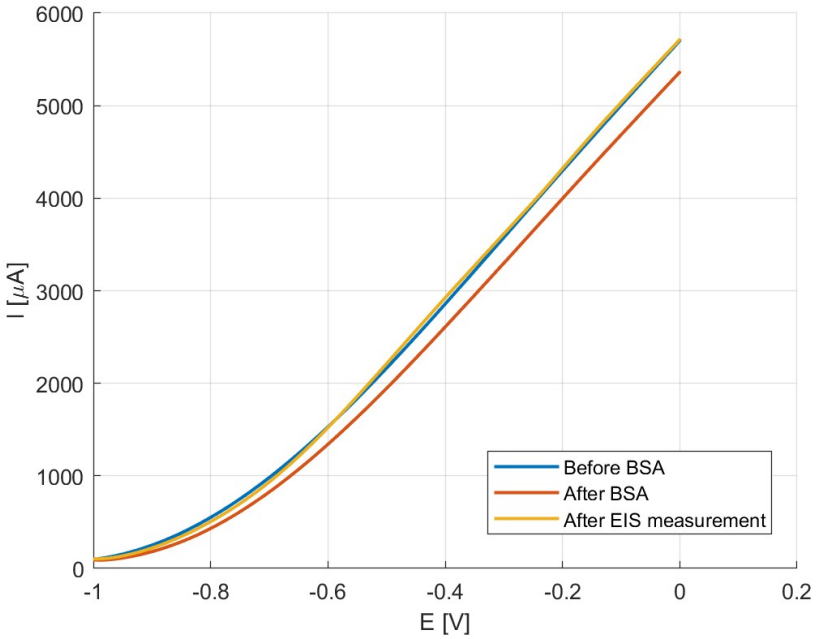

Figure 4.6: Transfer characteristics measurements on the EG-FET electrode. Three measurements were performed: first before BSA incubation, then after 1h incubation in BSA, followed by a transistor measurement after the electrode had been subjected to an EIS measurement.

Here, the apparent shift after BSA incubation cannot be confidently attributed to binding, since the observed change could equally well arise from lateral drift caused by the uncertainty in the EG-FET system. The influence of the EIS measurement is less pronounced but still visible, as the transfer curve measured after EIS measurement does not overlay with its preceding curve measured after BSA incubation. The curve has not only laterally shifted as usual but also cross the blue curve measured before incubation with BSA, indicating that the EIS measurement perturbed or charged the electrode surface.

Based on these results, it was decided to not combine multiple measurement techniques on the same electrode during later functionalization experiments. This decision was made to avoid cross method interference and to ensure that the extracted parameters could be trusted. As described in Section 3.2, transfer characteristic measurements were not used in subsequent experiments with the custom EG-FET system. Instead, only CA measurements were performed with the transistor based setup.

4.4 Validation of surface cleaning and activation

The results of the cleaning tests described in Section 3.4.3 are presented below. These tests were performed in triplicate and one representative dataset is shown here, while the remaining two are provided in Appendix E.

A typical cleaning cycle can be seen in Figure 4.7. During the cleaning cycles, the CV curves become increasingly overlapping with each cycle, indicating that the electrode surface approaches a stable and reproducible state. This behavior is expected for successful electrochemical cleaning, as repeated cycling removes surface contaminants and gradually exposes a more homogeneous gold surface.

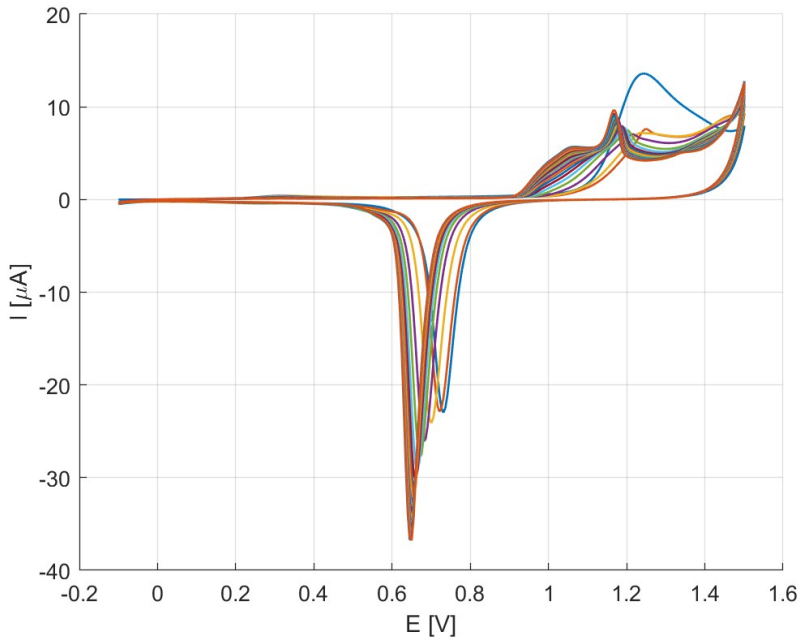

Figure 4.7: Typical cleaning cycle consisting of 30 CV scans in 0.5M sulfuric acid.

Prior and subsequent CV measurements on the same electrode are shown in Figure 4.8. The effect of the cleaning is clearly visible. The peak currents increase and the voltammogram becomes less flattened, indicating improved electron transfer kinetics and a cleaner, more electrochemically active surface. The short incubation in the wash buffer containing Tween-20 produces a curve that nearly overlaps with the post cleaning measurement, suggesting that the buffer does not adsorb to the surface or hinder electron transfer. This confirms that the wash buffer could be used in future experiments without affecting the electrode response if desired, although it was not applied further in this project.

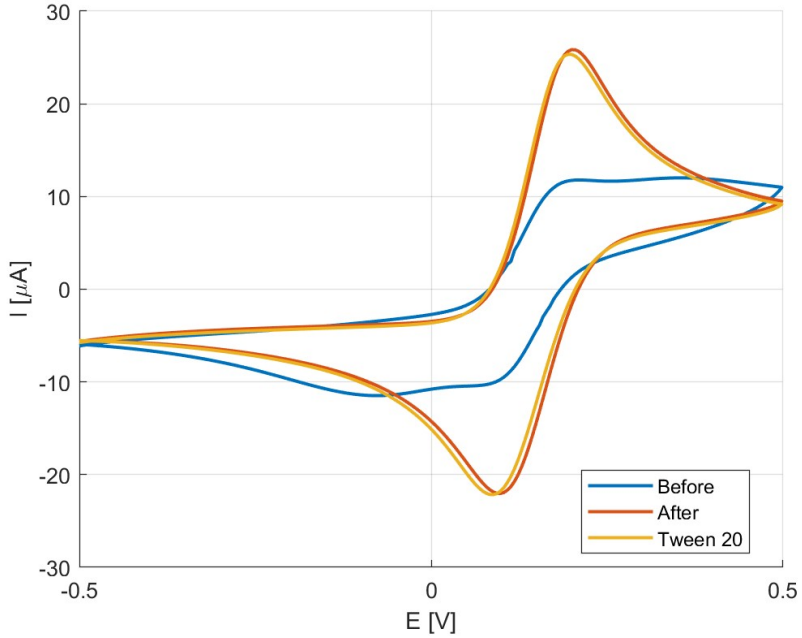

Figure 4.8: CV measurements in 5mM K3[Fe(CN)6]/K4[Fe(CN)6] / 0.1M KCl before cleaning, after cleaning and after 1 min incubation in 10mM PBS with 0.05%Tween-20.

4.5 PDMS Leakage Assessment

The results from the PDMS leakage experiments described in Section 3.4.4 are shown in Figure 4.9. A clear difference is observed between the electrode that was fully exposed to BSA and the electrode where only the WE was exposed through the PDMS. After BSA incubation, both electrodes show less diffusion dominated graphs compared to the graphs measured prior to BSA exposure. However, the electrode with full exposure exhibits a substantially larger semicircle than the electrode that had been restricted to only WE exposure during BSA incubation, indicating a stronger blocking effect due to more extensive BSA adsorption. In contrast, the electrode kept under PDMS shows a smaller increase in the semicircle, consistent with BSA binding restricted to the WE area. This indicates that the PDMS seal was sufficiently tight and prevented leakage or lateral diffusion of BSA underneath the PDMS. However, as this experiment was not performed in triplicate and electrode to electrode variation cannot be ruled out, further testing would be required to confirm the PDMS performance.

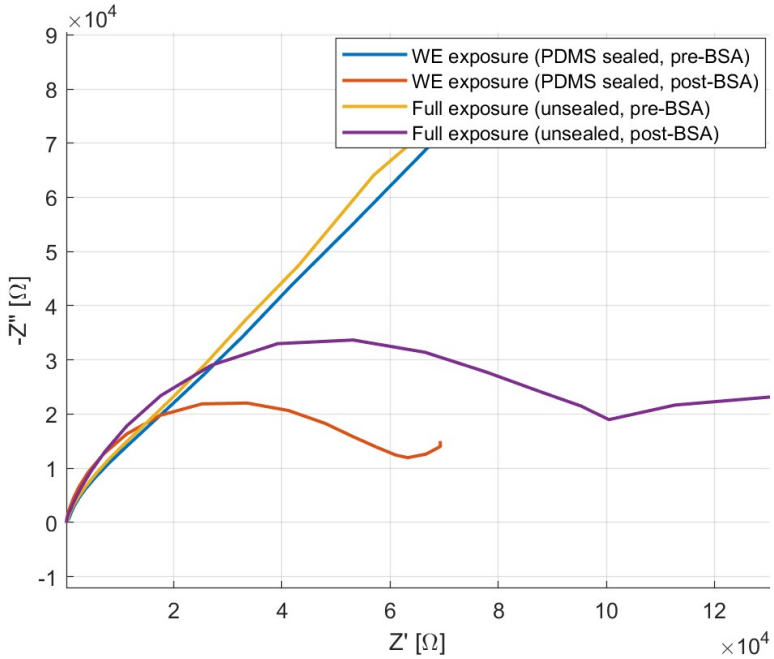

Figure 4.9: EIS measurements used to assess PDMS leakage, measured before and after 1 hour incubation with BSA. One electrode was fully exposed to BSA, while the other was inside a custom PDMS set up with only WE exposed.

4.6 Surface functionalization on Au-SPEs

This section presents the results of the surface functionalization described in Section 3.4.5. Fully modified electrodes were prepared in triplicate, and both controls as well as electrode 1 for each measurement technique (CV and EIS) are presented here. Electrodes 2 and 3 for both CV and EIS are shown in Appendix F and follow the same trends as electrode 1, which is discussed later in this section. The results indicate successful linker immobilization on all eight electrodes that underwent this step, as well as successful click reaction functionalization on all six electrodes subjected to that procedure.

All EIS fits yielded a relative fitting error below 5%, with the exception of the measurement done after incubation with saliva on electrode 2, where the fit quality was poor and the relative fitting error reached 48.681%. Although removing a single low frequency data point reduced the relative fitting error below 5%, the resulting fit in that case did not follow the experimental data. Therefore, no low frequency points were removed for this electrode.

4.6.1 Overview of electrode groups and experimental workflow

To improve readability of figures and tables throughout this section, a list of commonly used abbreviations is provided in Table 4.2.

Table 4.2: List of abbreviations used in figures and tables.

Abbreviation	**Meaning**
LP4-N_3	Lipoamido-PEG4-azide
DP4-OH	DBCO-PEG4-OH
BSA	Bovine serum albumin
EtOH	Ethanol
PBS	Phosphate buffered saline

The experimental workflow followed a stepwise surface modification protocol applied to both fully modified electrodes and control electrodes. All electrodes were first measured in their bare state, followed by sequential incubation steps as illustrated below:

Bare Au → Linker incubation → Click incubation → BSA blocking → Saliva incubation

All electrodes followed the same general workflow, although control electrodes were excluded from specific modification steps depending on the control type and only exposed to the corresponding solvent during incubation steps.

4.6.2 Functionalization sequence for fully modified electrodes

Electrode 1 is used as a representative example for the fully modified electrodes, as all three electrodes showed similar trends (see Appendix F).

All CV measurements for electrode 1 are shown in Figure 4.10, and the corresponding peak potentials and peak currents are summarized in Table 4.3.

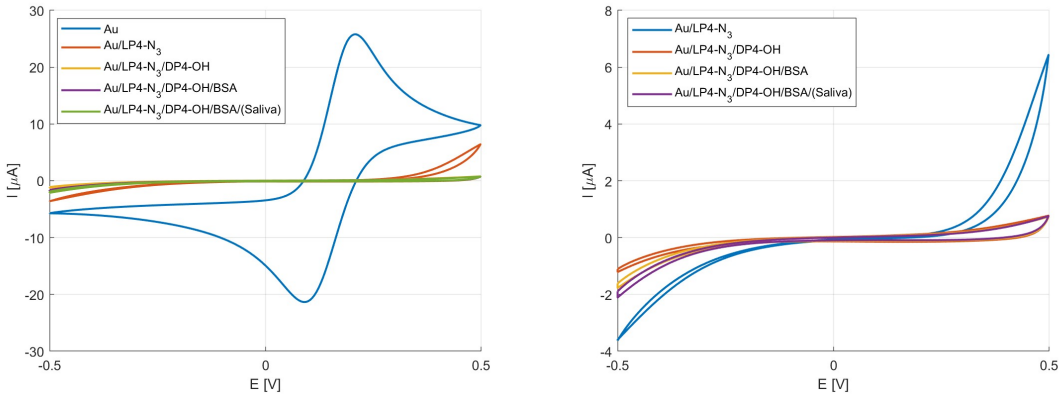

(a) **(b)**

Figure 4.10: Cyclic voltammograms of electrode 1 recorded at each step of the functionalization protocol. a) All incubation steps including the initial bare measurement. b) All steps except the bare measurement.

Table 4.3: Extracted peak potentials and peak currents for electrode 1 after each measurement. The percentage change in peak currents is calculated relative to the preceding step.

	$\mathbf{E}_{pa}$ [V]	$\mathbf{I}_{pa}$ [μA]	$\mathbf{E}_{pc}$ [V]	$\mathbf{I}_{pc}$ [μA]	$\mathbf{I}_{pa}$ **step** [%]	$\mathbf{I}_{pc}$ **step** [%]
Au	0.210	25.8	0.0930	-21.3	NaN	NaN
LP4-N$_3$	0.498	6.44	-0.500	-3.62	-75.0	-83.0
DP4-OH	0.498	0.773	-0.500	-1.22	-88.0	-66.5
BSA	0.498	0.735	-0.500	-1.78	-4.996	46.0
(Saliva)	0.498	0.761	-0.500	-2.11	3.60	18.9

A stepwise decrease in peak currents is observed throughout the functionalization sequence, indicating progressive surface blocking. The initial measurement displays the expected well defined redox peaks of the redox couple, characteristic of a clean and electrochemically accessible gold surface. After incubation with the linker solution, both anodic and cathodic peak currents decrease sharply, reflecting the formation of a surface bound linker layer that restricts electron transfer. The subsequent click-incubation produces an additional and substantial reduction in peak currents, consistent with the introduction of a second layer that further limits the accessibility of the redox couple to the electrode surface. The combined effect of linker and click molecule results in a markedly suppressed voltammetric response, consistent with progressive surface insulation.

Following BSA incubation, the anodic peak current remains essentially unchanged, while the cathodic peak becomes more negative. This behavior indicates that BSA adsorption does not significantly alter the already suppressed electron transfer rate imposed by the modification, but it modifies the interfacial environment in a way that slightly facilitates reduction. The increased magnitude of the cathodic peak

may reflect changes in local charge distribution or solvation that allow the redox couple to approach the surface more easily during the reduction step.

Exposure to equine saliva produces only minor changes in both peak currents, indicating that the surface is already strongly passivated by the full functionalization. Any additional nonspecific adsorption from saliva therefore has limited impact on electron transfer kinetics, consistent with the already highly insulated electrode surface.

All EIS measurements for electrode 1 are shown in Figure 4.11, and the corresponding fitted parameters are summarized in Table 4.4.

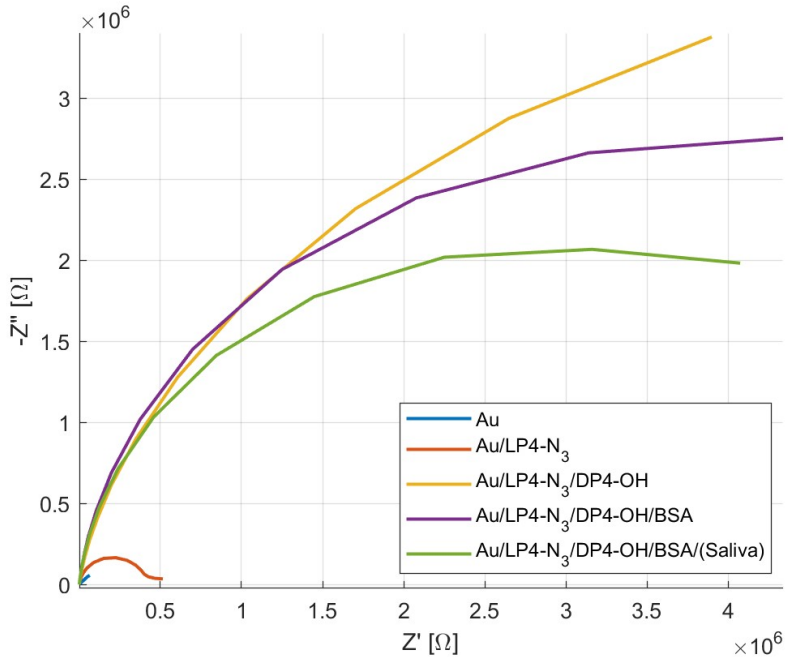

Figure 4.11: Nyquist plots of electrode 1 recorded at each step of the functionalization protocol.

Table 4.4: Fitted EIS parameters for electrode 1 after each measurement. The percentage change in R_{ct} is calculated relative to the preceding step.

	R_s [Ω]	R_{ct} [Ω]	Q [$\Omega^{-1}s^{\alpha}$]	α	σ [$\Omega\, s^{-1/2}$]	τ [s]	RMSE [Ω]	Rel. RMSE [%]	C_{eff} [F]	R_{ct} step [%]
Au	0.00485	9.69×10^4	1.36×10^{-5}	0.605	4.60×10^5	48.0	840	0.867	2.76×10^{-10}	NaN
LP4-N_3	254	4.13×10^5	3.11×10^{-7}	0.898	2.09×10^3	8.43×10^5	4.26×10^3	1.03	1.06×10^{-7}	326
DP4-OH	2.67×10^3	4.45×10^6	3.05×10^{-7}	0.886	3.55×10^6	3.69	3.79×10^4	0.852	1.22×10^{-7}	979
BSA	1.15×10^3	4.73×10^6	2.68×10^{-7}	0.913	1.85×10^6	2.96	3.80×10^4	0.802	1.24×10^{-7}	6.35
(Saliva)	3.15	2.74×10^6	2.74×10^{-7}	0.863	2.68×10^6	0.0129	5.03×10^4	1.83	2.99×10^{-8}	-42.1

The initial Au measurement displays the characteristic diffusion-dominated response of a clean gold electrode. After incubation with linker solution, the semicircle increases markedly, reflecting the formation of a surface bound linker layer that restricts access of the redox couple to the electrode and thereby slows electron transfer.

The subsequent click incubation produces a dramatic further increase in semicircle size, consistent with the formation of a densely packed DBCO-PEG layer that results in a substantially higher electron transfer barrier.

Following BSA incubation, the semicircle decreases slightly. This modest reduction suggests that BSA adsorption does not remove or disrupt the underlying modification but instead alters the interfacial environment in a way that slightly facilitates electron transfer relative to the highly blocked click-modified surface. Such an effect is consistent with minor changes in local charge distribution or solvation that allow the redox couple to approach the surface somewhat more easily.

Exposure to equine saliva results in a more pronounced decrease in semicircle size. As with BSA, this behavior likely reflects additional nonspecific adsorption that modifies the interfacial environment without removing the underlying functional layers. The reduced size in semicircle therefore indicates partial easing of the electron transfer barrier.

4.6.3 Control electrodes and nonspecific incubation effects

This section summarizes the electrochemical response of the control electrodes during the stepwise incubation sequence in terms of both CV and EIS behavior.

Bare control electrode
All CV measurements for the bare control electrode are shown in Figure 4.12, and the corresponding peak potentials and peak currents are summarized in Table 4.5.

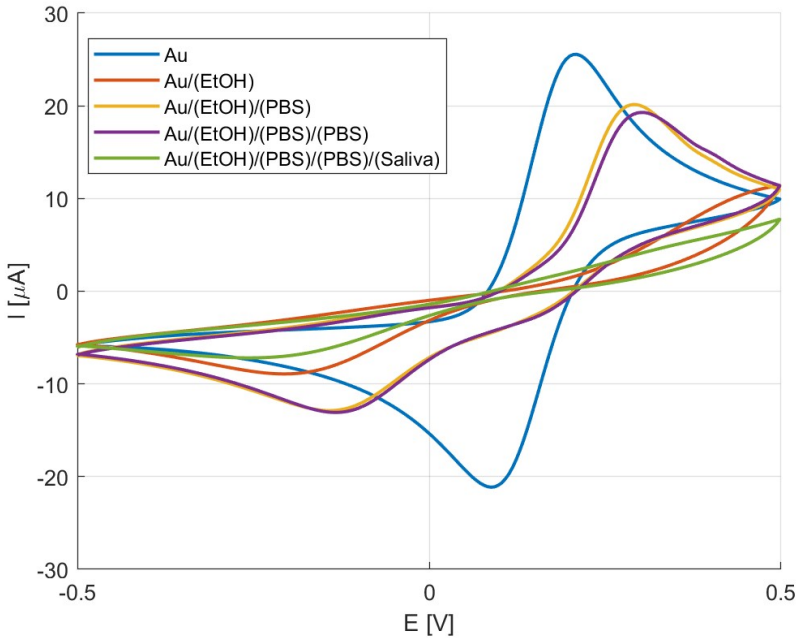

Figure 4.12: Cyclic voltammograms of the bare control electrode recorded at each step of the functionalization protocol.

Table 4.5: Extracted peak potentials and peak currents for the bare control electrode after each measurement. The percentage change in peak currents is calculated relative to the preceding step.

	$\mathbf{E}_{pa}$ [V]	$\mathbf{I}_{pa}$ [μA]	$\mathbf{E}_{pc}$ [V]	$\mathbf{I}_{pc}$ [μA]	$\mathbf{I}_{pa}$ step [%]	$\mathbf{I}_{pc}$ step [%]
Au	0.210	25.6	0.0879	-21.1	NaN	NaN
(EtOH)	0.498	11.4	-0.206	-8.92	-55.4	-57.8
(PBS)	0.291	20.1	-0.140	-12.9	76.6	44.4
(PBS)	0.301	19.3	-0.130	-13.1	-4.27	1.47
(Saliva)	0.498	7.78	-0.252	-7.19	-59.7	-45.0

The initial measurement on the untreated gold electrode displays the expected well defined redox peaks of the $Fe(CN)_6^{3-/4-}$ couple, with high peak currents and a steep voltammetric profile characteristic of an unmodified, electrochemically clean surface.

Incubation in ethanol results in a markedly flatter voltammogram with substantially reduced peak currents. This behaviour is consistent with partial surface blocking caused by adsorbed organic residues from ethanol, which hinder electron transfer between the redox couple and the electrode. Because the redox couple is highly sensitive to surface accessibility, even a thin adsorbed layer can significantly suppress the peak currents and broaden the voltammogram.

After rinsing and incubation in PBS, the voltammogram partially recovers toward its initial shape, with higher peak currents and steeper slopes compared to the ethanol treated state. This is expected, as PBS helps remove loosely bound organic residues and restores a more accessible electrode surface. However, the peaks remain slightly flatter than in the pristine state, indicating that some degree of surface contamination or restructuring persists.

The measurement performed after one hour of incubation in equine saliva, shows that the voltammogram again becomes flatter with further reduced peak currents. This behaviour is consistent with nonspecific adsorption of unknown biomolecules onto the gold surface. Such adsorption likely forms a partially blocking layer that hinders electron transfer between the redox couple and the electrode, leading to the observed decrease in both anodic and cathodic peak currents.

All EIS measurements for the bare control electrode are shown in Figure 4.13, and the corresponding fitted parameters are summarized in Table 4.6.

Table 4.6: Fitted EIS parameters for the bare control electrode after each measurement. The percentage change in R_{ct} is calculated relative to the preceding step.

	R_s [Ω]	R_{ct} [Ω]	Q [$\Omega^{-1}s^{\alpha}$]	α	σ [$\Omega\, s^{-1/2}$]	τ [s]	RMSE [Ω]	Rel. RMSE [%]	C_{eff} [F]	R_{ct} step [%]
Au	170	4.45×10^4	7.16×10^{-6}	0.761	3.34×10^5	29.6	1.33×10^3	2.99	8.67×10^{-7}	NaN
(EtOH)	0.0136	5.73×10^4	4.62×10^{-7}	0.785	7.26×10^4	21.2	2.20×10^3	3.84	2.62×10^{-9}	28.9
(PBS)	3.54×10^{-5}	4.44×10^4	4.70×10^{-6}	0.675	1.05×10^5	11.4	1.22×10^3	2.75	9.34×10^{-11}	-22.6
(PBS)	0.0137	3.60×10^4	2.53×10^{-6}	0.784	1.26×10^5	31.3	1.79×10^3	4.96	2.26×10^{-8}	-18.9
(Saliva)	420	1.54×10^5	1.12×10^{-6}	0.811	3.91×10^4	1.98	3.63×10^3	2.37	1.88×10^{-7}	326

The first EIS measurement performed on the cleaned gold surface shows a diffusion-

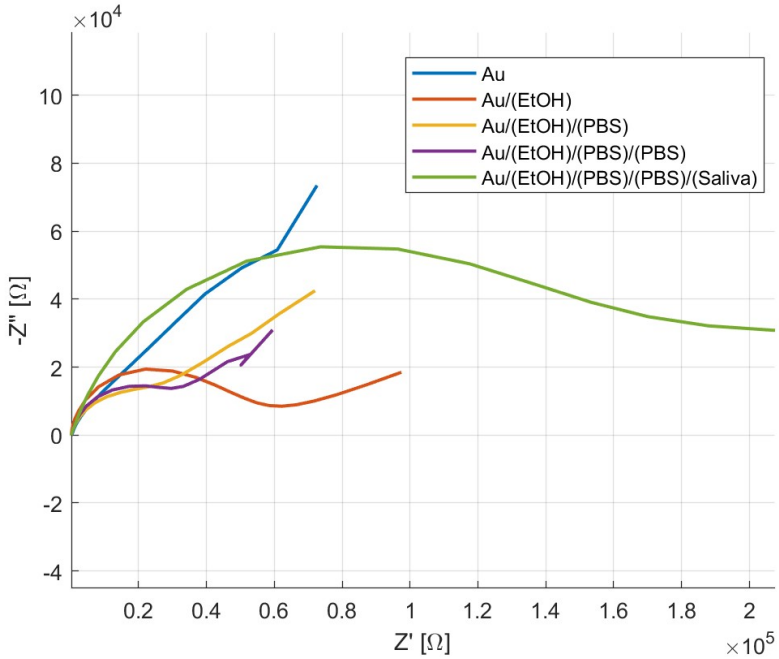

Figure 4.13: Nyquist plots of the bare control electrode recorded at each step of the functionalization protocol.

dominated response. After incubation in ethanol, the Nyquist plot shows a clearer and slightly enlarged semicircle compared to the untreated state, consistent with the presence of adsorbed organic residues left behind by ethanol. Such residues partially block the electrode surface and hinder electron transfer between the redox couple and the gold surface, in agreement with the reduced peak currents observed in the CV measurements.

Subsequent incubation in PBS restores the impedance response toward the initial state, with R_{ct} decreasing back to values close to the pristine electrode and moving towards more diffusion dominated graphs. This suggests that PBS removes loosely bound organic contaminants and re-exposes the electrode surface. However, the measurements after repeated PBS incubations do not fully return to the original state, which is consistent with the slightly flatter peaks observed in the CV measurements, indicating some degree of surface contamination or restructuring persists.

Following measurement performed after incubation in equine saliva show that the semicircle increases substantially, and R_{ct} rises by more than 300% compared to its previous step. This pronounced increase reflects nonspecific adsorption of biomolecules onto the gold surface, forming a blocking layer that impedes the electron transfer of the redox solution. The behavior aligns with the marked decrease in peak currents observed in the CV data and confirms that the bare electrode is highly susceptible to nonspecific adsorption in complex biological samples.

Linker control electrode

All CV measurements for the linker control electrode are shown in Figure 4.14, and the corresponding peak potentials and peak currents are summarized in Table 4.7.

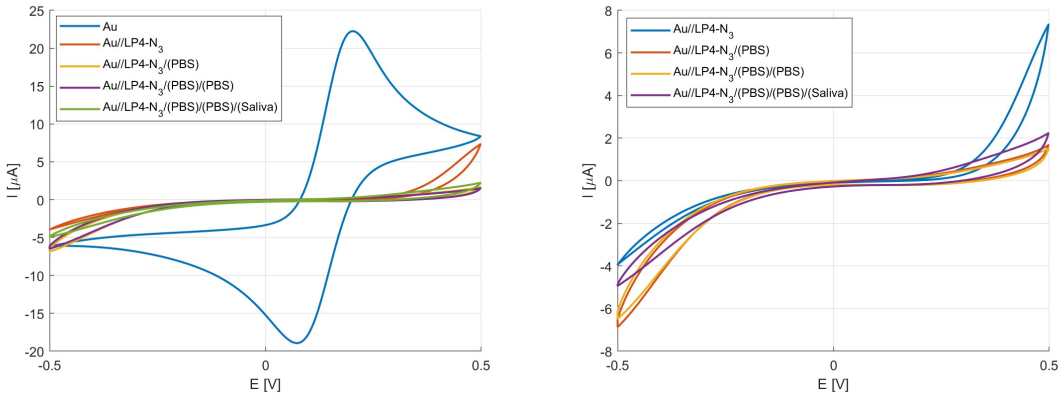

(a) **(b)**

Figure 4.14: Cyclic voltammograms of the linker control electrode recorded at each step of the functionalization protocol. a) All incubation steps including the initial bare measurement. b) All steps except the bare measurement.

Table 4.7: Extracted peak potentials and peak currents for the linker control electrode after each measurement. The percentage change in peak currents is calculated relative to the preceding step.

	$\mathbf{E}_{pa}$ **[V]**	$\mathbf{I}_{pa}$ **[μA]**	$\mathbf{E}_{pc}$ **[V]**	$\mathbf{I}_{pc}$ **[μA]**	$\mathbf{I}_{pa}$ **step [%]**	$\mathbf{I}_{pc}$ **step [%]**
Au	0.204	22.3	0.0727	-18.9	NaN	NaN
LP4-N_3	0.498	7.34	-0.500	-3.95	-67.0	-79.1
(PBS)	0.498	1.68	-0.500	-6.86	-77.2	73.5
(PBS)	0.498	1.51	-0.500	-6.48	-10.1	-5.59
(Saliva)	0.498	2.24	-0.500	-4.93	48.6	-23.9

The initial measurement on the untreated gold electrode displays the expected well defined redox peaks of the $Fe(CN)_6^{3-/4-}$ couple. After incubation with the linker solution, the voltammogram shows a substantial decrease in both anodic and cathodic peak currents, together with a noticeably flatter voltammetric profile. This behavior is consistent with the formation of a linker layer on the gold surface, which reduces the surface accessibility of the redox couple and thereby suppresses the peak currents.

The subsequent PBS incubations lead to only minor changes, with a slight decrease in the anodic peak current and an increase in the magnitude of the cathodic peak. The two PBS measurements overlap closely, indicating that the surface reaches a relatively stable state after the initial linker adsorption. The reduced anodic peak and more negative cathodic peak suggest that the linker layer remains intact and continues to hinder electron transfer, while PBS removes loosely bound linker molecules or solvent residues from ethanol without disrupting the underlying surface modification.

Following incubation in equine saliva, the cathodic peak current decreases again,

whereas the anodic peak shows a slight increase. This shift reflects additional non-specific adsorption of biomolecules onto the already linker-modified surface. Because the electrode is no longer bare, the effect is less pronounced than for the bare control electrode, but the changes still indicate that saliva components interact with and partially block the surface, influencing the electron transfer kinetics of the redox couple.

The corresponding EIS measurements for the linker control electrode are shown below. All EIS measurements for the linker control electrode are shown in Figure 4.15, and the corresponding fitted parameters are summarized in Table 4.8.

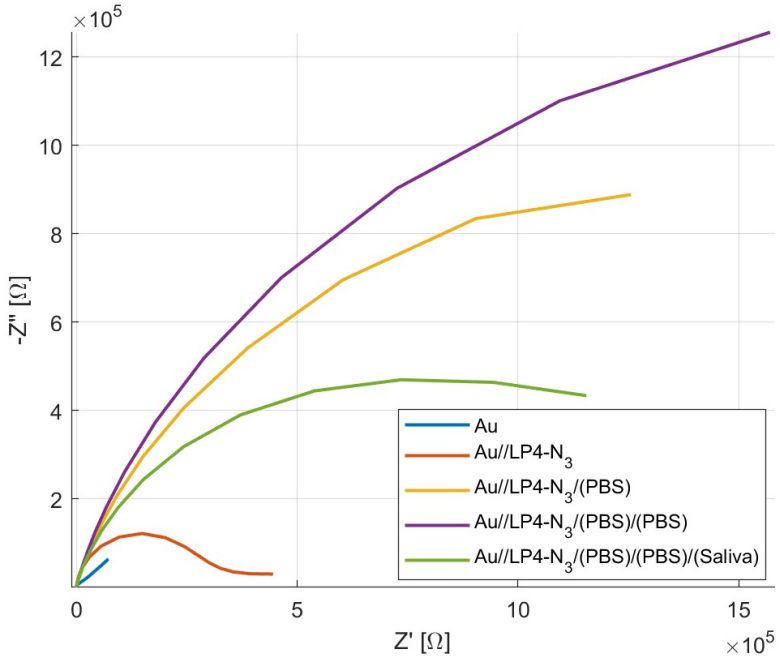

Figure 4.15: Nyquist plots of the linker control electrode recorded at each step of the functionalization protocol.

Table 4.8: Fitted EIS parameters for the linker control electrode after each measurement. The percentage change in R_{ct} is calculated relative to the preceding step.

	R_s [Ω]	R_{ct} [Ω]	Q [$\Omega^{-1}s^{\alpha}$]	α	σ [$\Omega\, s^{-1/2}$]	τ [s]	RMSE [Ω]	Rel. RMSE [%]	C_{eff} [F]	R_{ct} step [%]
Au	182	2.40×10^{4}	4.34×10^{-6}	0.801	4.34×10^{5}	67.0	257	1.07	7.33×10^{-7}	NaN
LP4-N_3	0.00688	3.21×10^{5}	3.43×10^{-7}	0.864	152	1.31×10^{6}	6.25×10^{3}	1.95	1.52×10^{-8}	1.24×10^{3}
(PBS)	1.84×10^{3}	1.20×10^{6}	8.88×10^{-7}	0.848	1.03×10^{6}	2.56	1.08×10^{4}	0.900	2.80×10^{-7}	273
(PBS)	3.13×10^{3}	1.64×10^{6}	7.12×10^{-7}	0.868	1.45×10^{6}	3.97	1.25×10^{4}	0.765	2.82×10^{-7}	36.8
(Saliva)	2.07×10^{3}	9.17×10^{5}	6.50×10^{-7}	0.847	4.67×10^{5}	2.53	1.75×10^{4}	1.91	1.97×10^{-7}	-44.0

After incubation with the linker solution, the semicircle increases dramatically, and R_{ct} rises by more than 1000%. This substantial increase reflects formation of a linker layer on the gold surface, which restricts access of the redox couple and thereby slows electron transfer kinetics. The magnitude of this increase is considerably larger than

for the bare control electrode, consistent with the linker being designed to bind strongly and form a more coherent blocking layer than residual ethanol only.

The two subsequent PBS incubations further modify the impedance response. The first PBS step produces the largest change in semicircle size, while the second results in a smaller additional increase. This behavior suggests that PBS primarily removes residual ethanol and other loosely bound species, revealing the intrinsic impedance of the linker-modified surface. The relatively lower apparent impedance observed immediately after ethanol exposure may therefore reflect transient interfacial effects from organic residues, which temporarily alter the electron transfer conditions at the surface.

Following incubation in equine saliva, the semicircle decreases noticeably, and R_{ct} drops over 40% relative to the final PBS step. This reduction likely reflects nonspecific adsorption of biomolecules from saliva, which modifies the interfacial environment and slightly alters the electron transfer conditions, leading to a lower resistance compared to the densely packed linker–PBS state.

4.6.4 Representative CV response during surface functionalization

Table 4.9 summarizes the relative changes in cathodic peak current for all electrodes and all functionalization steps. The values represent stepwise relative changes in cathodic peak currents extracted from cyclic voltammograms for all electrodes.

Table 4.9: Stepwise percentage change in I_{pc} at each functionalization step for all electrodes.

	Au [%]	**LP4-N_3** [%]	**DP4-OH** [%]	**BSA** [%]	**(Saliva)** [%]
CTRL bare	NaN	-57.8	44.4	1.47	-45.0
CTRL linker	NaN	-79.1	73.5	-5.59	-23.9
Electrode 1	NaN	-83.0	-66.5	46.0	18.9
Electrode 2	NaN	-90.7	-48.9	43.3	7.80
Electrode 3	NaN	-92.0	-22.8	23.9	25.8

A clear and consistent trend is observed across the dataset. During the linker step, all electrodes with added linker show a substantial decrease in I_{pc}, reflecting the formation of a surface bound layer that restricts electron transfer. The bare control electrode exhibits a smaller decrease than the other electrodes, which is consistent with its voltammogram. Its reduction peak appears at approximately –0.2V, whereas all other electrodes show a well defined peak at –0.5V. This shift in peak position indicates that the bare control electrode was not modified in the same way as the electrodes exposed to the linker solution.

At the click step, both control electrodes show an increase in I_{pc}, whereas all modified electrodes show a decrease. For the controls, this increase is likely caused by the removal of residual ethanol during the overnight PBS incubation, which reduces the

temporary interfacial effects introduced by ethanol and allows the redox couple to approach the surface more easily. In contrast, the decrease observed for the modified electrodes reflects further passivation due to formation of the triazole-PEG layer, which increases the electron transfer barrier.

During the BSA incubation step, both control electrodes show minimal changes in I_{pc} (+1% and –5.6%), consistent with stable voltammetric behavior after prior PBS treatment, as no BSA was added to these control electrodes during this step. In contrast, all modified electrodes show an increase in I_{pc} following BSA adsorption. This is consistent with BSA's net negative charge which may facilitate the approach of the positively charged redox species to the electrode surface during reduction.

A similar trend is observed after saliva incubation, where all fully modified electrodes show an increase in I_{pc}, while the control electrodes show a decrease. This confirms that saliva induces different interfacial effects depending on surface functionalization. On fully modified electrodes, the results suggest that the surface is already strongly passivated such that additional adsorption does not significantly increase blocking. Instead, the results indicate that charged species found in saliva may slightly enhance reduction by altering the interfacial charge environment. In contrast, on both control electrodes, the same adsorption appears to contribute to additional blocking through nonspecific interactions with the gold surface, resulting in a decrease in I_{pc}.

4.6.5 Representative EIS response during surface functionalization

Table 4.10 shows the relative changes in charge-transfer resistance for all electrodes across all functionalization steps.

Table 4.10: Stepwise percentage change in R_{ct} at each functionalization step for all electrodes.

	Au [%]	**LP4-N_3** [%]	**DP4-OH** [%]	**BSA** [%]	**(Saliva)** [%]
CTRL bare	NaN	28.9	-22.6	-18.9	326
CTRL linker	NaN	1.24×10^3	273	36.8	-44.0
Electrode 1	NaN	326	979	6.35	-42.1
Electrode 2	NaN	2.90×10^3	517	-10.1	-96.1
Electrode 3	NaN	117	202	5.10	-21.7

A clear increase is observed during the linker step for all modified electrodes, with at least a 100% increase compared to the bare state. In contrast, the bare control electrode shows only a modest increase (28.9%), which is most likely related to residual ethanol effects rather than true surface modification. The observed decrease in I_{pc} and increase in R_{ct} after ethanol exposure are both consistent with reduced electron transfer at the electrode interface. Although CV and EIS characterize different aspects of the electrochemical interface, the responses obtained by the two techniques indicate the same underlying mechanism.

Beyond the linker step, the R_{ct} values do not show a fully consistent trend across the electrodes. However, the Nyquist plots reveal clear and reproducible qualitative patterns. For the CTRL bare electrode, no substantial increase in impedance is observed except after saliva incubation, which is consistent with nonspecific adsorption from species in saliva likely being the main process affecting the unmodified surface. For the CTRL linker as well as the fully modified electrodes, the semicircle sizes follow a consistent order. The measurement after extended PBS exposure (corresponding to the BSA step in the modified electrodes) shows the largest semicircle for the CTRL linker, suggesting that extended PBS exposure gradually removes ethanol-related effects while the linker layer remains. The second largest semicircle is observed after the first PBS incubation (corresponding to the click chemsitry step). Oppositely, for all three fully modified electrodes, the largest semicircle is instead observed after the click chemistry step, reflecting the strong passivation introduced by the triazole-PEG layer and the second largest semicircle is observed after BSA incubation, consistent with the CV results indicating that interfacial charge effects facilitate redox species approach and slightly reduce the impedance.

4.6.6 Stepwise analysis of effective capacitance

While the CV peak currents and Nyqvist plots with extracted parameters showed clear trends throughout the functionalization process, the stepwise changes in fitted R_{ct} values were less consistent across all electrodes. To complement the R_{ct} analysis, the effective capacitance (C_{eff}) derived from the CPE element was examined as an additional interfacial parameter.

In several cases, C_{eff} displayed clearer and more reproducible stepwise trends than the fitted R_{ct} values, although no clear trend was observed during the linker adsorption step. Since C_{eff} is calculated from several fitted circuit parameters, according to equation 2.4, its interpretation should primarily be interpreted in terms of overall trends rather than as direct quantitative measures of interfacial properties. In general, decreases in C_{eff} can be interpreted as being consistent with a more insulating or less electrochemically accessible interfacial state, whereas increases in C_{eff} may indicate a more electrochemically accessible or less blocked interface. The absence of a clear trend during the linker adsorption step, together with the more pronounced changes observed in R_{ct}, suggests that the initial linker immobilization is primarily reflected in the charge-transfer resistance. In contrast, the clearer stepwise trends observed in C_{eff} during subsequent functionalization steps indicate that effective capacitance provides complementary information and may be more sensitive to smaller interfacial changes once the linker layer has been established.

Figure 4.16 shows C_{eff} before and after linker attachment for all electrodes, including the controls that were only exposed to ethanol during this step. No clear trend in C_{eff} was observed during the linker adsorption step. This contrasts with the pronounced changes previously observed in R_{ct}, suggesting that the initial linker immobilization is more clearly reflected in the charge-transfer resistance. Consequently, no consistent change in effective capacitance could be inferred from this step.

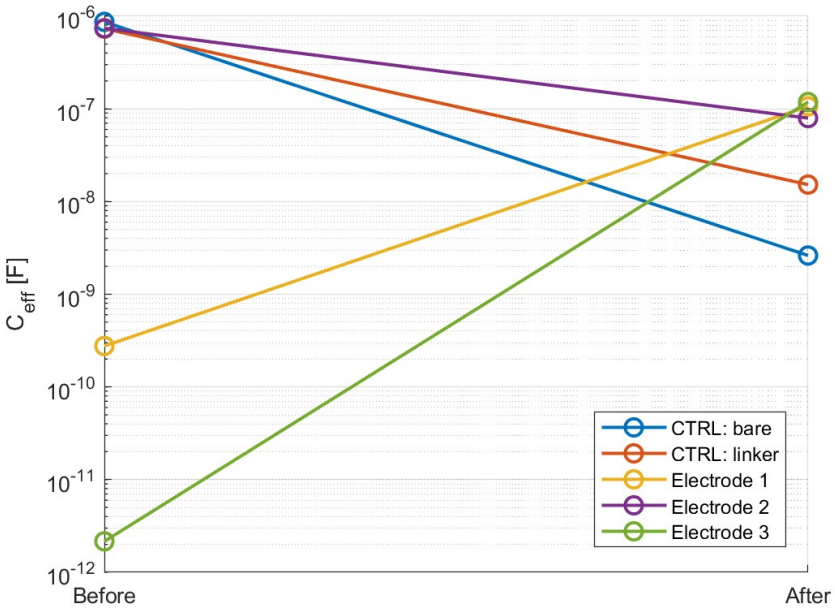

Figure 4.16: Effective capacitance for all electrodes before and after linker incubation with lipoamido-PEG4-azide, shown on a logarithmic scale.

Figure 4.17 shows C_{eff} before and after click chemistry incubation for all electrodes, including the controls that were only exposed to PBS during this step. The fully modified electrodes showed only a weak or negligible change in C_{eff} after the click chemistry incubation. In contrast, the control electrodes exhibited pronounced changes, with an increase in C_{eff} for the linker control and a decrease for the bare control.

For the fully modified electrodes, the weak change in C_{eff} suggests that multiple contributions to the interfacial response may counterbalance each other during the click chemistry step. In this system, the immobilization of additional molecular species, DBCO-PEG, may be offset by residual effects of the ethanol solvent used during linker incubation, resulting in a small net change in the effective capacitive response. In contrast, the linker control electrode, which lack the immobilization of DBCO-PEG, exhibit a more pronounced increase in C_{eff}. This suggests that solvent-related contributions from prior ethanol incubation may become more pronounced for this surface state during subsequent PBS exposure, leading to an apparent increase in the effective capacitance. The bare control electrode, which also were exposed to ethanol but lack both linker and DBCO-PEG modification, instead show a decrease in C_{eff}, consistent with a change in the interfacial state of the unmodified gold surface during PBS incubation. Redistribution of solvent-related contributions of the residual ethanol during PBS incubation may lead to a reduced effective capacitive response, without necessarily corresponding to a straightforward change in physical layer thickness.

Overall, the click chemistry step results in clearly distinguishable trends in C_{eff} for

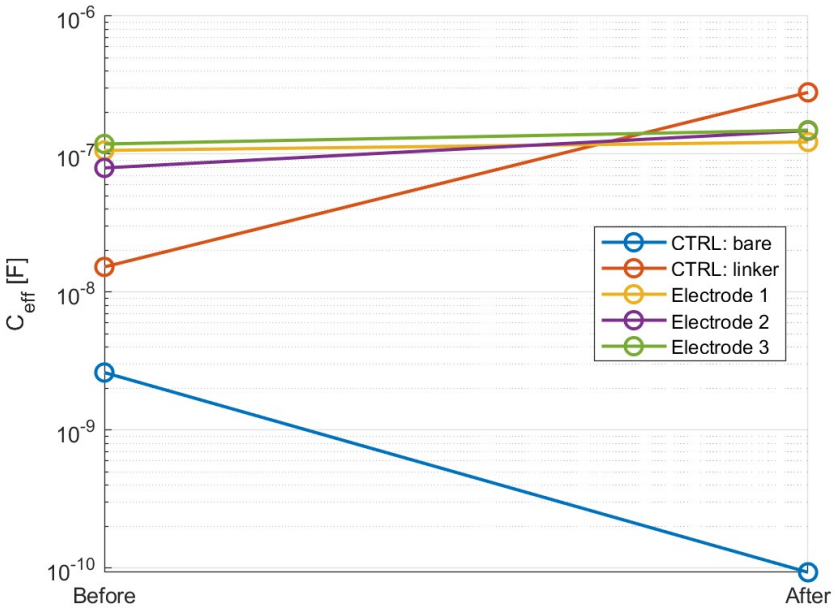

Figure 4.17: Effective capacitance for all electrodes before and after click reagent incubation with DBCO-PEG4-OH, shown on a logarithmic scale.

the different electrode types, with consistent behaviour observed within the fully modified group and distinct responses for the linker control as well as bare control electrode.

Figure 4.18 shows C_{eff} before and after BSA incubation for all electrodes, including the controls that were only exposed to PBS during this step. Overall, BSA incubation produces only minor changes in C_{eff} for the modified surfaces, while a clearer response is observed for the bare control electrode, highlighting differences in interfacial stability depending on the degree of surface functionalization. No noticeable change in C_{eff} was observed for the fully modified electrodes after BSA incubation. For the linker control, which was only exposed to PBS during this step, no corresponding change in C_{eff} was observed. This indicates that both surface types exhibited no pronounced alteration in the measured effective capacitance during this stage. In contrast, the bare control shows a clear increase in C_{eff} despite only being exposed to PBS. This suggests that the bare gold surface exhibits a more dynamic interfacial response, where repeated exposure to PBS may lead to measurable changes in the effective capacitance due to interactions occurring directly at the unmodified gold interface.

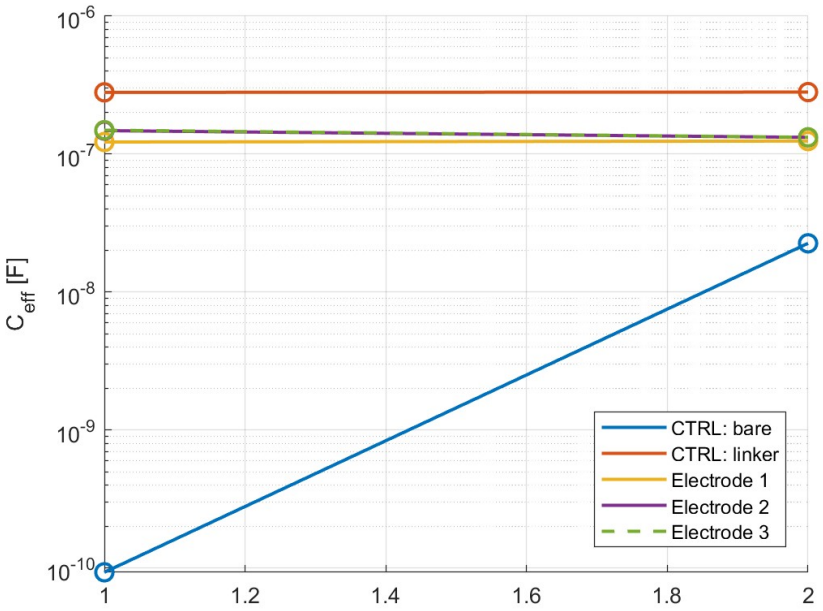

Figure 4.18: Effective capacitance for all electrodes before and after incubation with BSA, shown on a logarithmic scale.

Figure 4.19 shows C_{eff} before and after saliva incubation for all electrodes, including the controls. Both the fully modified electrodes and the linker control show a decrease in C_{eff} upon saliva incubation, consistent with adsorption of saliva components onto an already passivated surface, leading to a more insulating interfacial response and a reduction in the effective capacitance. In contrast, the bare control displays an increase in C_{eff}, suggesting that saliva components interact directly with the unmodified gold surface, resulting in a modified interfacial environment that increases the effective capacitance. Overall, this indicates that saliva primarily alters the interfacial properties of passivated electrodes in a manner consistent with increased interfacial blocking, whereas on bare gold it leads to the formation of a new interfacial layer with altered capacitive characteristics.

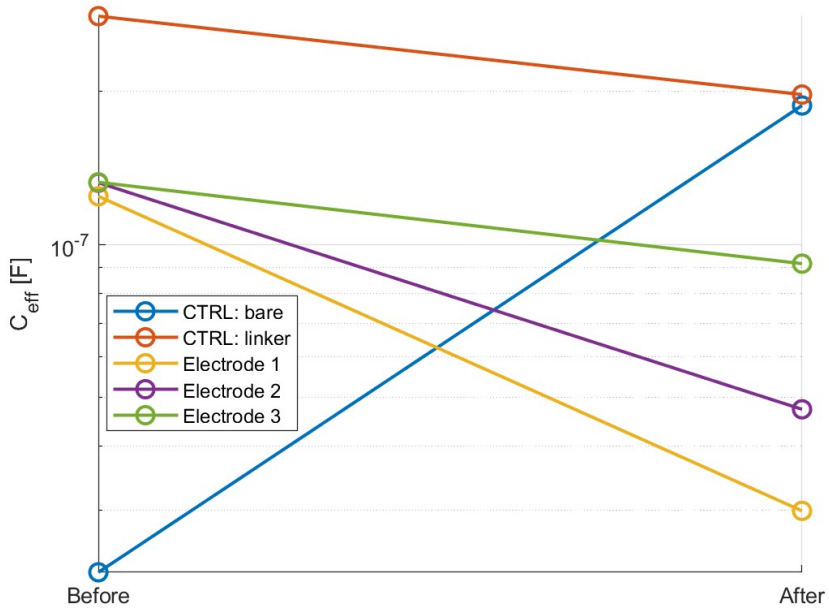

Figure 4.19: Effective capacitance for all electrodes before and after incubation with equine saliva, shown on a logarithmic scale.

4.6.7 EG-FET system CA response

Figure 4.20 shows the chronoamperometric measurements recorded on the CA electrode throughout the linker, click and BSA incubation steps during functionalization. It should be noted that the adhesive used in the Au-SPE was affected by ethanol exposure. This did not influence the electrodes embedded in PDMS used for CV and EIS measurements, where only the active area was exposed to ethanol. However, the CA electrode was fully immersed during the linker incubation step, and visible degradation of the adhesive was observed.

No clear changes in I_{DS} were observed during any of the functionalization steps. This was expected for the linker and click incubations, as the molecules used in these steps carry a net charge of zero and therefore would not generate a detectable electrostatic response in the transistor. The absence of a signal during BSA incubation can be explained by the combination of a highly passivating DBCO-PEG layer, which limits nonspecific adsorption and reduces the availability of binding sites, as well as the high ionic strength of PBS, which shortens the effective Debye length and further reduces electrostatic sensitivity. Under these conditions, the EG-FET system has limited ability to detect changes in gate potential, as the high ionic strength of PBS strongly screens any charge and the passivating PEG layer greatly reduces the likelihood of BSA binding events.

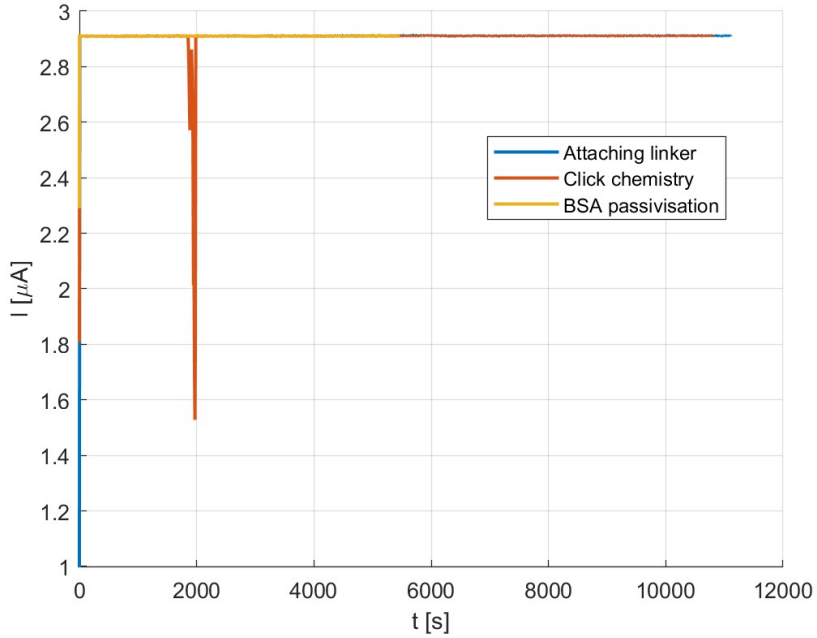

Figure 4.20: CA measurements with EG-FET system during functionalization steps of Au-SPE. "Linker attachment" corresponds to binding of lipoamido-PEG4-azide, "click chemistry" corresponds to binding of DBCO-PEG4-OH and "BSA passivation" corresponds to adsorption of BSA. At approximately 2000 s during the click step, the electrode briefly slipped out of the cuvette and was repositioned.

4.6.8 Summary of functionalization results

Overall, the CA measurements showed no electrochemical response during functionalization, which is consistent with the use of uncharged molecules (linker and click reagent) under high ionic strength conditions, thereby reducing sensitivity to interfacial changes. In contrast, the combined CV and EIS results consistently demonstrated successful stepwise surface functionalization, where linker immobilization and click chemistry produced the strongest electrochemical passivation, while the control electrodes primarily reflected nonspecific interfacial effects.

The electrochemical trends observed for electrode 1 were reproduced across the remaining fully modified electrodes (electrode 2 and electrode 3 can be seen in Appendix F), although the magnitude of the responses varied somewhat between electrodes. For all fully modified electrodes, linker incubation resulted in a clear suppression of the electrochemical response compared to bare gold, while the subsequent click reaction produced additional passivation. The effects observed after BSA and saliva incubation were smaller and less consistent in magnitude, but similar overall trends were still visible across the electrodes. These trends were distinct from those observed for the two control electrodes.

Taken together, the reproducible electrochemical behavior observed across six independently functionalized electrodes, together with comparison against four different controls, demonstrates that the surface modification procedure was both successful

and reproducible.

4.7 Supplementary EG-FET CA Experiments

The experiments described in Section 3.4.6 are presented below. Figure 4.21 shows the chronoamperometric response of BSA on bare gold electrodes under the different conditions.

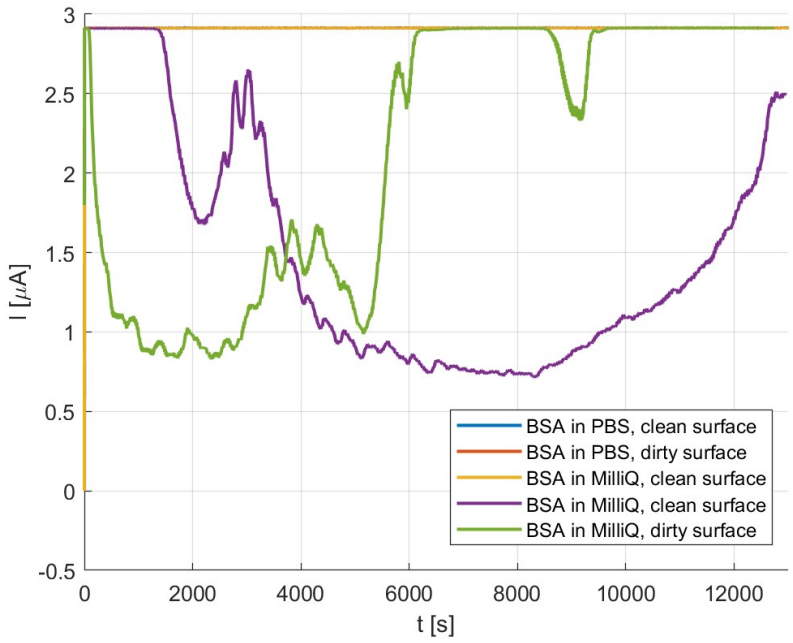

Figure 4.21: Chronoamperometric measurements of BSA binding on Au-SPEs under different conditions, comparing cleaned and uncleaned surfaces and BSA dissolved in either PBS or MilliQ.

In both cases where BSA binding is seen, I_{DS} decreases upon BSA adsorption. This is consistent with BSA carrying a net negative charge at pH above 4.7 and thereby partially closing the channel of the N-type transistor in the EG-FET system.

The binding occurs more rapidly on uncleaned electrodes than on cleaned ones, suggesting that BSA adsorbs more readily onto a rougher or more heterogeneous surface. This behavior may be related to the fact that increased surface roughness generally provides a larger effective surface area and more available binding sites. Furthermore, hydrophobic surface regions may promote protein adsorption more readily than hydrophilic ones. This may also explain why BSA dissolved in MilliQ water only produced a clear response on the cleaned electrode in one of the repetitions, as small differences in surface roughness in that case could influence the adsorption kinetics. Overall, the results indicate that BSA binds faster to less uniform surfaces and that its net negative charge under given measurement conditions narrow the transistor channel, resulting in a decrease in I_{DS}.

Figure 4.22 shows the chronoamperometric response of the synthetic biomarkers $COMP^{156}$ and BGN^{262} on cleaned gold electrodes under different solvent conditions. Note that these measurements were performed on bare gold electrodes without Fab' functionalization and therefor the observed responses are attributed to nonspecific adsorption and likely arise from different interaction mechanisms than those involved in antibody-biomarker recognition.

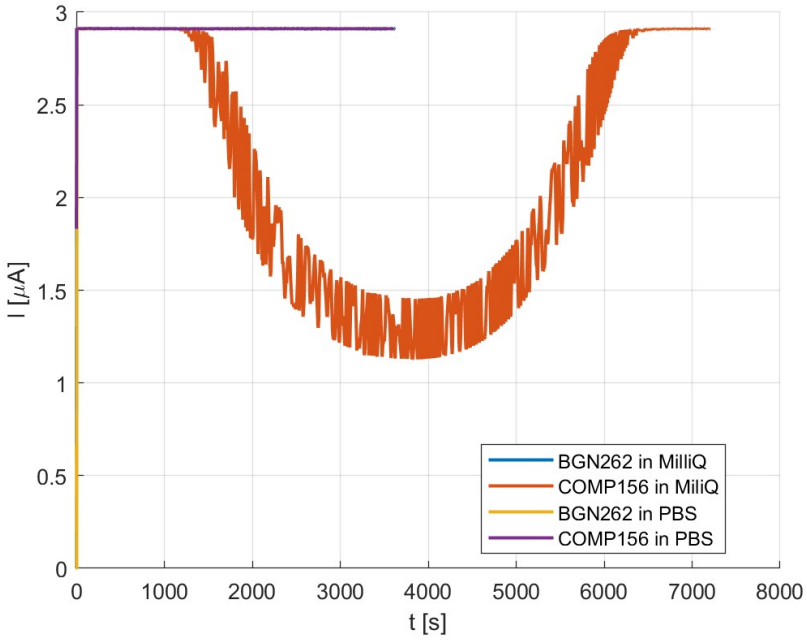

Figure 4.22: Chronoamperometric measurements on cleaned Au-SPEs showing adsorption of the synthetic biomarkers $COMP^{156}$ and BGN^{262} under different solvent conditions, comparing PBS and MilliQ.

A clear binding response was observed for $COMP^{156}$ when dissolved in MilliQ, which produced a rapid decrease in I_{DS} similar to the behavior seen for BSA. This suggests that $COMP^{156}$ carries a net negative charge under the measurement conditions, leading to partial channel closure of the N-type transistor in the EG-FET system. No clear binding response was detected for BGN^{262}. However, these tests do not necessarily reflect the behavior of the native biomarkers in saliva, as the synthetic peptides may differ in length or fragmentation state compared to the physiological fragments, which could influence their net charge and adsorption behavior.

The most important observation from both the BSA and biomarker CA experiments is that measurable responses were only obtained when the analytes were dissolved in MilliQ. This highlights the strong dependence of the EG-FET response on ionic strength and suggests that low salt conditions are required for detectable surface charge modulation in order to remain within the effective Debye length of the system.

For both BSA and $COMP^{156}$, I_{DS} decreased rapidly upon initial binding and then gradually approached a more stable level before slowly increasing again, a pattern

consistent with fast initial adsorption followed by slower surface rearrangement and progressive blocking of the electrode surface. This behavior is particularly clear for $COMP^{156}$ in MilliQ, where I_{DS} exhibits a distinct U-shaped profile: a sharp initial decrease, a well defined minimum and a gradual return toward equilibrium and the starting value. Such a curve is characteristic of rapid early adsorption, followed by a slower reorganization phase in which the adsorbed layer becomes more compact and, as the adsorption slows, the rate of further surface charge modulation decreases, allowing I_{DS} to gradually return toward its initial value. BSA shows the same overall trend, although the curve is less smooth and contains more fluctuations. This may indicate differences in the structure of the adsorbed layers, where BSA may form a more heterogeneous or multilayer-like assembly, while $COMP^{156}$ may be more likely to form a more uniform and compact surface layer.

The higher level of fluctuations observed for $COMP^{156}$ compared to BSA under identical measurement conditions may be related to differences in adsorption dynamics and molecular flexibility of the two, indicating that these factors result in a more sensitive response to adsorption events for $COMP^{156}$, leading to larger variations in surface charge and increased fluctuations in I_{DS}.

Overall, both analytes display the same fundamental kinetic signature of fast initial adsorption followed by slower surface blocking and a recovery of the channel current toward its initial state.

5

Discussion

This discussion relates the experimental results to the overall aim of the project and evaluates the performance, limitations and future potential of the developed biosensor platform.

A central part of the project aim was to develop the initial components of an electrochemical biosensing platform suitable for detecting OA-related biomarkers in equine saliva. The results demonstrate that these foundational components have been successfully established. The measurement setup, surface chemistry and electrode architecture all function as intended, providing a stable basis for further development. However, further advancements are required to ensure that future measurements fall within the effective Debye length of the system. This will be essential for enabling selective detection of $COMP^{156}$ and BGN^{262} in equine saliva, as discussed further in Section 5.1.

The EG-FET measurement setup established consisted of an EmStat Pico development board, an N-type JFET transistor as well as low cost disposable Au-SPEs. The modular design of the system, including the use of interchangeable SPEs, enabled flexible testing and ensured that each measurement could be performed on precisely the type of modified electrode required for each experiment. The setup demonstrated stable operation and good reproducibility when performing CA measurements, where identical settings consistently produced the same initial current prior to the onset of surface binding. These measurements also confirmed that the system is capable of detecting changes in gate potential when binding events of molecules carrying a net negative charge occur sufficiently close to the electrode surface, under conditions of low ionic strength where the effective Debye length is comparatively large. Together, these results indicate that the EG-FET platform operates reliably and provides a solid foundation for further optimization.

The copper free click based surface functionalization was successfully implemented. Demonstrated by consistent results performed in triplicate using both EIS and CV. These techniques confirmed that each functionalization step proceeded as intended, resulting in a stable and reproducible modification of the gold electrode surface. In contrast, the CA measurements did not show any detectable signal changes during the linker or click incubations, which is consistent with the fact that both molecules carry a net charge of zero and therefore do not introduce a strong electrostatic effect detectable by the EG-FET. The absence of a CA response during BSA incubation

on modified electrodes can likewise be explained by the combination of a highly passivating PEG layer, which limits nonspecific adsorption and reduces the number of available binding sites, and the high ionic strength of PBS, which shortens the effective Debye length and makes it difficult for the EG-FET system to detect any changes in gate potential. Together, these results confirm that the click-based functionalization strategy is robust and compatible with the EG-FET platform, while also highlighting the importance of Debye length considerations for future sensing applications.

Although Fab' fragments were not included in the experimental work of this project, the surface chemistry developed here is compatible with their future integration. The DBCO-PEG molecules used during functionalization bind to the azide terminated linker through copper free click chemistry and DBCO-conjugated Fab' fragments would react through the same mechanism. The successful implementation of this chemistry therefore provides a proof-of-concept foundation for incorporating DBCO coupled Fab' fragments as recognition elements in later stages of this sensor development.

While the sensor is not yet fully developed, the results of this project indicate that the platform has strong potential for future adaptation to ex vivo measurements in field settings such as stable environments. The overall successful results suggest that the system could be further optimized for direct analysis of equine saliva samples outside the laboratory. Since the targeted biomarkers are the same across mammals, the underlying sensing principle could be adapted for other species as well, including humans. In the longer term, the system could be advanced toward potential in vivo applications for continuous monitoring in the oral cavity. Such development will, however, require biocompatibility evaluation and alignment with corresponding ISO standards.

5.1 Future Work

Based on the experimental findings and the practical limitations observed throughout the project, several recommendations for future development are proposed. These suggestions represent one possible path forward, while acknowledging that alternative approaches may also be viable.

5.1.1 Verifying charge detection at Fab'-relevant distances

A central question for future development is whether the EG-FET system will be able to detect the charge redistribution associated with OA–biomarker binding events to its Fab' fragments. Since both $COMP^{156}$ and BGN^{262} may exhibit a net charge close to zero under physiological conditions, eventhough the synthetic peptide for $COMP^{156}$ has shown an indication for having a net charge below zero under CA measurements performed in this project, the resulting change in gate potential may be too small to register. This must therefore be evaluated experimentally.

A suitable first step is to verify that the transistor can detect charge-related bind-

ing events occurring at the distances relevant for Fab'-based sensing, approximately 6 nm according to Section 1.3. This can be evaluated by creating a controlled model system in which a charged DBCO-functionalized molecule is clicked onto azide-terminated PEG chains of different lengths on the lipoamido-PEGn-azide linker. By keeping the introduced charge constant and varying only the PEG length of the linker, it becomes possible to determine whether the system is able to detect binding events up to that length. These experiments should first be performed in MilliQ, where the Debye length is sufficiently long to increase the likelihood that any charge induced potential shift remains detectable. If no signal can be detected even under these favorable conditions, the choice of transistor architecture should be reconsidered. In particular, an OECT-based design may offer the higher sensitivity required to resolve binding events at these distances. OECTs typically provide improved sensitivity to small potential changes at the gate interface compared to regular FETs. A future design could therefore employ a reusable OECT channel on a small chip in combination with a separate, replaceable gold gate electrode. By electrically connecting the gate to the OECT through a simple lead, the setup would retain the same modular extended gate design used in this project while benefiting from the enhanced signal amplification characteristic of OECTs. In such a configuration, only the gate electrode would be exposed to the sample solution, whereas the OECT channel would remain encapsulated and protected from nonspecific interactions with saliva. This would allow the gate surface to be exchanged between measurements in the same manner as in the current EG-FET platform, while keeping the transistor element stable, reusable, and shielded from biofouling.

5.1.2 Testing Fab'-based biomarker recognition and increasing ionic strength

Once a configuration is identified that reliably detects binding events occuring in the order of 6 nm in MilliQ, the next step is to functionalize the surface with the intended linker chemistry and DBCO-Fab' fragments found in Section 1.3. Synthetic biomarkers dissolved in MilliQ can then be introduced to evaluate whether Fab'–biomarker binding events produce a measurable response. If a signal is observed, the ionic strength can gradually be increased using synthetic saliva to determine the maximum ionic strength at which the system remains sensitive, and to establish the minimum dilution required for saliva samples to be measurable. If no signal is observed, particularly expected for BGN^{262} as suggested by the CA results in this work (under the assumption that specific Fab'-biomarker interactions induce comparable charge effects as those obtained from nonspecific adsorption), alternative strategies should be explored. These include introducing a defined charge on the recognition element such as DBCO-conjugated Fab' fragments with an engineered net charge. In such a design, biomarker binding would neutralize or shield this charge, thereby generating a measurable change in gate potential even if the biomarker itself is uncharged. Any charge-modified Fab' fragment should be validated with ELISA to ensure that antigen binding is not impaired. Once a functional configuration is identified, the same systematic evaluation of ionic strength and sample dilution should be performed before transitioning to real saliva samples.

5.1.3 Optimizing surface chemistry, EG-FET signal response and calibration

After a suitable transistor architecture has been identified, a detectable signal has been confirmed for both biomarkers and the usable ionic strength range as well as required dilution of saliva have been established, several aspects of the sensing platform can be systematically optimized to further improve performance. Many of these parameters are interdependent, making a design of experiments (DoE) approach particularly valuable. Key factors include the ratio between DBCO-PEG and Fab', the length of the passivating PEG layer, and the overall surface density of functional groups. Proper optimization of PEG passivation is required to ensure sufficient blocking of nonspecific binding while avoiding steric hindrance of biomarker access to the Fab' recognition sites, thereby tuning the balance between specific and nonspecific binding which in turn influences the detectable signal of the sensor.

It should also be investigated whether functionalizing only WE or both WE and CE of the electrode provides the most sensitive system. The applied bias conditions during CA measurements should also be optimized to ensure that $S_{\max}$ is not reached within the low-concentration regime of each biomarker, allowing detection across the full range of observed concentrations while maintaining sufficient sensitivity to achieve a LoD below the healthy concentration thresholds. Temperature is another critical parameter which could have a significant impact on the rate of the binding events as well as the Debye length. This is especially relevant for potential in vivo applications, as the normal temperature of horses vary between individuals, but also for ex vivo applications used in field settings such as stables where the temperature can vary greatly depending on the current outside temperature. Future studies should therefore investigate how the sensor response varies across a wide temperature range, and whether temperature compensation or integrated thermal monitoring would be required for accurate measurements both in and outside the oral cavity.

Further optimization could also involve the laboratory protocol itself, incubation times, washing steps, and temperatures can all be optimized using DoE to reduce total functionalizaition time without compromising surface quality. To enable quantitative measurements, the sensor will eventually require calibration curves that link the electrical response of the transistor to known biomarker concentrations. Preferably, the same sample should be used under varied conditions such as different temperatures and have a known pH to generate a range of calibration curves for the same sample under each condition. These standard curves should be generated by measuring the EG-FET signal for samples with ELISA verified concentrations of each biomarker, ideally using a triplicate of electrodes for every concentration curve under each condition. In future tests, real samples will be measured using the EG-FET system under controlled pH and temperature conditions. The measured response will then be matched to calibration curves generated under matching conditions in order to determine the corresponding biomarker concentration.

5.1.4 Improving electrode design and multichannel measurements

Finally, the physical design of the electrode and measurement system offers additional opportunities for improvement. Printing electrodes on glass substrates instead of PET would enable oxygen-plasma cleaning as a rapid and reproducible surface-preparation step, replacing the electrochemical cleaning used in this project and thereby simplifying fabrication while increasing throughput. At the system level, a multi-channel measurement board with three parallel transistor channels would allow simultaneous reference measurements and dual biomarker detection from a single saliva droplet. One electrode would be functionalized only with PEG (reference), one with PEG + Fab' for $COMP^{156}$ and one with PEG + Fab' for BGN^{262}. This configuration would enable on site calibration according to Equation 1.2, which is essential given the variability in ionic strength between horses and sampling occasions. Together, these improvements would support the development of a robust, field deployable sensing platform suitable for practical use in stable environments.

6

Conclusion

This work presented the preliminary development of a transistor-based biosensing platform aimed at detecting OA related biomarkers in equine saliva. An EG-FET design was established, combined with a copper free click chemistry functionalization strategy on Au-SPEs as the extended gate electrode. CV and EIS confirmed that each functionalization step produced clear and reproducible electrochemical signatures, demonstrating that the surface chemistry was robust and reliably implemented on the electrodes. CA measurements using a custom EG-FET set up demonstrated that the system successfully detected surface-bound charge variations, validating the basic sensing principle of the platform. However, the results obtained by the EG-FET also revealed fundamental limitations imposed by Debye screening, indicating that further development is required before reliable biomarker detection can be achieved. Overall, the platform developed in this project represents a promising first step toward a transistor-based biosensor for detection of OA-related biomarkers in equine saliva, although substantial development remains before a fully functional diagnostic device can be realized.

Bibliography

[1] K. Nganvongpanit, R. Soponteerakul, P. Kaewkumpai, V. Punyapornwithaya, K. Buddhachat, R. Nomsiri, P. Kaewmong, K. Kittiwatanawong, R. Chawangwongsanukun, T. Angkawanish, C. Thitaram, and P. Mahakkanukrauh, "*Osteoarthritis in two marine mammals and 22 land mammals: learning from skeletal remains*," *Journal of Anatomy*, vol. 231, no. 1, pp. 140–155, 2017. doi: 10.1111/joa.12620.

[2] C. W. McIlwraith, C. E. Kawcak, D. D. Frisbie, C. B. Little, P. D. Clegg, M. J. Peffers, M. A. Karsdal, S. Ekman, S. Laverty, R. A. Slayden, L. J. Sandell, L. S. Lohmander, and V. B. Kraus, "*Biomarkers for equine joint injury and osteoarthritis*," *Journal of Orthopaedic Research*, vol. 36, no. 3, pp. 823–831, 2018. doi: 10.1002/jor.23738.

[3] S. Ekman, A. Lindahl, U. Rüetschi, A. Jansson, K. Björkman, K. Abrahamsson-Aurell, S. Björnsdóttir, M. Löfgren, L. Mattsson Hultén, and E. Skiöldebrand, "*Effect of circadian rhythm, age, training and acute lameness on serum concentrations of cartilage oligomeric matrix protein (COMP) neo-epitope in horses*," *Equine Veterinary Journal*, vol. 51, no. 5, pp. 674–680, 2019. doi: 10.1111/evj.13082.

[4] S. Adepu, M. Lord, Z. Hugoh, S. Nyström, L. Mattsson-Hulten, K. Abrahamsson-Aurell, C. Lützelschwab, and E. Skiöldebrand, "*Salivary biglycan-neo-epitope-BGN262: A novel surrogate biomarker for equine osteoarthritic sub-chondral bone sclerosis and to monitor the effect of short-term training and surface arena*," *Osteoarthritis and Cartilage Open*, vol. 5, no. 2, p. 100354, 2023. doi: 10.1016/j.ocarto.2023.100354.

[5] E. Skiöldebrand, S. Ekman, L. Mattsson Hultén, E. Svala, K. Björkman, A. Lindahl, A. Lundqvist, P. Önnerfjord, C. Sihlbom, and U. Rüetschi, "*Cartilage oligomeric matrix protein neoepitope in the synovial fluid of horses with acute lameness: A new biomarker for the early stages of osteoarthritis*," *Equine Veterinary Journal*, 2017. doi: 10.1111/evj.12666.

[6] GBD 2021 Osteoarthritis Collaborators, "*Global, regional, and national burden of osteoarthritis, 1990–2020 and projections to 2050: a systematic analysis for the Global Burden of Disease Study 2021*," *The Lancet Rheumatology*, vol. 5, no. 9, pp. e508–e522, 2023. doi: 10.1016/S2665-9913(23)00163-7.

[7] X. Jin, W. Liang, L. Zhang, S. Cao, L. Yang, and F. Xie, "*Economic and Humanistic Burden of Osteoarthritis: An Updated Systematic Review of Large Sample Studies*," *PharmacoEconomics*, vol. 41, pp. 1453–1467, 2023. doi: 10.1007/s40273-023-01296-1.

[8] R. L. Meeson, R. J. Todhunter, G. Blunn, G. Nuki, and A. A. Pitsillides, "*Spontaneous dog osteoarthritis - a One Medicine vision*," *Nature Reviews. Rheumatology*, vol. 15, no. 5, pp. 273–287, 2019. doi: 10.1038/s41584-019-0202-1.

[9] S. Adepu, S. Ekman, J. Leth, U. Johansson, A. Lindahl, and E. Skiöldebrand, "*Biglycan neo-epitope (BGN262), a novel biomarker for screening early changes in equine osteoarthritic subchondral bone*," *Osteoarthritis and Cartilage*, vol. 30, no. 10, pp. 1328–1336, 2022. doi: 10.1016/j.joca.2022.07.005.

[10] S. Kundu, B. G. Ashinsky, M. Bouhrara, E. B. Dam, S. Demehri, M. Shifat-E-Rabbi, R. G. Spencer, K. L. Urish, and G. K. Rohde, "*Enabling early detection of osteoarthritis from presymptomatic cartilage texture maps via transport-based learning*," *Proceedings of the National Academy of Sciences*, vol. 117, no. 40, pp. 24709–24719, 2020. doi: 10.1073/pnas.1917405117.

[11] K. Strimbu and J. A. Tavel, "*What are Biomarkers?*," *Current Opinion in HIV and AIDS*, vol. 5, no. 6, pp. 463–466, 2010. doi: https://doi.org/10.1097/COH.0b013e32833ed177.

[12] T.-w. Ma, Y. Li, G.-y. Wang, X.-r. Li, R.-l. Jiang, X.-p. Song, Z.-h. Zhang, H. Bai, X. Li, and L. Gao, "*Changes in Synovial Fluid Biomarkers after Experimental Equine Osteoarthritis*," *Journal of Veterinary Research*, vol. 61, no. 4, pp. 503–508, 2017. doi: 10.1515/jvetres-2017-0056.

[13] E. Skiöldebrand, S. Adepu, C. Lützelschwab, S. Nyström, A. Lindahl, K. Abrahamsson-Aurell, and E. Hansson, "*A randomized, triple-blinded controlled clinical study with a novel disease-modifying drug combination in equine lameness-associated osteoarthritis*," *Osteoarthritis and Cartilage Open*, vol. 5, no. 3, p. 100381, 2023. doi: 10.1016/j.ocarto.2023.100381.

[14] Arthro Diagnostics. `https://arthrodiagnostics.se/`. GoCo House, CCRM Nordics, 431 53 Mölndal, Sweden.

[15] V. Kraus and M. Karsdal, "*Clinical monitoring in osteoarthritis: Biomarkers*," *Osteoarthritis and Cartilage*, vol. 30, no. 9, pp. 1159–1173, 2022. Open Archive.

[16] O. Gutiérrez-Sanz, N. Haustein, M. Schroeter, T. Oelschlaegel, M. S. Filipiak, and A. Tarasov, "*Transistor-based immunosensing in human serum samples without on-site calibration*," *Sensors and Actuators B: Chemical*, vol. 295, pp. 153–158, 2019. doi: 10.1016/j.snb.2019.05.043.

[17] Y. Fujii, L. Liu, L. Yagasaki, M. Inotsume, T. Chiba, and H. Asahara, "*Cartilage Homeostasis and Osteoarthritis*," *International Journal of Molecular Sciences*, vol. 23, no. 11, p. 6316, 2022. doi: 10.3390/ijms23116316.

[18] B. N. Brown and S. F. Badylak, "*Extracellular matrix as an inductive scaffold for functional tissue reconstruction*," *Translational Research*, vol. 163, no. 4, pp. 268–285, 2014. doi: 10.1016/j.trsl.2013.11.003.

[19] "*Antibody Basics Guide*." `https://docs.abcam.com/pdf/antibody-guide/antibody-basics-guide.pdf`, 2023. Abcam, accessed 2026-05-11.

[20] K. Murphy and C. Weaver, *Janeway's Immunobiology*. Garland Science, 9 ed., 2017. Section 4-2: Immunoglobulin heavy and light chains are composed of constant and variable regions.

[21] M. Giese, "Personal communication." Vector Laboratories, Feb. 2026.

[22] ScienceInsights, "*What Is Kd in Enzyme Kinetics and Why Does It Matter?*," 2026. Accessed on 2026-05-25: scienceinsights.org.

[23] F. C. Howarth, J. Singh, J. J. Waring, B. I. Hustler, and M. Bailey, "*Effects of monovalent cations, pH and temperature on the dissociation constant (KD) for the fluorescent indicator mag-fura-2 at different excitation wavelengths*," *Magnesium Research*, vol. 8, no. 4, pp. 299–306, 1995. pubmed.ncbi.nlm.nih.gov.

[24] X. Shi, L. Kuai, D. Xu, Y. Qiao, Y. Chen, B. Di, and P. Xu, "*Surface Plasmon Resonance (SPR) for the Binding Kinetics Analysis of Synthetic Cannabinoids: Advancing CB1 Receptor Interaction Studies*," *International Journal of Molecular Sciences*, vol. 26, no. 8, p. 3692, 2025. doi: 10.3390/ijms26083692.

[25] D. G. Myszka, M. D. Jonsen, and B. J. Graves, "*Equilibrium Analysis of High Affinity Interactions Using BIACORE*," *Analytical Biochemistry*, vol. 265, no. 2, pp. 326–330, 1998.

[26] Z. Lu, K. Xu, K. Xiao, Q. Xu, L. Wang, P. Li, J. Zhou, D. Zhao, L. Bai, Y. Cheng, and W. Huang, "*Biomolecule sensors based on organic electrochemical transistors*," *Nature Electronics*, 2025. doi: 10.1038/s41528-025-00383-x.

[27] R. Gautam, "*State of the Art MOSFET Based Biosensors - A Review*," *Abstract Book of the National Conference on Advances in Basic Science & Technology*, 2025. Available at: sciencepublishinggroup.com/ISBN/979-8-88599-132-2/030.

[28] N. J. Ronkainen, H. B. Halsall, and W. R. Heineman, "*Electrochemical biosensors*," *Chemical Society Reviews*, vol. 39, no. 5, pp. 1747–1763, 2010. doi: 10.1039/B714449K.

[29] Željko Janićijević, T.-A. Nguyen-Le, and L. Baraban, "*Extended-gate field-effect transistor chemo- and biosensors: State of the art and perspectives*," *Next Nanotechnology*, vol. 3–4, p. 100025, 2023. Review article, Open access.

[30] The Royal Swedish Academy of Sciences, "*Press release: The Nobel Prize in Chemistry 2022*," October 2022. Available at: nobelprize.org/prizes/chemistry/2022/press-release.

[31] A. C. Lazanas and M. I. Prodromidis, "*Electrochemical Impedance Spectroscopy*

- *A Tutorial*," *ACS Measurement Science Au*, vol. 3, pp. 162–193, 2023. doi: 10.1021/acsmeasuresciau.2c00070.

[32] A. Lazanas and B. Prieto Simón, "*A Guide to Recognizing Your Electrochemical Impedance Spectra: Revisions of the Randles Circuit in (Bio)sensing*," *Sensors*, vol. 25, no. 19, p. 6260, 2025. doi: 10.3390/s25196260.

[33] A. Peroff, "*Electrochemical Impedance Spectroscopy (EIS) Basics*." Pine Research Support Center, 2024. Published: May 13, 2024. Edited: October 15, 2024. Accessed on 26 May 2026. `https://pineresearch.com/support-article/eis-basics/`.

[34] F. A. Nuñez Perez, "*Analytical–Computational Integration of Equivalent Circuit Modeling, Hybrid Optimization, and Statistical Validation for Electrochemical Impedance Spectroscopy*," *Electrochem*, vol. 6, no. 4, p. 35, 2025. doi: 10.3390/electrochem6040035.

[35] Gamry Instruments, "*Non-ideal Capacitor*." Gamry Instruments Help: EIS Theory, 2026. Accessed on 26 May 2026. `https://help.gamry.com/Framework/experiments_g_main_eis-theory_pcandcircuits_constantphaseelement.html`.

[36] B. Hirschorn, M. E. Orazem, B. Tribollet, V. Vivier, I. Frateur, and M. Musiani, "*Determination of effective capacitance and film thickness from constant-phase-element parameters*," *Electrochimica Acta*, vol. 55, no. 21, pp. 6218–6227, 2010. doi: https://doi.org/10.1016/j.electacta.2009.10.065.

[37] G. Moreno-Grijalva, J. C. Calva-Yáñez, A. Tirado-Guízar, V. Sarmiento, and M. T. Oropeza-Guzmán, "*Evaluation of antigen-antibody recognition by electrochemical impedance on AuNP-biopolymer electrode*," *Journal of Applied Electrochemistry*, vol. 55, pp. 1545–1555, 2025. doi: 10.1007/s10800-024-02257-y.

[38] A. Ahmad and E. Moore, "*Electrochemical immunosensor modified with self-assembled monolayer of 11-mercaptoundecanoic acid on gold electrodes for detection of benzo[a]pyrene in water*," *Analyst*, vol. 137, pp. 5839–5844, 2012. DOI: 10.1039/c2an35236b.

[39] N. I. Bojorge-Ramírez, M. M. Fortes, E. G. Vasconcelos, A. M. Salgados, and B. Valdman, "*Development of an amperometric immunosensor for the biotechnological use of a plant protein*," in *XXII Interamerican Congress of Chemical Engineering (CIIQ 2006) and V Argentinian Congress of Chemical Engineering (CAIQ 2006)*, (Rio de Janeiro, Brazil), Escola de Química, Centro de Tecnologia, Universidade Federal do Rio de Janeiro, 2006.

[40] M. Hosseinzadeh Fakhr, N. Beshchasna, S. Balakin, I. Lopez Carrasco, A. Heitbrink, F. Göhler, N. Rösch, and J. Opitz, "*Cleaning of LTCC, PEN, and PCB Au electrodes towards reliable electrochemical measurements*," *Scientific Reports*, vol. 12, p. 20431, 2022. DOI: 10.1038/s41598-022-23395-3.

[41] N. D. Zakaria, I. L. Salih, H. H. Hamzah, T. Sönmez, M. H. Omar, N. Mo-

hamad Nor, K. Abdul Razak, and V. Balakrishnan, "*Electrochemical and imaging evaluations of electrochemically activated screen-printed gold electrodes*," *Analyst*, vol. 149, no. 22, pp. 5401–5410, 2024. DOI: 10.1039/D4AN00990H.

[42] S. Muhammad, U. B. Zahra, A. Ahmad, L. A. Shah, and A. Muhammad, "*Understanding the Basics of Electron Transfer and Cyclic Voltammetry of Potassium Ferricyanide - An Outer Sphere Heterogeneous Electrode Reaction*," *Journal of the Chemical Society of Pakistan*, vol. 42, no. 6, pp. 813–817, 2020. doi: 10.52568/000705/jcsp/42.06.2020.

[43] N. Elgrishi, K. J. Rountree, B. D. McCarthy, E. S. Rountree, T. T. Eisenhart, and J. L. Dempsey, "*A Practical Beginner's Guide to Cyclic Voltammetry*," *Journal of Chemical Education*, vol. 95, pp. 197–206, 2018. doi: 10.1021/acs.jchemed.7b00361.

[44] I. Otu, "*Transistors: The Fundamental Components of Modern Electronics*," 2023. `https://www.linkedin.com/pulse/transistors-fundamental-components-modern-electronics-isaac-otu` Accessed: 2025-10-08.

[45] S. M. Sze, *Physics of Semiconductor Devices*, ch. Chapter 6, pp. 293–298. Wiley-Blackwell, 2006.

[46] T. Electronics, "*Principles of Electronics: Chapter 19 – Field Effect Transistors*." `https://www.talkingelectronics.com/Download%20eBooks/Principles%20of%20electronics/CH-19.pdf`. Accessed: 2025-10-08.

[47] S. Soclof, "*Transistors: Junction field-effect transistors*," Elsevier, 2006. ISBN: 978-142000315-4, 978-084937339-8.

[48] B. Reeve, "*Simple circuit turns scope, function generator into JFET curve tracer*," *Electronic Design*, vol. 58, no. 11, 2010.

[49] Tektronix, "*How do you find the transconductance of a MOSFET?*." Tektronix. Accessed on 29 May 2026. `https://www.tek.com/en/support/faqs/how-do-you-find-the-transconductance-of-a-mosfet`.

[50] R. Bagale, S. Sahu, F. Basini, M. S. Filipiak, D. Montaigne, C. Ritzenthaler, H. Happy, C. Kleber, R. Boukherroub, W. Knoll, R. Corradini, and S. Szunerits, "*Making field effect transistor measurements accessible to electrochemists and biologists*," *Journal of Solid State Electrochemistry*, vol. 29, pp. 2385–2394, 2025. doi: 10.1007/s10008-025-06225-0.

[51] "*Chronoamperometry*." ScienceDirect Topics, `https://www.sciencedirect.com/topics/engineering/chronoamperometry`, 2020. accessed 2026-05-25.

[52] C.-M. Yang, H.-L. Liu, C.-C. Ho, H.-F. Tsai, and N. Bhalla, "*Single-Step Primary Amine Synthesis on Proton Sensitive Nanofilms to Overcome Its Debye Length Limitations*," *Advanced Materials Interfaces*, vol. 10, p. 2300080, 2023. doi: 10.1002/admi.202300080.

[53] S. Chen, L. Xu, S. Xie, Y. Zhao, L. Xiao, S. Cheng, S. Feng, G.-J. Zhang, Y.-T. Li, and W.-H. Huang, "*Small-Molecule Probes Enhance in Vivo Field-Effect Transistor-Based Biosensing by Overcoming Debye Length Limitations*," *Angewandte Chemie International Edition*, 2025. doi: 10.1002/anie.202516351.

[54] S. Prakash and J. Yeom, *Nanofluidics and Microfluidics*, ch. Chapter 2. Elsevier, 2014. doi: 10.1016/C2010-0-66159-1.

[55] N. V. Bhagavan, "*Water, Acids, Bases, and Buffers*," in *Medical Biochemistry*, pp. 1–16, Academic Press, 4 ed., 2002. doi: 10.1016/B978-012095440-7/50003-2.

[56] Z. Cebula, S. Zołedowska, K. Dziąabowska, M. Skwarecka, N. Malinowska, W. Białobrzeska, E. Czaczyk, K. Siuzdak, M. Sawczak, R. Bogdanowicz, and D. Nidzworski, "*Detection of the Plant Pathogen Pseudomonas syringae pv. lachrymans on Antibody-Modified Gold Electrodes by Electrochemical Impedance Spectroscopy*," *Sensors*, vol. 19, no. 24, p. 5411, 2019. doi: 10.3390/s19245411.

[57] O. Gutiérrez-Sanz, N. M. Andoy, M. S. Filipiak, A. Tarasov, and N. Haustein, "*Direct, Label-Free, and Rapid Transistor-Based Immunodetection in Whole Serum*," *ACS Sensors*, vol. 2, pp. 1278–1286, 2017. doi: 10.1021/acssensors.7b00187.

[58] J. C. Love, L. A. Estroff, J. K. Kriebel, R. G. Nuzzo, and G. M. Whitesides, "*Self-Assembled Monolayers of Thiolates on Metals as a Form of Nanotechnology*," *Chemical Reviews*, vol. 105, no. 4, pp. 1103–1169, 2005. doi: 10.1021/cr0300789.

[59] N. Prize, "*Nobel Prize lecture: Carolyn Bertozzi, Nobel Prize in Chemistry 2022*," December 2022. Available at: youtube.com/watch?v=WyGoeQEHBEk.

[60] Y. Liao, B. Wu, R. Tang, F. Lin, and Y. Tan, "*Strain-Promoted Azide-Alkyne Cycloaddition* [-]," *Progress in Chemistry*, 2022. DOI: 10.7536/PC220103.

[61] E. J. Kim, D. W. Kang, H. F. Leucke, M. R. Bond, and S. Ghosh, "*Optimizing the selectivity of DIFO-based reagents for intracellular bioorthogonal applications*," *Carbohydrate Research*, 2013. DOI: 10.1016/j.carres.2013.05.014.

[62] Z. Huang, X. Yang, Y. Huang, Z. Tang, Y. Chen, H. Liu, M. Huang, L. Qing, L. Li, Q. Wang, Z. Jie, X. Jin, and B. Jia, "*Saliva - A new opportunity for fluid biopsy*," *Clinical Chemistry and Laboratory Medicine*, 2023. DOI: 10.1515/cclm-2022-0793.

[63] Z. Zhang, P. Li, Y. Zhang, H. Gao, and S. Zhang, "*Research Progress on Bovine Serum Albumin (BSA)-based Antifouling Coatings*," *Surface Technology*, 2025. DOI: 10.16490/j.cnki.issn.1001-3660.2025.20.001.

[64] J. A. Lori and T. Hanawa, "*Adsorption characteristics of albumin on gold and titanium metals in Hanks' solution using EQCM*," *Spectroscopy*, 2004. DOI: 10.1155/2004/834639.

[65] T. Janc, V. Vlachy, and M. Lukšič, "*Calorimetric studies of interactions between low molecular weight salts and bovine serum albumin in water at pH values below and above the isoionic point*," *Journal of Molecular Liquids*, 2018. DOI: 10.1016/j.molliq.2017.10.105.

[66] S. P. Daniels, E. J. Whiteside, S. Martin, M. J. S. Moore-Colyer, and P. Harris, "*Straight from the horse's mouth: The effect of different feedstuffs on oral pH in horses and ponies*," *Journal of Equine Veterinary Science*, vol. 142, p. 105181, 2024. doi: 10.1016/j.jevs.2024.105181.

[67] T. Lundström, P. Lingström, O. Wattle, A. Carlén, and D. Birkhed, "*Equine saliva components during mastication, and in vivo pH changes in the oral biofilm of sound and carious tooth surfaces after sucrose exposure*," *Acta Veterinaria Scandinavica*, 2020. doi: 10.1186/s13028-020-00518-2.

[68] Merck, "*1X Phosphate-Buffered Saline (PBS) Recipe Calculator*," n.d. `https://www.sigmaaldrich.com/SE/en/support/calculators-and-apps/1x-phosphate-buffered-saline` Accessed: 2025-10-08.

[69] PalmSens BV, *EmStat Pico Data Sheet*. PalmSens BV, The Netherlands, 2023. Available online: `https://www.palmsens.com/app/uploads/2023/04/PSDAT-ESP-EmStat-Pico-Datasheet.pdf` (Accessed: 2026-05-13).

[70] PalmSens BV, *PSAN-EmStat Pico Field Effect Transistor Characterization*. PalmSens, 2022. Application Note. Available online: `https://assets.palmsens.com/app/uploads/2022/11/PSAN-ESPICO-Characterization-of-Field-Effect-Transistors.pdf` (Accessed: 2026-05-13).

A

METHODscript

This appendix contains the PSTrace METHODscripts used in this work: CA as described in Section A.1, transfer characteristics described in A.2, electrochemical cleaning with CV in Section A.3, CV measurement in Section A.4 and EIS measurement in Section A.5.

A.1 CA transistor

```
e
var i
var e
var i_bipot
set_pgstat_chan 0
set_pgstat_mode 2
set_max_bandwidth 58505m
set_bipot_mode 1
set_range bb 917969p
set_autoranging bb 917969p 917969p
set_bipot_potential 400m
set_range_minmax da -500m -500m
set_range ba 470u
set_autoranging ba 917969p 470u
set_e -400m
cell_on
meas_loop_ca e i -400m 100m 18k add_meas(0 bb i_bipot)
  pck_start
    pck_add e
    pck_add i
    pck_add i_bipot
  pck_end
endloop
on_finished:
  cell_off
```

A.2 Transfer characteristics

```
e
#This sets the device into MethodSCRIPT mode
#------------------------------------------------------------------------
#------------------------------------------------------------------------
#ZEROING SCRIPT
#------------------------------------------------------------------------
#------------------------------------------------------------------------
# set GPIO5 to output mode
set_gpio_cfg 0b100000 1
# turn switch on (high output signal)
set_gpio 0b100000
#------------------------------------------------------------------------
#------------------------------------------------------------------------
#declare variables
# c = WE0 current
var c
# p = set_potential (Vgs for transfer characteristics setup, Vds for
↪  output characteristics setup)
var p
# b = WE1 current
var b
#------------------------------------------------------------------------
#Set up the current measurement on WE1 (i.e. channel 1 in bipot mode)
#select channel 1
set_pgstat_chan 1
#set channel 1 to poly_we (bipot) mode
set_pgstat_mode 5
#Set required bandwidth (Hz)
set_max_bandwidth 100
#set poly_we (bipot) mode = 0, thus WE1 maintains a fixed voltage relative
↪  to RE0
set_poly_we_mode 0
#set starting current range e.g. for 100uA use "set_range ba 100u"
set_range ba 5m
#set WE1 to RE0 offset voltage. (Vds for transfer characteristics setup,
↪  Vgs for output characteristics setup)
set_e 0m
#------------------------------------------------------------------------
#Set up the current measurement on WE0 (i.e. channel 0 in low-speed mode)
#select channel 0
set_pgstat_chan 0
#set channel 0 to low-speed mode
set_pgstat_mode 2
#Set required bandwidth (Hz)
set_max_bandwidth 100
#Set the range for ch 0 (RE0 to WE0) voltage sweep
#(Vgs for transfer characteristics setup, Vds for output characteristics
↪  setup)
```

```
set_range_minmax da -1000m 0m
set_autoranging ba 1n 5m
#set starting current range e.g. for 100uA use "set_range ba 100u"
set_range ba 5m
#set WE0 to offset voltage. (Vgs for transfer characteristics setup, Vds
↪  for output characteristics setup)
set_e 0m
#----------------------------------------------------------------------
#----------------------------------------------------------------------
#Perform the voltage scan, reporting RE0 to WE0 potential, WE0 current,
↪  and WE1 current
#Turn the cell on, any settings set when the cell was off will be applied
↪  here.
cell_on
#equilibrate at -0.5 V for 5 seconds, using a CA measurement
#meas_loop_ca potential(V) current_WE0(A) start(V) interval_time(s)
↪  duration(s) poly_we(1 b)
meas_loop_ca p c -10m 20m 1000m poly_we(1 b)
   #selects ch 1 as the active channel
    set_pgstat_chan 1
    #Set the current range corresponding to the measured current on the
    ↪  secondary WE
    mul_var b 1150m
    set_range ba b
    #selects ch 0 as the active channel
    set_pgstat_chan 0
endloop
#LSV measurement using channel 0 as WE1 and channel 1 as WE2
#WE2 current is stored in var b
#meas_loop_lsv potential(V) current_WE0(A) start(V) end(V) step(V)
↪  scan_rate(V/s) poly_we(1 current_WE1(A))
meas_loop_lsv p c -1000m 0m 1m 100m poly_we(1 b)
    #Send a package containing set potential and measured WE current.
    pck_start
    #The variable 'p' is added to the data packet. The first variable
    ↪  becomes the x-axis in PStrace
    pck_add p
    #The variable 'c' is added to the data packet.
    pck_add c
    #The variable 'b' is added to the data packet.
    pck_add b
    #Signals the end of a measurement data package.
    pck_end
    #selects ch 0 as the active channel
    #set_pgstat_chan 0
    #Measures the WE0 current for 100 ns and stores the value in 'c'
    #meas 100n c ba
    #Set the current range corresponding to the measured current on the
    ↪  main WE
    #//mul_var c 1150m
```

```
    #set_range ba c
    #selects ch 1 as the active channel
    set_pgstat_chan 1
    #Measures the WE1 current for 100 ns and stores the value in 'b'
    #meas 100n b ba
    #Set the current range corresponding to the measured current on the
    ↪  secondary WE
    mul_var b 1150m
    set_range ba b
    #selects ch 0 as the active channel
    set_pgstat_chan 0
endloop
#Turn cell off when finished or aborted
#on_finished:
cell_off
#------------------------------------------------------------------------
#------------------------------------------------------------------------
#MEASURING SCRIPT
#------------------------------------------------------------------------
#------------------------------------------------------------------------
# set GPIO5 to output mode  - might not needed again?
set_gpio_cfg 0b100000 1
# turn switch off (low output signal)
set_gpio 0b000000
#------------------------------------------------------------------------
#------------------------------------------------------------------------
#declare variables
# c = WE0 current
var c
# p = set_potential (Vgs for transfer characteristics setup, Vds for
↪  output characteristics setup)
var p
# b = WE1 current
var b
#------------------------------------------------------------------------
#Set up the current measurement on WE1 (i.e. channel 1 in bipot mode)
#select channel 1
set_pgstat_chan 1
#set channel 1 to poly_we (bipot) mode
set_pgstat_mode 5
#Set required bandwidth (Hz)
set_max_bandwidth 100
#set poly_we (bipot) mode = 0, thus WE1 maintains a fixed voltage relative
↪  to RE0
set_poly_we_mode 0
#set starting current range e.g. for 100uA use "set_range ba 100u"
set_range ba 5m
#set WE1 to RE0 offset voltage. (Vds for transfer characteristics setup,
↪  Vgs for output characteristics setup)
set_e 600m
```

```
#------------------------------------------------------------------
#Set up the current measurement on WE0 (i.e. channel 0 in low-speed mode)
#select channel 0
set_pgstat_chan 0
#set channel 0 to low-speed mode
set_pgstat_mode 2
#Set required bandwidth (Hz)
set_max_bandwidth 100
#Set the range for ch 0 (RE0 to WE0) voltage sweep
#(Vgs for transfer characteristics setup, Vds for output characteristics
↪  setup)
set_range_minmax da -1000m 0m
set_autoranging ba 1n 5m
#set starting current range e.g. for 100uA use "set_range ba 100u"
set_range ba 5m
#------------------------------------------------------------------
#------------------------------------------------------------------
#Perform the voltage scan, reporting RE0 to WE0 potential, WE0 current,
↪  and WE1 current
#Turn the cell on, any settings set when the cell was off will be applied
↪  here.
cell_on
#equilibrate at -0.5 V for 5 seconds, using a CA measurement
#meas_loop_ca potential(V) current_WE0(A) start(V) interval_time(s)
↪  duration(s) poly_we(1 b)
meas_loop_ca p c -10m 20m 1000m poly_we(1 b)
   #selects ch 1 as the active channel
    set_pgstat_chan 1
    #Set the current range corresponding to the measured current on the
    ↪  secondary WE
    mul_var b 1150m
    set_range ba b
    #selects ch 0 as the active channel
    set_pgstat_chan 0
endloop
#LSV measurement using channel 0 as WE1 and channel 1 as WE2
#WE2 current is stored in var b
#meas_loop_lsv potential(V) current_WE0(A) start(V) end(V) step(V)
↪  scan_rate(V/s) poly_we(1 current_WE1(A))
meas_loop_lsv p c -1000m 0m 1m 10m poly_we(1 b)
    #Send a package containing set potential and measured WE current.
    pck_start
    #The variable 'p' is added to the data packet. The first variable
    ↪  becomes the x-axis in PStrace
    pck_add p
    #The variable 'c' is added to the data packet.
    pck_add c
    #The variable 'b' is added to the data packet.
    pck_add b
    #Signals the end of a measurement data package.
```

```
    pck_end
    #selects ch 0 as the active channel
    #set_pgstat_chan 0
    #Measures the WE0 current for 100 ns and stores the value in 'c'
    #meas 100n c ba
    #Set the current range corresponding to the measured current on the
    ↪  main WE
    #//mul_var c 1150m
    #set_range ba c
    #selects ch 1 as the active channel
    set_pgstat_chan 1
    #Measures the WE1 current for 100 ns and stores the value in 'b'
    #meas 100n b ba
    #Set the current range corresponding to the measured current on the
    ↪  secondary WE
    mul_var b 1150m
    set_range ba b
    #selects ch 0 as the active channel
    set_pgstat_chan 0
endloop
#Turn cell off when finished or aborted
on_finished:
cell_off
```

A.3 CV cleaning

```
e
var i
var e
set_pgstat_chan 1
set_pgstat_mode 0
set_pgstat_chan 0
set_pgstat_mode 2
set_max_bandwidth 117011m
set_range_minmax da -100m 1500m
set_range ba 470u
set_autoranging ba 917969p 2350u
set_e -100m
cell_on
meas_loop_ca e i -100m 200m 20
  pck_start
    pck_add e
    pck_add i
  pck_end
endloop
meas_loop_cv e i -100m 1500m -100m 5m 100m nscans(30)
  pck_start
```

```
    pck_add e
    pck_add i
  pck_end
endloop
on_finished:
  cell_off
```

A.4 CV measurement

```
e
var i
var e
set_pgstat_chan 1
set_pgstat_mode 0
set_pgstat_chan 0
set_pgstat_mode 2
set_max_bandwidth 117011m
set_range_minmax da -500m 500m
set_range ba 470u
set_autoranging ba 917969p 2350u
set_e -500m
cell_on
meas_loop_ca e i -500m 200m 20
  pck_start
    pck_add e
    pck_add i
  pck_end
endloop
meas_loop_cv e i -500m 500m -500m 5m 100m nscans(3)
  pck_start
    pck_add e
    pck_add i
  pck_end
endloop
on_finished:
  cell_off
```

A.5 EIS measurement

```
e
var f
var z_r
var z_i
```

```
var i
var e
set_pgstat_chan 1
set_pgstat_mode 0
set_pgstat_chan 0
set_pgstat_mode 3
set_max_bandwidth 500k
set_range_minmax da 280m 280m
set_range ba 2350u
set_autoranging ba 470n 2350u
set_range ab 4200m
set_autoranging ab 4200m 4200m
set_e 280m
cell_on
meas_loop_ca e i 280m 200m 45
  pck_start
    pck_add e
    pck_add i
  pck_end
endloop
set_range ba 2350u
set_autoranging ba 470n 2350u
meas_loop_eis f z_r z_i 10m 50k 50m 30 280m
  pck_start
    pck_add f
    pck_add z_r
    pck_add z_i
  pck_end
endloop
on_finished:
  cell_off
```

B

MATLAB

This appendix contains the MATLAB scripts used for data processing of EIS and CV data. It includes EIS fitting in Section B.1, effective capacitance comparison plot in Section B.2 and CV data analysis in Section B.3.

B.1 EIS fitting

```
%% ========================================================================
% EIS CIRCUIT FITTING
% ========================================================================

rng(1); % Ensures fully reproducible fitting behavior

% ========================================================================
% LIST OF INPUT FILES
% ========================================================================
files = {
    '....'
    '....'
    '....'
    '....'
    '....'
};

% ========================================================================
% MANUAL LEGEND LABELS
% ========================================================================
legend_names = {
     '....'
     '....'
     '....'
     '....'
     '....'
};

% ========================================================================
```

```
% CIRCUIT MODEL SELECTION
%
% 0 = Randles circuit without diffusion
% 1 = Randles circuit including finite-length Warburg diffusion
%
% Each element corresponds to one input file.
% ========================================================================
circuit_type = [          ];

% ========================================================================
% DATA PROCESSING SETTINGS
% ========================================================================

% Frequency rows imported from each CSV file
rowRange = 1:30;

% Minimum number of remaining data points after trimming
minPoints = 20;

% Number of high-frequency points that may be removed
hf_remove = 0:10;

% Number of low-frequency points allowed to be removed per file
% Minimum:maximum low-frequency points removable per file
lf_remove_list = {
     :
     :
     :
     :
     :
};

nFiles = length(files);

% ========================================================================
% PREALLOCATION OF RESULT VARIABLES
% ========================================================================
Rs_all = zeros(nFiles,1);
Rct_all = zeros(nFiles,1);
Q_all = zeros(nFiles,1);
alpha_all = zeros(nFiles,1);

sigma_all = nan(nFiles,1);
tau_all = nan(nFiles,1);

RMSE_all = zeros(nFiles,1);
Ceff_all = zeros(nFiles,1);
```

```
removed_log = cell(nFiles,1);

% ========================================================================
% GLOBAL NYQUIST PLOT INITIALIZATION
% ========================================================================
figAll = figure;
hold on;

xlabel('Z'' [\Omega]');
ylabel('-Z'''' [\Omega]');

grid on;
axis equal;

% Nonlinear least-squares optimization settings
options = optimoptions('lsqnonlin','Display','off');

%% ========================================================================
% MAIN FITTING LOOP
% ========================================================================
for i = 1:nFiles

    % ====================================================================
    % IMPORT AND PREPROCESS DATA
    % ====================================================================
    data = readmatrix(files{i});

    % Extract frequency and impedance columns
    freq = data(rowRange,1);
    Zre  = data(rowRange,5);
    Zim  = -data(rowRange,6);

    % Remove invalid entries
    valid = ~isnan(freq) & ~isnan(Zre) & ~isnan(Zim);

    freq = freq(valid);
    Zre  = Zre(valid);
    Zim  = Zim(valid);

    % Sort frequencies in descending order
    [freq, idx] = sort(freq,'descend');

    Zre = Zre(idx);
    Zim = Zim(idx);

    % Construct complex impedance vector
```

```
Z = Zre + 1i*Zim;

n = length(Z);

% ========================================================================
% EQUIVALENT CIRCUIT MODEL DEFINITION
% ========================================================================

% Model without diffusion
if circuit_type(i) == 0

    model = @(p,f) ...
        p(1) + ...
        1 ./ (1./p(2) + (1i*2*pi*f).^p(4).*p(3));

    n_params = 4;

% Model including finite-length Warburg diffusion
else

    model = @(p,f) ...
        p(1) + ...
        1 ./ ( ...
        1./( ...
        p(2) + ...
        p(5).*tanh(sqrt(1i*2*pi*f*p(6))) ./ ...
        sqrt(1i*2*pi*f*p(6))) + ...
        (1i*2*pi*f).^p(4).*p(3) );

    n_params = 6;
end

% Residual function used by lsqnonlin
costfun = @(p,f,Zd) ...
    [real(model(p,f)) - real(Zd); ...
     imag(model(p,f)) - imag(Zd)];

% ========================================================================
% INITIAL PARAMETER ESTIMATION
% ========================================================================
Rs0 = min(real(Z));

Rct0 = max(real(Z)) - min(real(Z));

Q0 = 1e-5;
alpha0 = 0.85;
```

```
if n_params == 4

    p0_base = [Rs0, Rct0, Q0, alpha0];

    lb = [0, 0, 1e-8, 0.5];
    ub = [Inf, Inf, 1e-2, 1];

else

    sigma0 = Rct0;
    tau0 = 1;

    p0_base = [Rs0, Rct0, Q0, alpha0, sigma0, tau0];

    lb = [0, 0, 1e-8, 0.5, 0, 1e-6];
    ub = [Inf, Inf, 1e-2, 1, Inf, Inf];
end

% ========================================================================
% BASE FIT USING DETERMINISTIC MULTISTART OPTIMIZATION
% ========================================================================
best_rmse = Inf;
best_p = p0_base;

perturb = linspace(-0.5,0.5,10);

for k = 1:10

    p0 = p0_base .* (1 + 0.2*perturb(k));

    try

        p_tmp = lsqnonlin( ...
            @(p) costfun(p,freq,Z), ...
            p0, lb, ub, options);

        Zp = model(p_tmp,freq);

        rmse_tmp = sqrt(mean(abs(Z - Zp).^2));

        if rmse_tmp < best_rmse

            best_rmse = rmse_tmp;
            best_p = p_tmp;
        end

    catch ME
```

```
        warning(ME.message)
        end
    end

    p_base = best_p;
    rmse_base = best_rmse;

    % ========================================================================
    % OPTIONAL EDGE-POINT REMOVAL SEARCH
    % ========================================================================
    best_rmse2 = rmse_base;
    best_p2 = p_base;

    best_removed = [];

    lf_remove = lf_remove_list{i};

    for h = hf_remove
        for l = lf_remove

            idx_keep = true(n,1);

            % Remove high-frequency points
            idx_keep(1:h) = false;

            % Remove low-frequency points
            if l > 0
                idx_keep(end-l+1:end) = false;
            end

            % Ensure sufficient data remain
            if sum(idx_keep) < minPoints
                continue;
            end

            f_tmp = freq(idx_keep);
            Z_tmp = Z(idx_keep);

            rmse_tmp_best = Inf;
            p_tmp_best = p0_base;

            % Deterministic multistart optimization
            for k = 1:10

                p0 = p0_base .* (1 + 0.2*perturb(k));

                try
```

```
                p_tmp = lsqnonlin( ...
                    @(p) costfun(p,f_tmp,Z_tmp), ...
                    p0, lb, ub, options);

                Zp_tmp = model(p_tmp,f_tmp);

                rmse_tmp = sqrt(mean(abs(Z_tmp - Zp_tmp).^2));

                if rmse_tmp < rmse_tmp_best

                    rmse_tmp_best = rmse_tmp;
                    p_tmp_best = p_tmp;
                end

            catch ME
            warning(ME.message)
            end
        end

        % Keep best point-removal solution
        if rmse_tmp_best < best_rmse2

            best_rmse2 = rmse_tmp_best;
            best_p2 = p_tmp_best;

            best_removed = find(~idx_keep);
        end
    end
end

% ========================================================================
% ACCEPTANCE CRITERION
%
% Point removal is accepted only if RMSE improves by at least 10%.
% ========================================================================
improvement = (rmse_base - best_rmse2)/rmse_base;

if improvement < 0.10

    p_fit = p_base;
    rmse = rmse_base;
    removed = [];

else

    p_fit = best_p2;
```

```
        rmse = best_rmse2;
        removed = best_removed;
    end

    % ========================================================================
    % STORE FITTED PARAMETERS
    % ========================================================================
    Rs_all(i) = p_fit(1);
    Rct_all(i) = p_fit(2);

    Q_all(i) = p_fit(3);
    alpha_all(i) = p_fit(4);

    if length(p_fit) == 6

        sigma_all(i) = p_fit(5);
        tau_all(i) = p_fit(6);
    end

    RMSE_all(i) = rmse;

    % ========================================================================
    % EFFECTIVE CAPACITANCE CALCULATION
    %
    % Equation used corresponds to the Randles equivalent circuit.
    % ========================================================================
    Rpar = ...
        (Rs_all(i).*Rct_all(i)) ./ ...
        (Rs_all(i) + Rct_all(i));

    Ceff_all(i) = ...
        Q_all(i).^(1 ./ alpha_all(i)) .* ...
        Rpar.^((1 - alpha_all(i)) ./ alpha_all(i));

    % ========================================================================
    % INDIVIDUAL NYQUIST PLOTS
    % ========================================================================
    Zfit = model(p_fit,freq);

    figure;
    hold on;

    % Plot retained and removed points separately
    if isempty(removed)

        plot(real(Z), -imag(Z), 'bo');
```

```
    else

        keep_idx = true(n,1);
        keep_idx(removed) = false;

        plot(real(Z(keep_idx)), -imag(Z(keep_idx)), 'go');
        plot(real(Z(removed)), -imag(Z(removed)), 'ro');
    end

    % Plot fitted model
    plot(real(Zfit), -imag(Zfit), 'k-','LineWidth',1.5);

    legend(legend_names{i}, 'Interpreter','tex', 'Location','best');

    xlabel('Z'' [\Omega]');
    ylabel('-Z'''' [\Omega]');

    grid on;
    axis equal;

    % Add spectrum to combined Nyquist plot
    figure(figAll);

    plot(real(Z), -imag(Z), ...
        'DisplayName', legend_names{i}, 'LineWidth', 1.5);

    % Store removed point indices
    removed_log{i} = removed;
end

%% ========================================================================
% FINAL SUMMARY TABLE
% ========================================================================
figure(figAll);

legend(legend_names,'Interpreter','tex', 'Location','best');

Relative_RMSE = RMSE_all ./ Rct_all;

T = table( ...
    (1:nFiles)', ...
    Rs_all, ...
    Rct_all, ...
    Q_all, ...
    alpha_all, ...
    sigma_all, ...
    tau_all, ...
```

```
    RMSE_all, ...
    Relative_RMSE, ...
    Ceff_all, ...
    'VariableNames', ...
    {'File','Rs','Rct','Q','alpha','sigma','tau', ...
     'RMSE','Relative_RMSE','Ceff'});

% Relative Rct stepwise change between consecutive measurements
Rct_step = [NaN; diff(Rct_all)./Rct_all(1:end-1)*100];

T.Rct_step_change_percent = Rct_step;

disp(T);

disp('Removed indices per file:');
disp(removed_log);
```

B.2 EIS Ceff comparison plot

```
%% ========================================================================
% EIS CIRCUIT Ceff COMPARISON BETWEEN STEPS
% ========================================================================

rng(1); % Ensures fully reproducible fitting behavior

% ========================================================================
% LIST OF INPUT FILES
% Step before and after desired step for each electrode
% Files are ordered as consecutive before/after pairs
% ========================================================================
files = {
    '....'
    '....'
    '....'
    '....'
    '....'
    '....'
    '....'
    '....'
    '....'
    '....'
};

% ========================================================================
% MANUAL LEGEND LABELS
% Labels used in the paired Ceff comparison plot
```

```
% Defines which electrode each pair corresponds to
% ========================================================================

pair_names = {
    '....'
    '....'
    '....'
    '....'
    '....'
};

% ========================================================================
% CIRCUIT MODEL SELECTION
%
% 0 = Randles circuit without diffusion
% 1 = Randles circuit including finite-length Warburg diffusion
%
% Each element corresponds to one input file.
% Circuit models matched those used in the primary fitting analysis
% ========================================================================
circuit_type = [                    ];

% ========================================================================
% DATA PROCESSING SETTINGS
% ========================================================================

% Frequency rows imported from each CSV file
rowRange = 1:30;

% Minimum number of remaining data points after trimming
minPoints = 20;

% Number of high-frequency points that may be removed
hf_remove = 0:10;

% Number of low-frequency points allowed to be removed per file
% Point-removal limits matched those used in the primary fitting analysis
lf_remove_list = {
    :
    :
    :
    :
    :
    :
    :
    :
    :
```

```
    :
};

nFiles = length(files);

% ========================================================================
% PREALLOCATION OF RESULT VARIABLES
% ========================================================================
Rs_all = zeros(nFiles,1);
Rct_all = zeros(nFiles,1);
Q_all = zeros(nFiles,1);
alpha_all = zeros(nFiles,1);

sigma_all = nan(nFiles,1);
tau_all = nan(nFiles,1);

RMSE_all = zeros(nFiles,1);
Ceff_all = zeros(nFiles,1);

removed_log = cell(nFiles,1);

% ========================================================================

% Nonlinear least-squares optimization settings
options = optimoptions('lsqnonlin','Display','off');

%% ========================================================================
% MAIN FITTING LOOP
% ========================================================================
for i = 1:nFiles

    % ====================================================================
    % IMPORT AND PREPROCESS DATA
    % ====================================================================
    data = readmatrix(files{i});

    % Extract frequency and impedance columns
    freq = data(rowRange,1);
    Zre  = data(rowRange,5);
    Zim  = -data(rowRange,6);

    % Remove invalid entries
    valid = ~isnan(freq) & ~isnan(Zre) & ~isnan(Zim);

    freq = freq(valid);
    Zre  = Zre(valid);
    Zim  = Zim(valid);
```

```
% Sort frequencies in descending order
[freq, idx] = sort(freq,'descend');

Zre = Zre(idx);
Zim = Zim(idx);

% Construct complex impedance vector
Z = Zre + 1i*Zim;

n = length(Z);

% =========================================================================
% EQUIVALENT CIRCUIT MODEL DEFINITION
% =========================================================================

% Model without diffusion
if circuit_type(i) == 0

    model = @(p,f) ...
        p(1) + ...
        1 ./ (1./p(2) + (1i*2*pi*f).^p(4).*p(3));

    n_params = 4;

% Model including finite-length Warburg diffusion
else

    model = @(p,f) ...
        p(1) + ...
        1 ./ ( ...
        1./( ...
        p(2) + ...
        p(5).*tanh(sqrt(1i*2*pi*f*p(6))) ./ ...
        sqrt(1i*2*pi*f*p(6))) + ...
        (1i*2*pi*f).^p(4).*p(3) );

    n_params = 6;
end

% Residual function used by lsqnonlin
costfun = @(p,f,Zd) ...
    [real(model(p,f)) - real(Zd); ...
     imag(model(p,f)) - imag(Zd)];

% =========================================================================
% INITIAL PARAMETER ESTIMATION
```

```
% ========================================================================
Rs0 = min(real(Z));

Rct0 = max(real(Z)) - min(real(Z));

Q0 = 1e-5;
alpha0 = 0.85;

if n_params == 4

    p0_base = [Rs0, Rct0, Q0, alpha0];

    lb = [0, 0, 1e-8, 0.5];
    ub = [Inf, Inf, 1e-2, 1];

else

    sigma0 = Rct0;
    tau0 = 1;

    p0_base = [Rs0, Rct0, Q0, alpha0, sigma0, tau0];

    lb = [0, 0, 1e-8, 0.5, 0, 1e-6];
    ub = [Inf, Inf, 1e-2, 1, Inf, Inf];
end

% ========================================================================
% BASE FIT USING DETERMINISTIC MULTISTART OPTIMIZATION
% ========================================================================
best_rmse = Inf;
best_p = p0_base;

perturb = linspace(-0.5,0.5,10);

for k = 1:10

    p0 = p0_base .* (1 + 0.2*perturb(k));

    try

        p_tmp = lsqnonlin( ...
            @(p) costfun(p,freq,Z), ...
            p0, lb, ub, options);

        Zp = model(p_tmp,freq);

        rmse_tmp = sqrt(mean(abs(Z - Zp).^2));
```

```
        if rmse_tmp < best_rmse

            best_rmse = rmse_tmp;
            best_p = p_tmp;
        end

    catch ME
    warning(ME.message)
    end
end

p_base = best_p;
rmse_base = best_rmse;

% ========================================================================
% OPTIONAL EDGE-POINT REMOVAL SEARCH
% ========================================================================
best_rmse2 = rmse_base;
best_p2 = p_base;

best_removed = [];

lf_remove = lf_remove_list{i};

for h = hf_remove
    for l = lf_remove

        idx_keep = true(n,1);

        % Remove high-frequency points
        idx_keep(1:h) = false;

        % Remove low-frequency points
        if l > 0
            idx_keep(end-l+1:end) = false;
        end

        % Ensure sufficient data remain
        if sum(idx_keep) < minPoints
            continue;
        end

        f_tmp = freq(idx_keep);
        Z_tmp = Z(idx_keep);

        rmse_tmp_best = Inf;
```

```
            p_tmp_best = p0_base;

            % Deterministic multistart optimization
            for k = 1:10

                p0 = p0_base .* (1 + 0.2*perturb(k));

                try

                    p_tmp = lsqnonlin( ...
                        @(p) costfun(p,f_tmp,Z_tmp), ...
                        p0, lb, ub, options);

                    Zp_tmp = model(p_tmp,f_tmp);

                    rmse_tmp = sqrt(mean(abs(Z_tmp - Zp_tmp).^2));

                    if rmse_tmp < rmse_tmp_best

                        rmse_tmp_best = rmse_tmp;
                        p_tmp_best = p_tmp;
                    end

                catch ME
                warning(ME.message)
                end
            end

            % Keep best point-removal solution
            if rmse_tmp_best < best_rmse2

                best_rmse2 = rmse_tmp_best;
                best_p2 = p_tmp_best;

                best_removed = find(~idx_keep);
            end
        end
    end

    % ========================================================================
    % ACCEPTANCE CRITERION
    %
    % Point removal is accepted only if RMSE improves by at least 10%.
    % ========================================================================
    improvement = (rmse_base - best_rmse2)/rmse_base;

    if improvement < 0.10
```

```
        p_fit = p_base;
        rmse = rmse_base;
        removed = [];

    else

        p_fit = best_p2;
        rmse = best_rmse2;
        removed = best_removed;
    end

    % ========================================================================
    % STORE FITTED PARAMETERS
    % ========================================================================
    Rs_all(i) = p_fit(1);
    Rct_all(i) = p_fit(2);

    Q_all(i) = p_fit(3);
    alpha_all(i) = p_fit(4);

    if length(p_fit) == 6

        sigma_all(i) = p_fit(5);
        tau_all(i) = p_fit(6);
    end

    RMSE_all(i) = rmse;

    % Store removed point indices
    removed_log{i} = removed;

    % ========================================================================
    % EFFECTIVE CAPACITANCE CALCULATION
    %
    % Equation used corresponds to the Randles equivalent circuit.
    % ========================================================================
    Rpar = ...
        (Rs_all(i).*Rct_all(i)) ./ ...
        (Rs_all(i) + Rct_all(i));

    Ceff_all(i) = ...
        Q_all(i).^(1 ./ alpha_all(i)) .* ...
        Rpar.^((1 - alpha_all(i)) ./ alpha_all(i));

end
%% ========================================================================
```

```
% FINAL SUMMARY TABLE
% Make sure to compare to results from fitting file so they are the same
% ========================================================================

T = table( ...
    (1:nFiles)', ...
    Rs_all, ...
    Rct_all, ...
    Q_all, ...
    alpha_all, ...
    sigma_all, ...
    tau_all, ...
    RMSE_all, ...
    Ceff_all, ...
    'VariableNames', ...
    {'File','Rs','Rct','Q','alpha','sigma','tau','RMSE','Ceff'});

% Stepwise Rct change between consecutive measurements
Rct_step = [NaN; diff(Rct_all)./Rct_all(1:end-1)*100];

T.Rct_step_change_percent = Rct_step;

disp(T);

disp('Removed indices per file:');
disp(removed_log);

%% ========================================================================
% PAIRED Ceff COMPARISON PLOT
%
% Compares effective capacitance before and after modification for each
% electrode pair.
% ========================================================================
nFiles = length(Ceff_all);

% Assumes files are ordered as consecutive before/after pairs
nPairs = floor(nFiles/2);

Ceff_before = Ceff_all(1:2:end);
Ceff_after  = Ceff_all(2:2:end);

figure;
hold on;

colors = lines(nPairs);

for i = 1:nPairs
```

```
    plot([1 2], ...
         [Ceff_before(i) Ceff_after(i)], ...
         '-o', ...
         'Color', colors(i,:), ...
         'LineWidth', 1.5, ...
         'MarkerSize', 8);
end

xticks([1 2]);

xticklabels({'Before','After'});

ylabel('C_{eff} [F]');

grid on;

% Logarithmic scaling improves visualization across orders of magnitude
set(gca,'YScale','log');

legend(pair_names,'Interpreter','tex', 'Location','best');
```

B.3 Cyclic Voltammetry

```
%% ========================================================================
% Cyclic Voltammetry
% ========================================================================
% ========================================================================
% LIST OF FILES
% ========================================================================
files = {
  '....'
  '....'
  '....'
  '....'
  '....'
};

% ========================================================================
% COLUMN MAPPING PER FILE
%
% Use last cycle results
% Format: {potential_column current_column}
% ========================================================================
col_map = {
    [  ]
```

```
    [  ]
    [  ]
    [  ]
    [  ]
};

% ========================================================================
% MANUAL LEGEND NAMES
% ========================================================================
legend_names = {
    '....'
    '....'
    '....'
    '....'
    '....'
};

%% ========================================================================
% LOAD EXPERIMENTAL DATA
% ========================================================================

nFiles = length(files);

data = cell(nFiles,1);

for k = 1:nFiles
    data{k} = readmatrix(files{k});
end

% ========================================================================
% PREALLOCATE PEAK RESULT ARRAYS
% ========================================================================
Epa_all = zeros(nFiles,1);   % Anodic peak potential
Ipa_all = zeros(nFiles,1);   % Anodic peak current

Epc_all = zeros(nFiles,1);   % Cathodic peak potential
Ipc_all = zeros(nFiles,1);   % Cathodic peak current

DeltaE_all = zeros(nFiles,1); % Peak-to-peak separation

%% ========================================================================
% COMBINED CV FIGURE
%
% All cyclic voltammograms plotted together for direct comparison.
% ========================================================================
figure_all = figure;
```

```
hold on;
grid on;

xlabel('E [V]');
ylabel('I [\muA]');

%% ========================================================================
% MAIN ANALYSIS LOOP
% ========================================================================
for k = 1:length(files)

    % ====================================================================
    % IMPORT DATA
    % ====================================================================
    A = data{k};

    % Extract potential and current columns
    cols = col_map{k};

    E = A(:, cols(1));
    I = A(:, cols(2));

    % ====================================================================
    % REMOVE INVALID DATA POINTS
    % ====================================================================
    valid = ~isnan(E) & ~isnan(I);

    E = E(valid);
    I = I(valid);

    % ====================================================================
    % ADD CURVE TO COMBINED FIGURE
    % ====================================================================
    figure(figure_all);

    % Close the CV loop for visualization
    plot([E; E(1)], [I; I(1)], 'DisplayName', legend_names{k}, 'LineWidth', 1.5);

    % ====================================================================
    % PEAK DETECTION
    %
    % Anodic peak (Epa, Ipa) is defined as the global maximum current.
    % Cathodic peak (Epc, Ipc) is defined as the global minimum current.
    % ====================================================================
    [Ipa, idx_pa] = max(I);
    [Ipc, idx_pc] = min(I);
```

```
    % Corresponding peak potentials
    Epa = E(idx_pa);
    Epc = E(idx_pc);

    % Peak separation
    peaksep = Epa - Epc;

    % ========================================================================
    % STORE PEAK VALUES
    % ========================================================================
    Epa_all(k) = Epa;
    Ipa_all(k) = Ipa;

    Epc_all(k) = Epc;
    Ipc_all(k) = Ipc;

    DeltaE_all(k) = peaksep;

    % ========================================================================
    % INDIVIDUAL CV FIGURE
    %
    % Each voltammogram is plotted individually together with highlighted
    % anodic and cathodic peak positions.
    % ========================================================================
    figure;

    hold on;
    grid on;

    % Plot CV curve
    plot([E; E(1)], [I; I(1)], 'b', 'LineWidth', 1.2);

    % Mark anodic peak
    plot(Epa, Ipa, 'ro', ...
        'MarkerSize', 8, ...
        'LineWidth', 1.5);

    % Mark cathodic peak
    plot(Epc, Ipc, 'go', ...
        'MarkerSize', 8, ...
        'LineWidth', 1.5);

    xlabel('E [V]');
    ylabel('I [\muA]');

legend(legend_names{k}, ...
        'Anodic peak', ...
```

```
        'Cathodic peak', ...
        'Location','best', ...
        'Interpreter','tex');

    % ========================================================================
    % PRINT PEAK VALUES TO COMMAND WINDOW
    % ========================================================================
    fprintf('\n=== %s ===\n', files{k});

    fprintf('Anodic peak:\n');
    fprintf('  Epa = %.4f V\n', Epa);
    fprintf('  Ipa = %.4e µA\n', Ipa);

    fprintf('Cathodic peak:\n');
    fprintf('  Epc = %.4f V\n', Epc);
    fprintf('  Ipc = %.4e µA\n', Ipc);

    fprintf('Peak separation:\n');
    fprintf('  E = %.4f V\n', peaksep);
end

%% ========================================================================
% FINAL COMBINED FIGURE LEGEND
% ========================================================================
figure(figure_all);

legend(legend_names, ...
        'Location','best', ...
        'Interpreter','tex');

%% ========================================================================
% FINAL PEAK TABLE
%
% Summary table containing anodic and cathodic peak parameters for all
% cyclic voltammograms.
% ========================================================================
T = table( ...
    (1:nFiles)', ...
    Epa_all, ...
    Ipa_all, ...
    Epc_all, ...
    Ipc_all, ...
    DeltaE_all, ...
    'VariableNames', ...
    {'File','Epa_V','Ipa_uA','Epc_V','Ipc_uA','DeltaE_V'});

% ========================================================
```

```
% RELATIVE CHANGE, STEPWISE BETWEEN MEASUREMENTS
% ============================================================

Epa_step = [NaN; diff(Epa_all) ./ Epa_all(1:end-1) * 100];
Ipa_step = [NaN; diff(Ipa_all) ./ Ipa_all(1:end-1) * 100];

Epc_step = [NaN; diff(Epc_all) ./ Epc_all(1:end-1) * 100];
Ipc_step = [NaN; diff(Ipc_all) ./ Ipc_all(1:end-1) * 100];

DeltaE_step = [NaN; diff(DeltaE_all) ./ DeltaE_all(1:end-1) * 100];

T.Epa_step_change_percent = Epa_step;
T.Ipa_step_change_percent = Ipa_step;

T.Epc_step_change_percent = Epc_step;
T.Ipc_step_change_percent = Ipc_step;

T.DeltaE_step_change_percent = DeltaE_step;

disp(T);
%% ========================================================================
% COMBINED CV FIGURE WITHOUT BASELINE
%
% Same visualization as the full combined plot, but omitting the first
% dataset for comparison purposes.
% ========================================================================
figure;

hold on;
grid on;

xlabel('E [V]');
ylabel('I [\muA]');

for k = 2:nFiles

    A = data{k};

   cols = col_map{k};

   E = A(:, cols(1));
   I = A(:, cols(2));

    valid = ~isnan(E) & ~isnan(I);

    E = E(valid);
    I = I(valid);
```

```
    plot([E; E(1)], [I; I(1)], ...
        'DisplayName', legend_names{k}, ...
        'LineWidth', 1.5);
end

legend('Location','best','Interpreter','tex');
```

C

Repeatability analysis transfer characteristics EG-FET system

A set of repeatability measurements was performed to evaluate the stability of the transfer characterization as measuring method for the EG-FET system. All measurements were performed in PBS using a gate voltage sweep from -0.39V to +0.39V and a drain source bias of $V_{DS} = 0.4$V. The analysis was based on the linear region of the transfer curve (0 to +0.15 V), where the response was stable and I_{DS} remained below 3 µA.

Five measurement sets were collected, each consisting of five repeated measurements, structured to isolate different sources of variability:

File 1: same electrode, same cuvette, same solution (5 repetitions)

File 2: same electrode, same cuvette, fresh solution (5 repetitions)

File 3: same electrode, new cuvette, fresh solution (5 repetitions)

File 4: new electrode, same cuvette, fresh solution (5 repetitions)

File 5: new electrode, new cuvette, fresh solution (5 repetitions)

Table C.1 shows the calculated slope and its corresponding std based on the obtained results seen in Figures C.1-C.5.

Table C.1: Mean slope and standard deviation for each file.

File	**MeanSlope** $[\mu A/V]$	**Std** $[\mu A/V]$
File 1	4.71×10^3	84.1
File 2	4.50×10^3	86.9
File 3	4.39×10^3	25.8
File 4	4.68×10^3	139
File 5	4.72×10^3	57.2

Overall, the repeatability within each file was low in terms of standard deviation relative to the magnitude of the transfer curve slope, indicating the slope to be a stable measurement parameter for repeated sweeps under different conditions. Differences between measurement files are small in terms of mean transfer curve

slope, which remains fairly consistent across all conditions. Some variation is seen in curve shape and baseline level between files, which is likely related to differences in electrode handling, cuvette exchange and solution preparation.

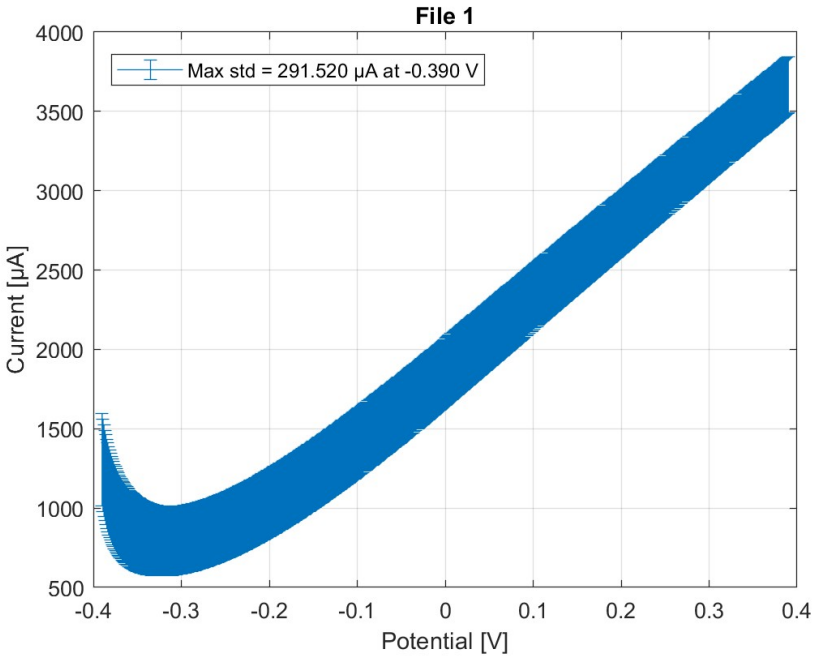

Figure C.1: Mean transfer curve obtained from five repeated measurements (File 1: same electrode, same cuvette, same solution). Error bars indicate standard deviation, showing low variability within repeated sweeps.

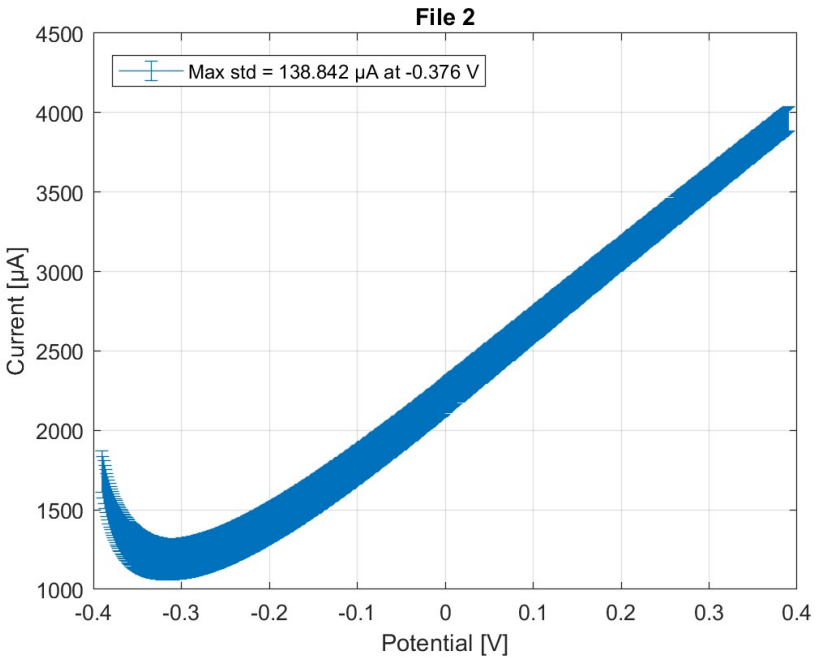

Figure C.2: Mean transfer curve obtained from five repeated measurements (File 2: same electrode, same cuvette, fresh solution). Error bars indicate standard deviation, showing stable repeatability within the measurement set.

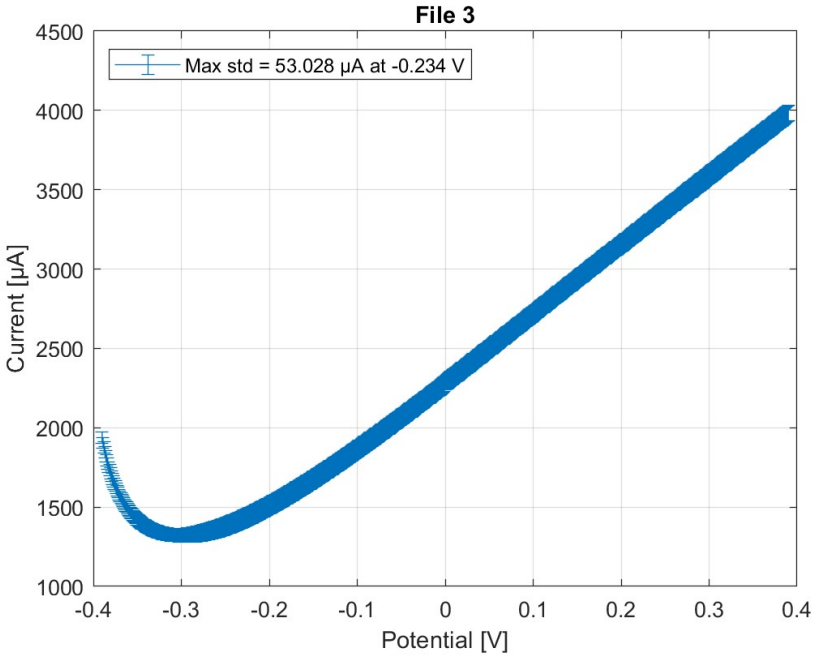

Figure C.3: Mean transfer curve obtained from five repeated measurements (File 3: same electrode, new cuvette, fresh solution). Error bars indicate standard deviation, showing the lowest intra-set variability among all files.

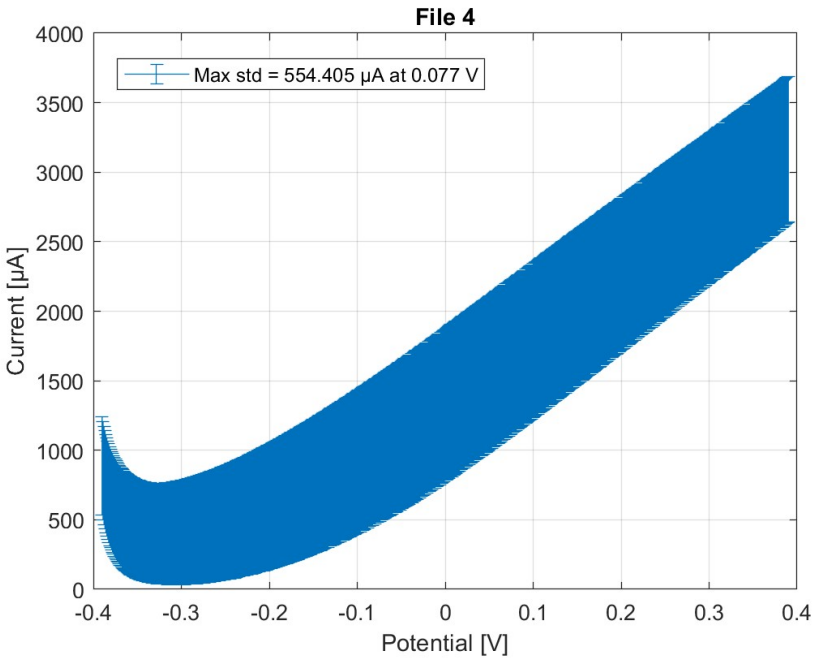

Figure C.4: Mean transfer curve obtained from five repeated measurements (File 4: new electrode, same cuvette, fresh solution). Error bars indicate standard deviation, showing increased variability compared to other measurement sets.

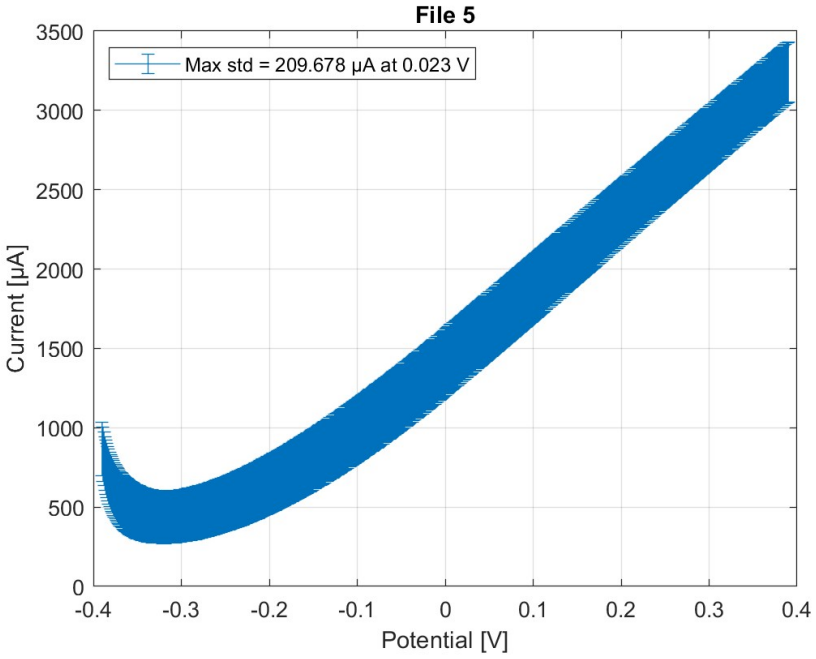

Figure C.5: Mean transfer curve obtained from five repeated measurements (File 5: new electrode, new cuvette, fresh solution). Error bars indicate standard deviation, showing moderate variability within the measurement set.

D

Preliminary tests

This appendix presents the results obtained from the combined electrode configuration used during the preliminary tests to evaluate whether transfer measurements and EIS could be performed on the same electrode. However, no conclusive results were obtained from this setup.

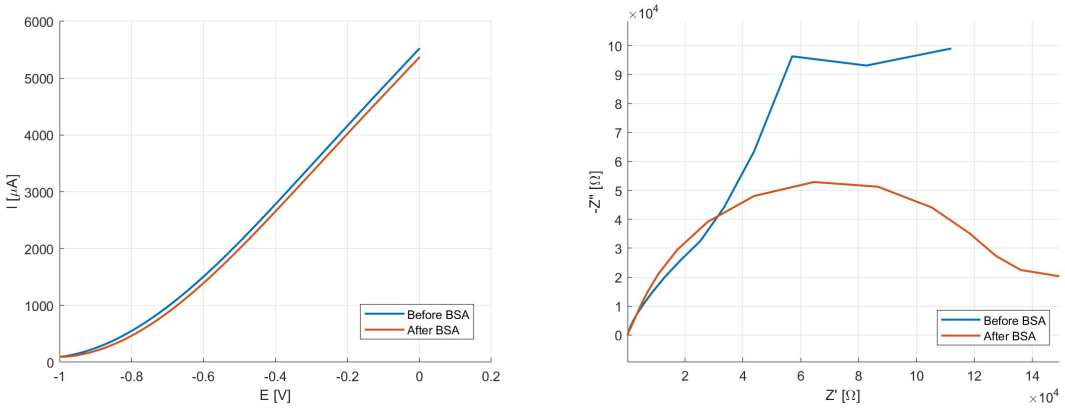

(a) **(b)**

Figure D.1: Combined electrode measurement. (a) Transistor measurements performed first, followed by (b) EIS measurements on the same electrode.

E

Validation of cleaning surface and activation

This appendix presents the results obtained from the two additional electrodes used in the validation of the cleaning protocol, which was performed in triplicate, showing similar trends across all three electrodes.

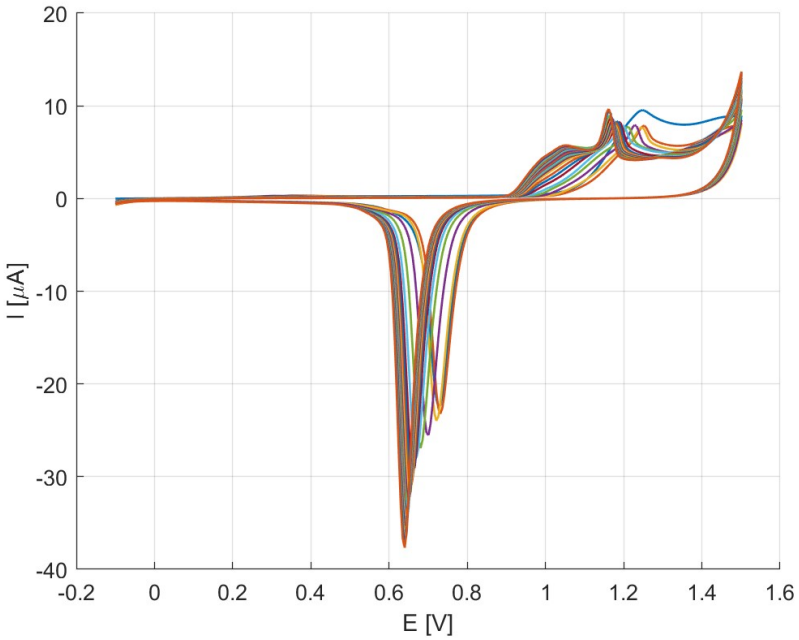

Figure E.1: Cleaning cycle consisting of 30 CV scans in 0.5M sulfuric acid for the second electrode.

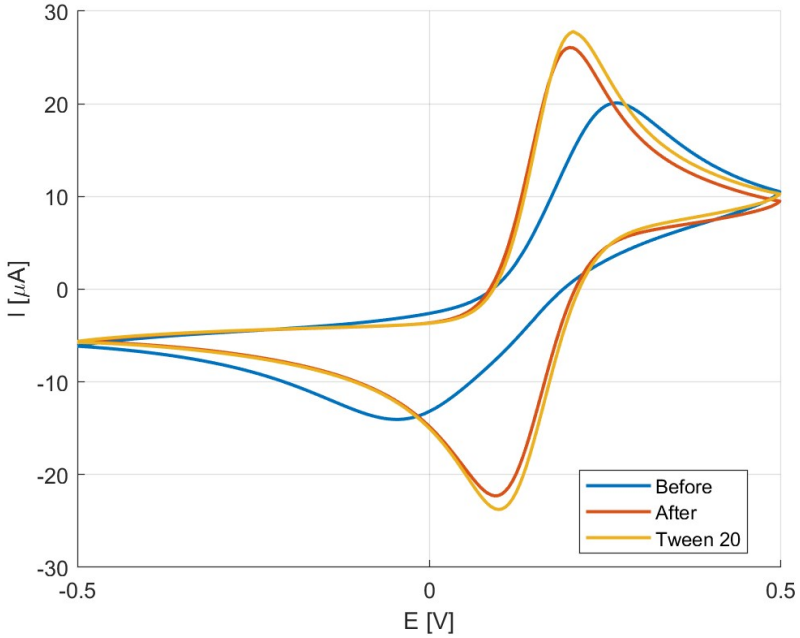

Figure E.2: CV measurements in 5mM K3[Fe(CN)6]/K4[Fe(CN)6] / 0.1M KCl before cleaning, after cleaning and after 1 min incubation in 10mM PBS with 0.05%Tween-20 for the second electrode.

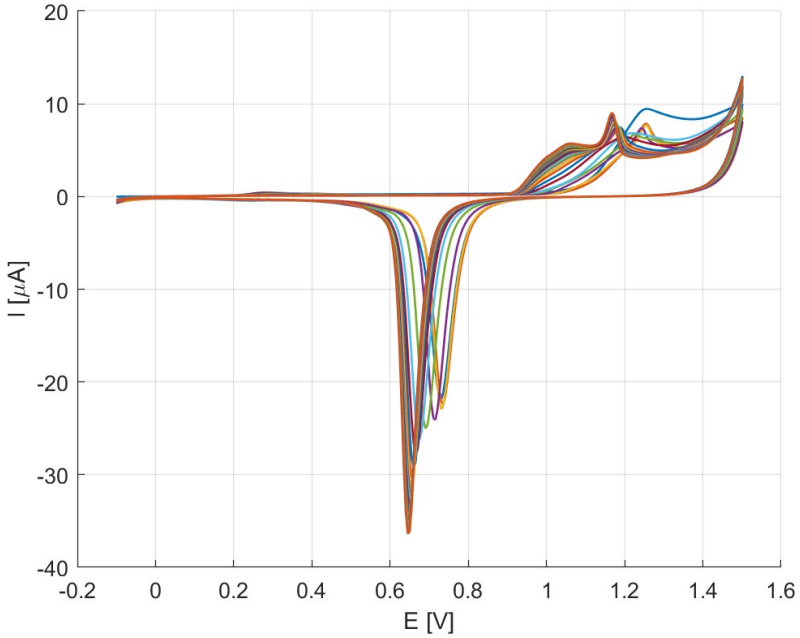

Figure E.3: Cleaning cycle consisting of 30 CV scans in 0.5M sulfuric acid for the third electrode.

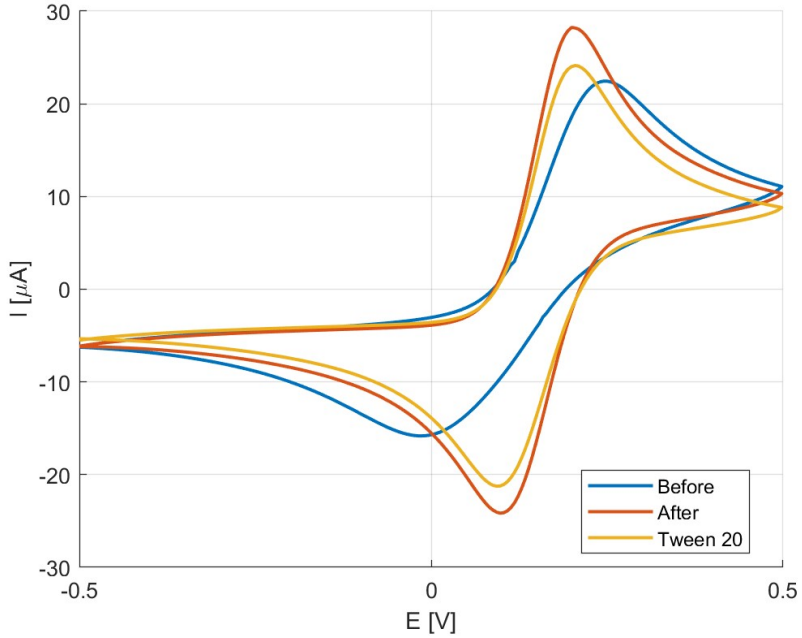

Figure E.4: CV measurements in 5mM K3[Fe(CN)6]/K4[Fe(CN)6] / 0.1M KCl before cleaning, after cleaning and after 1 min incubation in 10mM PBS with 0.05%Tween-20 for the third electrode.

F

Surface functionalization on SPE

This appendix presents the results obtained from the two additional fully functionalized electrodes for both CV and EIS, where the functionalization was performed in triplicate, with similar trends observed across all three electrodes for both methods.

Electrode 2

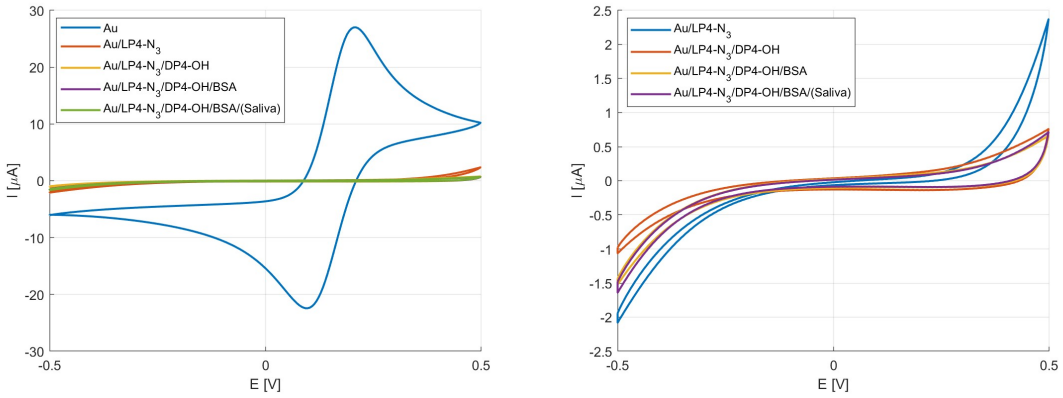

(a) **(b)**

Figure F.1: Cyclic voltammograms of electrode 2 recorded at each step of the functionalization protocol. a) All incubation steps including the initial bare measurement. b) All steps except the bare electrode.

Table F.1: Extracted peak potentials and peak currents for electrode 2 after each measurement. The percentage change in peak currents is calculated relative to the preceding step.

	$\mathbf{E}_{pa}$ [V]	$\mathbf{I}_{pa}$ [μA]	$\mathbf{E}_{pc}$ [V]	$\mathbf{I}_{pc}$ [μA]	$\mathbf{I}_{pa}$ **step** [%]	$\mathbf{I}_{pc}$ **step** [%]
Au	0.210	27.0	0.0930	-22.4	NaN	NaN
LP4-N$_3$	0.498	2.37	-0.500	-2.08	-91.2	-90.7
DP4-OH	0.498	0.760	-0.500	-1.06	-67.9	-48.9
BSA	0.498	0.664	-0.500	-1.52	-12.7	43.3
(Saliva)	0.498	0.715	-0.500	-1.64	7.64	7.80

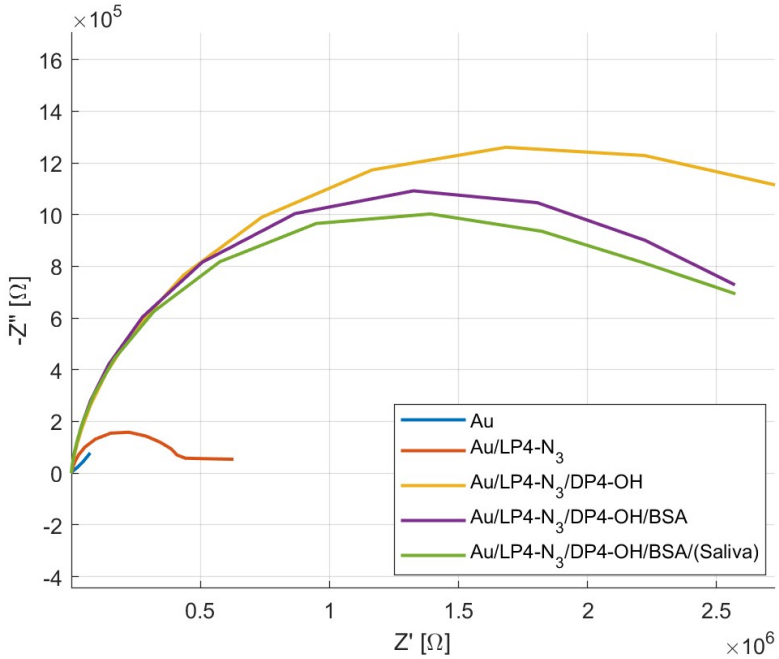

Figure F.2: Nyquist plots of electrode 2 recorded at each step of the functionalization protocol.

Table F.2: Fitted EIS parameters for electrode 2 after each measurement. The percentage change in R_{ct} is calculated relative to the preceding step.

	R_s [Ω]	R_{ct} [Ω]	Q [$\Omega^{-1}s^{\alpha}$]	α	σ [$\Omega\, s^{-1/2}$]	τ [s]	RMSE [Ω]	Rel. RMSE [%]	C_{eff} [F]	R_{ct} step [%]
Au	146	1.42×10^4	3.84×10^{-6}	0.820	2.96×10^5	22.9	330	2.33	7.40×10^{-7}	NaN
LP4-N_3	373	4.25×10^5	3.42×10^{-7}	0.860	14.2	1.31×10^6	5.62×10^3	1.32	7.95×10^{-8}	2.90×10^3
DP4-OH	3.87×10^3	2.63×10^6	3.15×10^{-7}	0.899	7.46×10^5	4.01	2.75×10^4	1.05	1.48×10^{-7}	517
BSA	2.19×10^3	2.36×10^6	2.75×10^{-7}	0.910	4.39×10^5	2.13	2.91×10^4	1.23	1.32×10^{-7}	-10.1
(Saliva)	132	9.19×10^4	2.83×10^{-7}	0.851	2.69×10^6	0.0284	4.48×10^4	48.7	4.73×10^{-8}	-96.1

Electrode 3

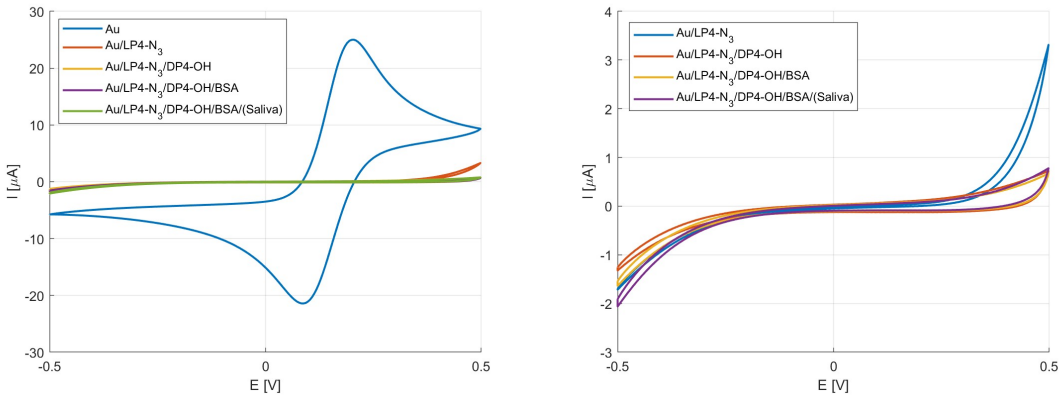

(a) **(b)**

Figure F.3: Cyclic voltammograms of electrode 3 recorded at each step of the functionalization protocol. a) All incubation steps including the initial bare measurement. b) All steps except the bare electrode.

Table F.3: Extracted peak potentials and peak currents for electrode 3 after each measurement. The percentage change in peak currents is calculated relative to the preceding step.

	$\mathbf{E}_{pa}$ [V]	$\mathbf{I}_{pa}$ [μA]	$\mathbf{E}_{pc}$ [V]	$\mathbf{I}_{pc}$ [μA]	$\mathbf{I}_{pa}$ step [%]	$\mathbf{I}_{pc}$ step [%]
Au	0.204	25.0	0.0879	-21.4	NaN	NaN
LP4-N_3	0.498	3.32	-0.500	-1.71	-86.7	-92.0
DP4-OH	0.498	0.724	-0.500	-1.32	-78.2	-22.8
BSA	0.498	0.672	-0.500	-1.64	-7.15	23.9
(Saliva)	0.498	0.778	-0.500	-2.06	15.9	25.8

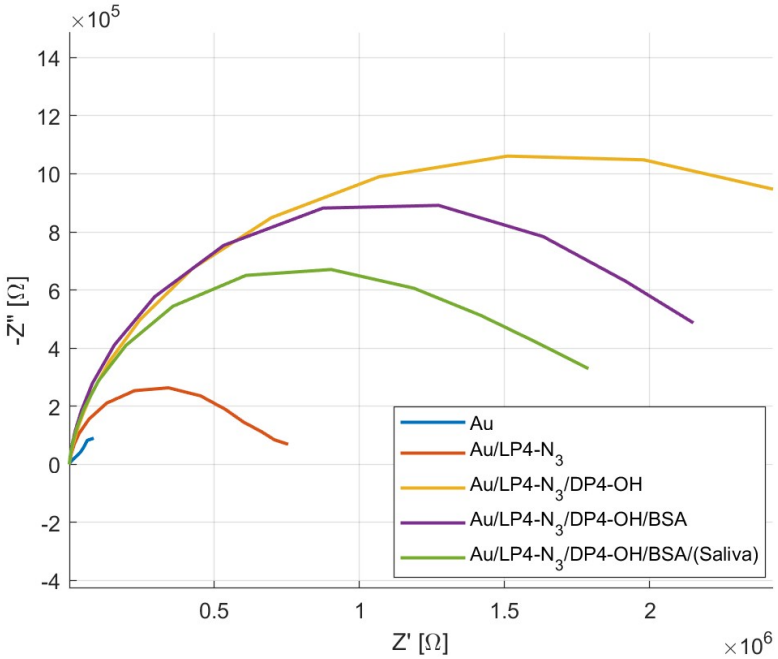

Figure F.4: Nyquist plots of electrode 3 recorded at each step of the functionalization protocol.

Table F.4: Fitted EIS parameters for electrode 3 after each measurement. The percentage change in R_{ct} is calculated relative to the preceding step.

	R_s [Ω]	R_{ct} [Ω]	Q [$\Omega^{-1}s^{\alpha}$]	α	σ [$\Omega\, s^{-1/2}$]	τ [s]	RMSE [Ω]	Rel. RMSE [%]	C_{eff} [F]	R_{ct} step [%]
Au	1.41×10^{-5}	2.95×10^{5}	1.34×10^{-5}	0.589	6.75×10^{5}	5.48	2.14×10^{3}	0.727	2.16×10^{-12}	NaN
LP4-N_3	333	6.41×10^{5}	3.11×10^{-7}	0.905	114	7.51×10^{5}	5.64×10^{3}	0.880	1.18×10^{-7}	117
DP4-OH	2.81×10^{3}	1.94×10^{6}	3.25×10^{-7}	0.900	9.27×10^{5}	2.67	3.16×10^{4}	1.63	1.49×10^{-7}	202
BSA	1.69×10^{3}	2.04×10^{6}	2.81×10^{-7}	0.911	2.25×10^{5}	2.17	2.29×10^{4}	1.13	1.33×10^{-7}	5.10
(Saliva)	285	1.59×10^{6}	2.63×10^{-7}	0.900	2.21×10^{5}	2.64	2.92×10^{4}	1.83	9.16×10^{-8}	-21.7

DEPARTMENT OF PHYSICS AND ASTRONOMY
CHALMERS UNIVERSITY OF TECHNOLOGY
Gothenburg, Sweden
www.chalmers.se

CHALMERS
UNIVERSITY OF TECHNOLOGY